



Properties of the InGaAsSb Alloy and InGaAsSb-Based Photodiodes

Katarina Mamić

Department of Physics

Lancaster University

A thesis submitted for the degree of

Doctor of Philosophy

February, 2025

Properties of the InGaAsSb Alloy and InGaAsSb-Based Photodiodes

Katarina Mamić

Department of Physics, Lancaster University

A thesis submitted for the degree of *Doctor of Philosophy*. February, 2025.

Abstract

The quaternary alloy InGaAsSb is a promising material system for applications in the short-wave infrared (SWIR) spectral region due to its flexible bandgap that can be tuned for wavelengths between 1.7 and 3 μm while remaining lattice matched to GaSb. Despite its increasing prominence in various infrared applications, there is a notable lack of reliable information available on some of the important material properties, particularly for alloys with low indium fractions. Therefore, a more comprehensive analysis of various material and device characteristics is needed to inform the design and development of optimal structures employing this material system. This thesis reports on the growth, fabrication, and characterisation of $\text{In}_x\text{Ga}_{1-x}\text{As}_y\text{Sb}_{1-y}$ *p-i-n* photodiodes with $0 \leq x \leq 0.30$ to investigate the potential of this alloy to provide an alternative to current SWIR technologies, across a more comprehensive bandgap range between 1.7 and 3 μm . The sample growth was carried out via molecular beam epitaxy (MBE) on *n*-type GaSb substrates. Good crystallinity was achieved in samples with $x < 0.15$, with signs of thermodynamically-induced phase separation seen in samples with $x > 0.15$. Both the absorption coefficient and external quantum efficiency (EQE) increased with increasing In fractions in the alloy, up to 8500 cm^{-1} at 2.2 μm and 70% at 1.55 μm measured in $\text{In}_{0.26}\text{GaAsSb}$, respectively. Moreover, the EQE was largely independent of applied bias, suggesting a minority carrier diffusion length that is greater than 1 μm . The bandgap energies extracted from the absorption data exhibited the expected decrease from 0.722 eV measured in GaSb to 0.422 eV measured in $\text{In}_{0.30}\text{GaAsSb}$. Electrical characterisation of InGaAsSb *p-i-n* photodiodes revealed

a significant improvement in both dark current density, which was found to be limited by surface leakage, and zero-bias dynamic resistance-area (R_0A) product with the introduction of In and As to the alloy. The best performance was seen in the $\text{In}_{0.043}\text{GaAsSb}$ photodiode which measured a dark current density and R_0A product of 0.36 mA/cm^2 at -100 mV and $194 \text{ }\Omega\text{cm}^2$, respectively. Furthermore, the background carrier concentration extracted from capacitance-voltage (CV) measurements reduced significantly from $2.7 \times 10^{15} \text{ cm}^{-3}$ in GaSb to $6 \times 10^{14} \text{ cm}^{-3}$ in $\text{In}_{0.30}\text{GaAsSb}$ which points to a reduced native defect concentration. Dark current and R_0A product gradually worsened towards even higher In fractions in the alloy as a result of the bandgap narrowing which increased Shockley-Read-Hall (SRH) generation-recombination. The photodetectors' signal-to-noise performance was summarised with the calculation of specific detectivity which was found to be dominated by leakage and similarly peaked in the $\text{In}_{0.043}\text{GaAsSb}$ photodiode at $8.08 \times 10^{10} \text{ Jones}$ and -10 mV , before reducing towards even higher In fractions in the alloy. The performance of these photodiodes is comparable to commercially available extended InGaAs detectors.

Acknowledgements

I would like to thank my supervisor, Dr. Andy Marshall, without whose endless support, kindness, and more importantly, patience, I would not be where I am today.

Declaration of Authorship

I declare that the work presented in this thesis is, to the best of my knowledge and belief, original and my own work except where the contributions by others are specifically stated. Parts of this thesis have been published in the following conferences and academic journals:

K. Mamić, L. A. Hanks, J. E. Fletcher, A. P. Craig, A. R. J. Marshall. "Electrical and optical characterisation of InGaAsSb-based photodetectors for SWIR applications," *Semiconductor Science and Technology*, vol. 39, 2024

K. Mamić, A. Bainbridge, L. A. Hanks, A. P. Craig, A. R. J. Marshall. "InGaAsSb for cut-off tuned SWIR detectors," *Proc. SPIE 12430*, Quantum Sensing and Nano Electronics and Photonics XIX, 124300O, 2023

A. Bainbridge, **K. Mamić**, L. A. Hanks, F. Al-Saymari, A. P. Craig, A. R. J. Marshall. "Resonant Cavity Enhanced Photodiodes in the Short-Wave Infrared for Spectroscopic Detection," *IEEE Photonics Technology Letters*, vol. 32, 2020

L. A. Hanks, **K. Mamić**, K. Klos, A. Bainbridge, J. Fletcher, L. Gilder, L. Tedstone, F. J. Castano, A. R. J. Marshall. "Quasi-planar InGaAsSb p-B-n photodiodes for spectroscopic sensing," *Optics Express*, Vol. 31, No. 9, 2023

K. Mamić, L. A. Hanks, A. Bainbridge, A. P. Craig, A. R. J. Marshall. "InGaAsSb for cut-off tuned SWIR detectors," *UK Semiconductors*, Sheffield, UK (2022) (oral presentation)

K. Mamić, L. A. Hanks, A. Bainbridge, A. P. Craig, A. R. J. Marshall "InGaAsSb for cut-off tuned SWIR detectors," *SPIE Photonics West*, San Francisco, USA (2023) (oral presentation)

Contents

1	Introduction and Overview of e-SWIR Detector Structures	1
2	Background Theory	5
2.1	Absorption coefficient	5
2.1.1	Absorption processes in a semiconductor material	6
2.2	Device physics	8
2.2.1	<i>p-n</i> junction	8
2.2.2	<i>p-i-n</i> junction	12
2.2.2.1	Current-voltage characteristics	14
2.2.2.2	Junction capacitance	23
2.2.3	Quantum efficiency	24
2.2.4	Specific detectivity	25
3	Literature Review	27
3.1	GaSb	27
3.2	InGaAsSb	31
3.2.1	Growth of $\text{In}_x\text{Ga}_{1-x}\text{As}_y\text{Sb}_{1-y}$ alloys	31
3.2.2	Optical parameters	35
3.3	InGaAsSb detectors	39
3.4	Summary	48
4	Experimental Methods	52
4.1	Sample growth	52

4.2	X-ray diffraction	59
4.3	Fabrication	63
4.3.1	Sample cleaning	64
4.3.2	Photolithography	64
4.3.3	Contact deposition	67
4.3.4	Wet chemical etching	71
4.3.5	Passivation	72
4.4	Characterisation	75
4.4.1	Fourier Transform Infrared spectroscopy	76
4.4.2	Current-voltage and quantum efficiency measurements	78
4.4.3	Spectral responsivity measurements	80
4.4.4	Capacitance-voltage measurements	81
4.4.5	Capacitance modelling	81
5	Results I	85
5.1	Photodetector design	85
5.2	Growth of InGaAsSb <i>p-i-n</i> photodiodes	89
5.3	Growth of InGaAsSb transmission layers	91
5.4	XRD analysis	92
5.5	Optical characteristics	98
5.5.1	Absorption coefficient	98
5.5.2	Urbach energy	106
5.5.3	Bandgap energy	108
5.6	Conclusion	110
6	Results II	113
6.1	Electrical characteristics	113
6.1.1	Current-voltage characteristics	113
6.1.2	Unintentional intrinsic doping	125
6.1.3	Quantum efficiency	128

6.1.4	Specific detectivity	130
7	Conclusions and Future Work	133
7.1	Conclusions	133
7.2	Future Work	136
	References	139

List of Tables

5.1	$\text{In}_x\text{Ga}_{1-x}\text{As}_y\text{Sb}_{1-y}$ <i>p-i-n</i> photodiodes grown via MBE, with indium fractions between $0 \leq x \leq 0.3$. The degree of lattice mismatch is indicated for each sample.	87
5.2	$\text{In}_x\text{Ga}_{1-x}\text{As}_y\text{Sb}_{1-y}$ transmission layers grown via MBE, with indium fractions between $0 \leq x \leq 0.25$. The degree of lattice mismatch is indicated for each sample. *Samples grown on single side polished GaAs.	88

List of Figures

2.1	Absorption coefficient of an arbitrary semiconductor with a 0.5 eV bandgap and an Urbach energy of 5 meV. The dashed line represents the ideal case with no sub-bandgap absorption.	8
2.2	Operation of a p - n photodiode under zero bias. a) Diffusion and recombination of carriers creates the depletion region. b) Band bending ensures the Fermi level, E_f , remains constant across the junction. c) Electric field distribution.	9
2.3	Operation of a p - n photodiode under reverse bias. a) The depletion region penetrates deeper into the n and p layers. b) Applied voltage, V_R , increases the potential step which is equal to $e(V_0 + V_R)$. d) Electric field distribution.	11
2.4	a) Operation of a p - i - n photodiode. b) Energy band diagram under reverse bias. c) Electric field distribution.	13
2.5	Leakage mechanisms in a reverse-biased p - i - n junction diode: a) band-to-band EHP generation, b) trap-assisted generation, c) trap-assisted generation within the depletion region, d) trap-assisted tunneling, e) direct band-to-band tunneling.	18
2.6	IV characteristics of a typical p - i - n junction diode, adapted from Sze et al.[63], showing voltage-dependent leakage mechanisms; a) shunt resistance effects, b) recombination current region, c) diffusion current region, d) high injection region, e) series resistance effects, and f) reverse leakage due to generation current and surface effects.	21

3.1	Phase diagram of $\text{In}_x\text{Ga}_{1-x}\text{As}_{1-y}\text{Sb}_y$, taken from reference [104]. The solid lines correspond to compositions lattice matched to GaSb and InAs. The immiscibility region predicted by the author's calculations is indicated on the graph.	33
3.2	Bandgap energy variation with composition, x , for $(\text{GaSb})_{1-x}(\text{InAs}_{0.91}\text{Sb}_{0.09})_x$ according to Vurgaftman[100]. Dashed line indicates the location of the miscibility gap.	36
3.3	Bandgap energy variation with alloy composition for $\text{In}_x\text{Ga}_{1-x}\text{As}_y\text{Sb}_{1-y}$. Solid lines represent interpolation schemes proposed by Moon (black) and Vurgaftman (red). Symbols show experimental data available in literature.	38
3.4	(a) Various theoretical models for the absorption coefficient of $\text{In}_{0.16}\text{GaAsSb}$. (b) Measured absorption coefficient of $\text{In}_x\text{Ga}_{1-x}\text{As}_y\text{Sb}_{1-y}$ with $0.15 \leq x \leq 0.266$ grown by various techniques.	40
3.5	Band diagram of a barrier photodetector employing an InGaAsSb absorber taken from reference [22].	46
3.6	Summary of the specific detectivity and EQE values found in literature for InGaAsSb-based photodetectors. Red squares and blue triangles correspond to D^* and EQE values of homojunction p - (i) - n photodiodes, respectively. Red circles and blue diamonds correspond to D^* and EQE values of barrier $n\text{Bn}/p\text{Bn}$ photodiodes, respectively.	49
4.1	(a) In_xGaAsSb p - i - n photodiode structure grown on n -type GaSb substrates with various In fractions to enable the comparison of InGaAsSb detector properties with varying alloy composition. (b) InGaAsSb transmission sample structure grown on semi-insulating GaAs substrates with the aim of obtaining extended absorption coefficient data. *This layer thickness is 4500 nm for the GaSb transmission sample.	53

4.2	Schematic of an MBE growth chamber showing thermal effusion cells with cell shutters, substrate holder/heater assembly, RHEED system, cryopanel, and pumps.	54
4.3	Image of the RHEED screen showing a $3\times$ surface reconstruction during GaSb buffer growth, taken from reference [70].	58
4.4	Simplified representation of lattice-matched and strained epitaxial layers.	59
4.5	Schematic of the X-ray diffraction apparatus.	61
4.6	An example XRD scan of a thick GaSb layer epitaxially grown on a GaAs substrate. Red line shows the spectrum simulated via the Bede RADS software.	62
4.7	Processing flow for <i>p-i-n</i> photodiodes showing several lithography steps, contact deposition, and wet chemical etching.	65
4.8	Deposition of a resist bi-layer enables a clean lift-off by creating a break in the deposited contact.	68
4.9	Processing steps for the passivation of the photodiodes' sidewalls with SU-8 photoresist.	74
4.10	(a) <i>p-i-n</i> device structure. (b) Surface of a fabricated sample as seen under a microscope showing the circular mesas and the horseshoe top contacts.	75
4.11	A schematic diagram of the Vertex 70 FTIR spectrometer showing the optical path for a typical transmission measurement, with relevant components labelled[165]. OPF is the optical filter wheel, APT is the aperture wheel, BMS is the beamsplitter, and D1 and D2 are detector positions.	77
4.12	A schematic diagram of the IV setup. SMU (sourcemeater unit) is a Keithley 2400.	79
4.13	A schematic diagram of the QE setup with the InGaAs detector as a reference.	80

4.14	Electric field distribution in a $p-i-n$ device structure with N_i doping concentrations, and X_i depletion widths, assuming p and n regions are fully depleted of carriers. E_1 and E_2 are the boundary electric fields.	82
4.15	An example of the CV model fit to experimental data.	83
5.1	InGaAsSb $p-i-n$ photodetector structure showing layer thicknesses and doping profile.	86
5.2	Transmission sample structure of (a) InGaAsSb, and (b) GaSb.	88
5.3	X-ray diffraction data for $\text{In}_x\text{Ga}_{1-x}\text{As}_y\text{Sb}_{1-y}$ $p-i-n$ samples with: (a) $x = 0.043$, (b) $x = 0.05$, (c) $x = 0.1$, and (d) $x = 0.12$	94
5.4	X-ray diffraction data for $\text{In}_x\text{Ga}_{1-x}\text{As}_y\text{Sb}_{1-y}$ $p-i-n$ samples with: (a) $x = 0.15$, (b) $x = 0.20$, (c) $x = 0.26$, and (d) $x = 0.30$	96
5.5	Transmission spectra of the XK1779 sample and the GaSb substrate reference.	99
5.6	Diagram of the transmission and reflection through the $p-i-n$ structure.	99
5.7	(a) Transmission against wavelength of the thick GaSb on GaAs sample. (b) Cosine of the phase angle, ϕ , as a function of photon energy superimposed onto the raw transmission data.	101
5.8	Diagram of the transmission and reflection through the GaSb sample.	101
5.9	(a) Room temperature absorption coefficient of $\text{In}_x\text{Ga}_{1-x}\text{As}_y\text{Sb}_{1-y}$ samples with $0.05 \leq x \leq 0.30$ on a log-linear scale. (b) Room temperature absorption coefficient of GaSb measured in this work compared to literature.	104
5.10	Experimental absorption coefficient data of binaries InSb[176], InAs[177], and GaSb[174], ternary $\text{In}_{0.53}\text{Ga}_{0.47}\text{As}$ [178], and quaternary $\text{In}_{0.22}\text{GaAsSb}$ (MBE)[99], $\text{In}_{0.167}\text{GaAsSb}$ (LPE)[118], $\text{In}_{0.16}\text{GaAsSb}$ (OMVPE)[42], and $\text{In}_{0.15}\text{GaAsSb}$ (OMVPE)[124] taken from literature. $\text{In}_{0.26}\text{GaAsSb}$, $\text{In}_{0.26}\text{GaAsSb}$, and GaSb measured in this work are also shown.	105

5.11	Urbach tail and absorption edge fits for (a) $\text{In}_x\text{Ga}_{1-x}\text{As}_y\text{Sb}_{1-y}$ samples with $0.05 \leq x \leq 0.30$, and (b) GaSb.	106
5.12	The variation of (a) Urbach energy, and (b) the exponent, n , with In fraction in the alloy.	107
5.13	An example of the two graphical methods for extracting the bandgap energy from absorption coefficient data for the $\text{In}_{0.1}\text{GaAsSb}$ sample.	108
5.14	Variation of the bandgap energy with In fraction in the alloy. The two solid lines correspond to interpolation methods from Vurgaftman et al.[100] with a bowing parameter of 0.75 eV, and Moon et al.[114]. The same interpolation method from Vurgaftman applied to our data with a higher bowing parameter of 0.92 eV is represented by the dashed line.	109
6.1	Current density against voltage for In_xGaAsSb samples with (a) $x = 0$, (b) $x = 0.043$, (c) $x = 0.1$, (d) $x = 0.15$, (e) $x = 0.20$, (f) $x = 0.26$, and (g) $x = 0.30$. (h) Current density against voltage of all unpassivated samples taken from 800 μm device mesas.	115
6.2	(a) An example of the IV fit in forward bias for the $\text{In}_{0.15}\text{GaAsSb}$ sample. Y-intercept corresponds to the reverse saturation current. The ideality factor is extracted from the slope of the exponential region. (b) The variation of ideality factor with indium fraction in the alloy.	116
6.3	Shunt resistance variation with In fraction.	118
6.4	The variation of measured and fitted current density with In fraction in the alloy. The dashed and dotted lines indicate the theoretical bandgap dependence of current density, relative to the 4.3% indium sample assuming $n = 2$ and 1.36, respectively.	120
6.5	Measured current density at -100 mV against P/A ratio for (a) unpassivated, and (b) SU-8 passivated samples.	121

6.6	(a) Variation in the dynamic resistance area product with In fraction.	
	(b) $1/R_dA$ product against P/A ratio for In_xGaAsSb samples with $0 \leq x \leq 0.30$.	123
6.7	Reverse current density against voltage measured in $\text{In}_x\text{Ga}_{1-x}\text{As}_y\text{Sb}_{1-y}$ photodiodes with $x = 0, 0.043, 0.1, \text{ and } 0.2$, compared to an extended InGaAs detector from Hamamatsu[183].	124
6.8	The intrinsic unintentional doping concentration as a function of In fraction in the alloy for $\text{In}_x\text{Ga}_{1-x}\text{As}_y\text{Sb}_{1-y}$ layers with $0 \leq x \leq 0.30$. Note that the sample with $x = 0.15$ could not be satisfactory fit and is not presented on the graph. The inset shows an example of the CV fit for the sample with $x = 0.30$.	126
6.9	(a) Current flowing through a biased $\text{In}_{0.043}\text{GaAsSb}$ photodiode under dark and light conditions. (b) External quantum efficiency against voltage for $\text{In}_x\text{Ga}_{1-x}\text{As}_y\text{Sb}_{1-y}$ photodiodes with $0 \leq x \leq 0.30$. The inset shows an example of the responsivity spectrum at zero bias for the sample with 4.3% In.	128
6.10	(a) Specific detectivity against voltage at $1.55 \mu\text{m}$ for GaSb and InGaAsSb photodiodes. (b) Measured and bulk limited peak specific detectivities and R_0A product as a function of In fraction in the alloy.	130
6.11	Measured and bulk limited wavelength dependant specific detectivities of our $\text{In}_{0.1}\text{GaAsSb}$ <i>p-i-n</i> photodiode compared to a commercially available InGaAs photodetector with a $2.6 \mu\text{m}$ cutoff[185].	132

List of Acronyms

SWIR Short-Wave Infrared

e-SWIR Extended Short-Wave Infrared

MWIR Mid-Wave Infrared

NIR Near Infrared

FPA Focal Plane Array

TPV Thermophotovoltaic Cell

LED Light-Emitting Diode

XRD X-Ray Diffraction

MBE Molecular Beam Epitaxy

LPE Liquid Phase Epitaxy

MOCVD Metalorganic Chemical Vapour Deposition

OMVPE Organometallic Vapour-Phase Epitaxy

DOS Density of States

EHP Electron-Hole Pair

QE Quantum Efficiency

EQE External Quantum Efficiency

SRH Shockley-Read-Hall

MCT Mercury Cadmium Telluride

NEP Noise-Equivalent Power

BEP Beam-Equivalent Pressure

DFT Density-Functional Theory

PAS Positron Annihilation Spectroscopy

XPS X-ray Photoelectron Spectroscopy

PL Photoluminescence

EL Electroluminescence

SEM Scanning Electron Microscopy

FTIR Fourier Transform Infrared Spectroscopy

IMF Interfacial Misfit Array

TAT Trap-Assisted Tunneling

UHV Ultra High Vacuum

RHEED Reflection High Energy Electron Diffraction

TEM Transmission Electron Microscopy

Chapter 1

Introduction and Overview of e-SWIR Detector Structures

The short-wave infrared (SWIR) spectral region, spanning between 1 and 3 μm , contains absorption fingerprints of various important compounds such as CO_2 , CH_4 , H_2O , NH_3 , glucose, and many others[1], [2]. Therefore, sensing in this region is crucial for applications in remote sensing, telecommunications, medical sensing, defense, and many other fields[3], [4]. As a result, development of high-performance and reliable SWIR detectors has become the focus of much research and development. Various material systems have been employed over the years to facilitate detection in this spectral region, including HgCdTe, Ge, InAs, PbS, and InGaAs. However, current commercial SWIR detectors based on these materials are limited by their low responsivity, narrow spectral response range and/or large noise at room temperature which limits their applications and increases cost[3]. Furthermore, the spectral range between 1.7 μm (marked by the cutoff wavelength of InP lattice matched InGaAs) and the beginning of the mid-wave infrared (MWIR) at 3 μm , known as the extended short-wave infrared, or e-SWIR, is considered a performance gap for infrared photodetectors[2], [5]. For this reason, various bulk and superlattice structures have been developed to aid detection in the e-SWIR region[4]. These are InGaAs/GaAsSb type-II superlattices grown on InP

substrates[6], [7], and InAs/GaSb[8], InAs/GaSb/AlSb/GaSb[9], InAs/AlSb[10], InAs/InSb/AlSb/InSb[11], and InAs/InAsSb/AlAsSb[12] superlattices as well as bulk InPSb[13] grown on GaSb substrates. However, extended-InGaAs detectors, grown lattice mismatched to InP substrates to achieve wavelengths up to $\sim 3 \mu\text{m}$ [14], are still the standard solution, despite the many issues encountered during growth and fabrication of such mismatched structures[2], [5]. The performance of extended InGaAs detectors drops off rapidly beyond $1.7 \mu\text{m}$ due to increasing mismatch which causes strain-induced defects such as threading dislocations[2], [15], leading to higher leakage currents. The high defect density also reduces yield making the fabrication of focal plane arrays (FPAs) with this material challenging[4].

The quaternary alloy InGaAsSb, lattice-matched to GaSb, has emerged as the most promising alternative to current technologies for detection in the e-SWIR region, with InGaAsSb-based detectors already widely used for environmental monitoring and gas sensing[16], [17]. The advantage in using this material system comes from its highly flexible bandgap which can be tuned for applications in the entire e-SWIR region and beyond, between the GaSb cutoff at $1.7 \mu\text{m}$ and $4.9 \mu\text{m}$, all whilst remaining lattice-matched to GaSb[18]. At one end of this spectrum, GaSb-based photodetectors have routinely underperformed their InGaAs counterparts due to various growth and fabrication issues. Epitaxial GaSb is known to suffer from a high concentration of native defects introduced during growth which gives rise to its high residual p -type background. Additionally, the GaSb surface is highly reactive and prone to oxidation which creates surface leakage channels[19], [20]. Both of these issues negatively impact the detector performance by increasing unwanted dark currents and limiting responsivity. Although similar fabrication issues were noted in other Sb-based photodetectors, InGaAsSb has shown promise as a lower-leakage, higher-detectivity alternative to GaSb and potentially extended-InGaAs for applications in the e-SWIR. Due to its flexibility, InGaAsSb has already established itself as the active region in many infrared structures including photodetectors[21], [22], thermophotovoltaic (TPV) cells[23], [24], light-emitting diodes[25], [26], and

lasers[27], [28].

Growth of this alloy has been successfully realized via various epitaxy techniques, including LPE[29], [30], MOCVD[31], [32], OMVPE[33], [34], and MBE[18], [35], although not without difficulties. InGaAsSb contains a large miscibility gap which limits the growth of layers with In fractions greater than $\sim 20 - 30\%$ depending on the growth technique and conditions employed[18], [33]. Within this region, the alloy is subject to spinodal decomposition, whereby it decomposes into a mixture of GaAs- and InSb-rich quaternary phases[36], [37]. However, this phase separation can be suppressed when growing InGaAsSb layers under non-equilibrium conditions, i.e lower growth temperatures. For this reason, molecular beam epitaxy was found to be the most suitable method for growing InGaAsSb due to the much lower growth temperatures achievable which successfully exploits surface dynamics and limits phase separation[16], [36]. Growth of InGaAsSb layers with cutoff wavelengths up to $\sim 3 \mu\text{m}$ has been successfully demonstrated via MBE[22]. Additionally, digital alloys have been explored as an alternative to traditional bulk structures as a way of obtaining compositions within the miscibility gap. This digital alloying technique, also known as "modulated beam growth", refers to the growth of a short-period superlattice (thin layers of alternating alloys with very short periodicity)[38]. Such a structure is typically engineered to emulate a quaternary alloy and exhibit some of the same properties such as the bandgap energy or refractive index[38], [39]. However, growing digital alloys comes with its own set of challenges. This alloying technique requires precise control of layer thicknesses and very sharp interfaces in order to maintain the correct periodicity, where issues such as interfacial segregation, localization of carriers, and strain accumulation in the case of mismatched layers need to be addressed[38], [40].

Despite the increased interest in the InGaAsSb material system, most work reports on single alloy compositions with a focus on higher In fractions in the alloy[41]–[46], with no study to date that overviews material properties and detector performance across the more comprehensive bandgap range between 1.7

and 3 μm . Furthermore, there is a lack of reliable information available on some of the important material properties, such as the absorption coefficient and the compositional dependence of bandgap energy, needed to successfully design structures employing this material. It is essential to build a thorough understanding of InGaAsSb material properties and device performance characteristics in order to truly exploit its potential through the design and development of optimal structures. Therefore, the main aim of this work was to study how the various material and device properties of InGaAsSb vary with increasing In fractions in the alloy, from 0% In in pure GaSb, to the onset of the miscibility gap in alloys with $\sim 30\%$ In. To enable such comparison, a homojunction *p-i-n* device structure was chosen, where the growth and fabrication of these photodiodes was carried out under consistent conditions.

Chapter 2 provides the theoretical background necessary to understand the function of infrared photodetectors, while chapter 3 gives a summary of available literature on GaSb and InGaAsSb with a focus on growth and fabrication issues as well as detector performance. Chapter 4 presents the experimental methods employed for the growth, fabrication, as well as characterisation of InGaAsSb photodiodes. MBE-growth of high quality $\text{In}_x\text{Ga}_{1-x}\text{As}_y\text{Sb}_{1-y}$ layers with $0 \leq x \leq 0.30$ was demonstrated in chapter 5, and the issues with phase separation encountered when approaching the miscibility limit are discussed. Moreover, this chapter reports on the material properties of InGaAsSb layers with a focus on the absorption coefficient and the variation in the bandgap energy with In fraction. Various electrical properties of InGaAsSb photodiodes including leakage currents, dynamic resistance, capacitance, and quantum efficiency are presented in chapter 6. Finally, as the ultimate figure of merit that defines signal-to-noise performance of a detector, specific detectivity is presented as a function of alloy composition.

Chapter 2

Background Theory

This chapter introduces the key concepts needed to understand the function and properties of infrared photodetectors presented in this work. These include absorption processes in a bulk semiconductor material, physics of *p-i-n* junctions, leakage characteristics of *p-i-n* photodiodes, the role of junction capacitance in such diodes, and finally the quantum efficiency and specific detectivity as important parameters which define the performance of the detectors.

2.1 Absorption coefficient

The absorption coefficient, α , is defined as the fraction of the light intensity, I , absorbed per unit length (or thickness) of an optical medium, such that

$$\frac{I}{I_0} = e^{-\alpha t} \quad (2.1)$$

where I_0 is the incident light intensity, and t is the thickness of the medium. Likewise, transmission through a medium, T , is defined as the ratio of the transmitted light intensity, I , to incident light intensity, i.e. $T = I/I_0$. In order to calculate the absorption coefficient of a thin film, one has to consider multiple reflections from the front and back surfaces. In the case of incoherent light, where the thickness of the film, t , is much greater than the coherence length of the light, the interference

effects are negligible and the transmission through the film is given by:

$$T = \frac{I}{I_0} = \frac{(1 - R_1)(1 - R_2)e^{-\alpha t}}{1 - R_1 R_2 e^{-2\alpha t}} \quad (2.2)$$

where R_1 and R_2 are reflectivities at the front and back surfaces respectively[47]. If $R_1 = R_2 = R$, the above expression can be simplified to:

$$T = \frac{(1 - R)^2 e^{-\alpha t}}{1 - R^2 e^{-2\alpha t}} \quad (2.3)$$

where the reflectivity, R , is given by[47]:

$$|n - 1|^2 / |n + 1|^2 \quad (2.4)$$

Here, n is the refractive index of the film. In the case of coherent light, where the coherence length is greater than the thickness of the medium, interference fringes will arise and the transmission through a medium is given by:

$$T = \frac{(1 - R_1)(1 - R_2)e^{-\alpha t}}{1 - 2\sqrt{R_1 R_2} \cos(\phi)e^{-\alpha t} + R_1 R_2 e^{-2\alpha t}} \quad (2.5)$$

where ϕ is the phase angle between the reflected and transmitted light given by $(4\pi n t) / \lambda_0$. Here, λ_0 is the wavelength of light in vacuum. Such interference effects are seen in GaSb and InGaAsSb samples grown on semi insulating GaAs substrates due to the relatively large difference in the refractive indices between the two materials and their respective thicknesses. Equation 2.5 will be adjusted to fit the more complex structures presented in this work in section 5.5.1.

2.1.1 Absorption processes in a semiconductor material

The fundamental absorption in semiconductors refers to band-to-band transitions, i.e. excitation of electrons from the valence to the conduction band when photons with energies greater than or equal to the bandgap are incident on the material[48]. The bandgap energy, E_g , of a semiconductor is defined as the energy separation between the parabolic conduction band minimum and the valence band

maximum[49]. In III-V compound semiconductors, the absorption coefficient rapidly increases at the fundamental edge, typically up to $\sim 10^4 \text{ cm}^{-1}$ and continues to increase steadily at higher photon energies[50]. The magnitude of absorption depends on the density of states (DOS) near the conduction and valence band edges which varies between different materials. A lower DOS in one of the bands will lead to a lower absorption coefficient near the fundamental absorption edge, whereas a high DOS in both the valence and conduction bands will lead to a markedly higher absorption.

The absorption coefficient in a semiconductor material can be described by:

$$\alpha(h\nu) = A(h\nu - E_g)^n \quad (2.6)$$

for $h\nu \geq E_g$, where $h\nu$ is photon energy, and A is a constant[47], [48], [51]. In a direct gap material, where the conduction band minimum and the valence band maximum are located at $k = 0$, the absorption increases with a square root dependence on energy, and $n = 1/2$. In a perfect crystalline intrinsic semiconductor, there is no absorption for $h\nu < E_g$. However, the introduction of impurities, as well as alloying which often degrades material homogeneity and leads to defect formation, causes a perturbation of the band structure resulting in the formation of localized states with a lower density near the band edges, extending them into the bandgap[48], [52], [53]. This band tailing due to lattice disorder enables sub-bandgap absorption which is known to have an exponential dependence on energy for $h\nu < E_g$, and can be empirically described by:

$$\alpha = \alpha_0 \exp[(h\nu - E_g)/E_U] \quad (2.7)$$

where E_U is the characteristic Urbach energy which defines the width of the absorption tail, and α_0 is the absorption coefficient at the bandgap energy[47], [54], [55]. Figure 2.1 shows the absorption coefficient of a typical direct-gap semiconductor.

The investigation of the Urbach energy plays an important role in determining the

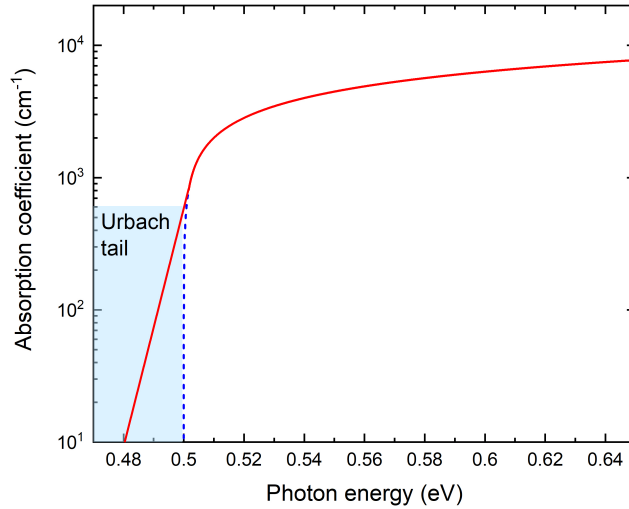


Figure 2.1: Absorption coefficient of an arbitrary semiconductor with a 0.5 eV bandgap and an Urbach energy of 5 meV. The dashed line represents the ideal case with no sub-bandgap absorption.

material quality of a quaternary alloy like InGaAsSb which can suffer from alloying induced defects and phase separation often seen in various epitaxy techniques, particularly in alloys with higher indium fractions which approach the onset of the miscibility gap. A detailed investigation of the absorption edge and Urbach energy of samples presented in this work is conducted in section 5.5.2.

2.2 Device physics

2.2.1 p - n junction

To understand the operation of p - i - n photodiodes presented in this work, we first need to understand the workings of a simple p - n junction - the building block of the vast majority of opto-electronic devices.

A p - n junction is formed when a p -type and an n -type semiconductors are joined together. Holes from the p -side diffuse across the junction and combine

with electrons from the n -side, leaving behind negatively charged acceptor centres. The same happens with electrons which diffuse across the junction into the p -side, recombining with holes and leaving behind positively charged donor centres, as illustrated in figure 2.2a.

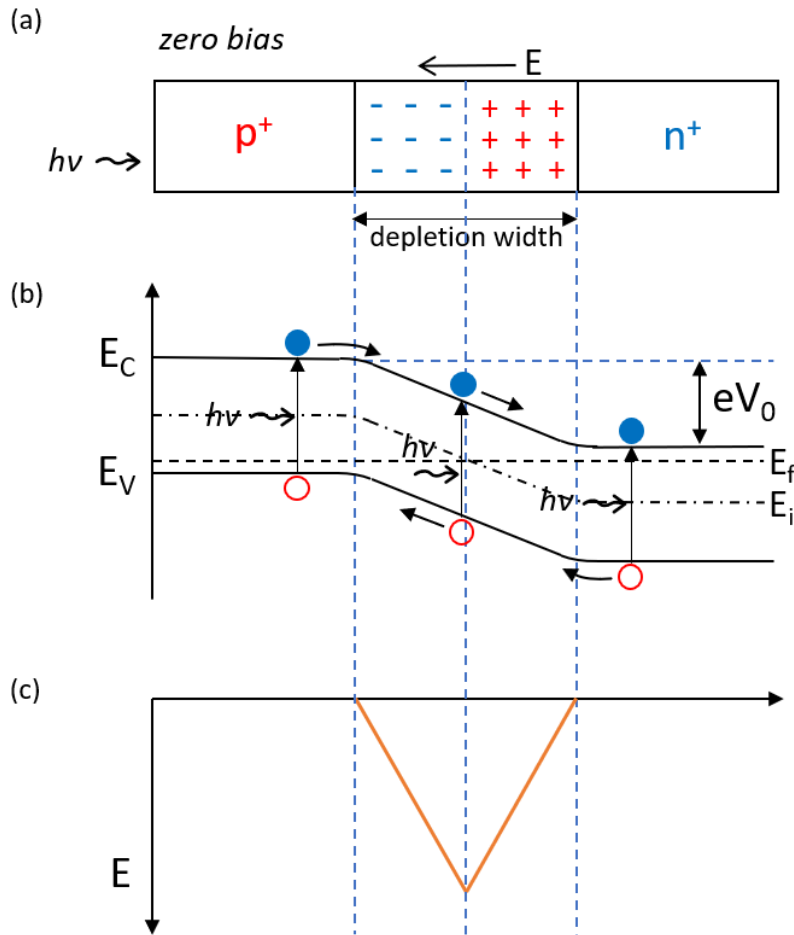


Figure 2.2: Operation of a p - n photodiode under zero bias. a) Diffusion and recombination of carriers creates the depletion region. b) Band bending ensures the Fermi level, E_f , remains constant across the junction. c) Electric field distribution.

As the fixed charges build up around the junction, an electric field is produced which opposes further carrier diffusion across the junction. At the same time, any thermally generated minority carriers near the junction will be accelerated by the

electric field and give rise to a drift current which flows in the opposite direction to the diffusion current. An equilibrium will be reached with no net current flow across the junction, such that:

$$I_{diff} + I_{drift} = 0 \quad (2.8)$$

where I_{diff} and I_{drift} are the diffusion and drift currents respectively.

The region near the junction that is now depleted of free carriers is called the depletion region or the space-charge region, and will be discussed in more detail in the following sections. Band bending ensures the Fermi level, E_f , remains constant across the junction as can be seen in figure 2.2b, and the resulting potential difference between the p and n sides at thermal equilibrium is called the built-in potential, V_0 . Applying forward bias to the p - n junction decreases the depletion layer width and reduces the built-in potential enabling more holes and electrons to overcome the smaller potential barrier and diffuse across the junction, i.e. minority carrier injection occurs and current flows through the junction. This is the operating condition for light emitting diodes[56].

Applying reverse bias has the opposite effect on the diode; the depletion width increases and so does the built-in potential, greatly reducing the diffusion currents[56], as illustrated in figure 2.3a. However, the large electric field enables the flow of thermally generated minority carriers across the junction. This current is known as the reverse saturation current. A band diagram of a p - n junction under reverse bias is illustrated in figure 2.3b. A photodiode is operated under reverse bias to ensure only a very small current flows in the circuit when no light is present[47]. When photons with energy greater than or equal to the bandgap of the semiconductor are incident on a photodiode, they are absorbed in the material creating electron-hole pairs (EHPs). If these are created within the depletion region (or a diffusion length away from it), the electric field separates the EHPs which drift towards the diode terminals, and induce a current flow in the external circuit. This

current is known as the photocurrent.

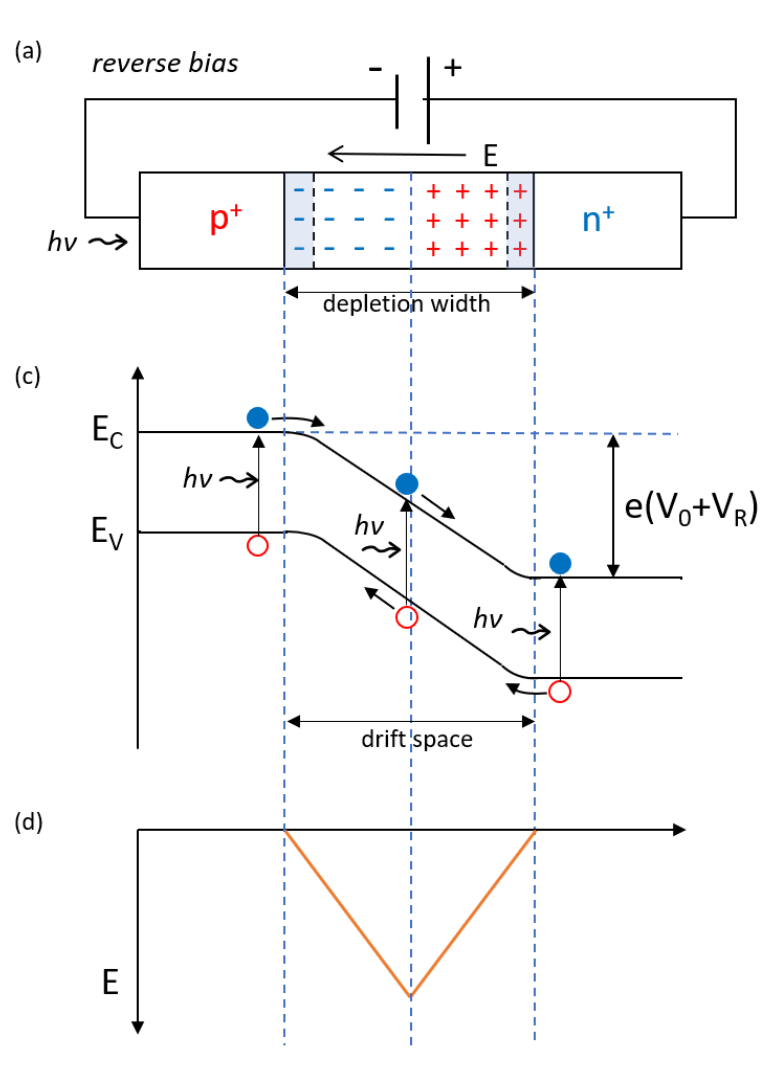


Figure 2.3: Operation of a p - n photodiode under reverse bias. a) The depletion region penetrates deeper into the n and p layers. b) Applied voltage, V_R , increases the potential step which is equal to $e(V_0 + V_R)$. d) Electric field distribution.

A wider depletion region is preferable to ensure efficient collection of the EHPs and maximisation of the quantum efficiency as well as lower junction capacitance, hence a p - n photodiode is typically operated at a large reverse bias. Likewise, the top p layer is kept thin to minimise the chances of photons being absorbed away from the depletion region[57].

The main disadvantage of a $p-n$ diode is the small depletion width which prevents operation at high modulation frequencies due to a higher junction capacitance, and also limits the device's ability to collect photocurrent. Since the penetration depth of light is inversely proportional to the absorption coefficient, in a $p-n$ structure with a junction located near the surface, longer wavelengths will penetrate beyond the small depletion width. Likewise, if the junction is located deeper in the structure, shorter wavelengths will not reach the depletion region, while the longer wavelengths can still penetrate beyond. In both cases some of the incident photons will be absorbed outside of the depletion region where there is no field to separate the EHPs. A $p-i-n$ diode does not suffer from such limitations which makes it one of the most common photodetector structures[56].

2.2.2 $p-i-n$ junction

The $p-i-n$ structure, illustrated in figure 2.4, is widely used in many opto-electronic devices, including photodetectors, light-emitting diodes, solar cells, and optical modulators[47]. What differentiates this structure from the basic $p-n$ junction diode is the existence of a relatively thick intrinsic region between the p and n layers[58]. The intrinsic layer has a high resistivity due to a very low doping level, which allows the depletion region to extend through to the n layer with relatively low bias, providing a large depleted volume with an electric field to separate EHPs. It is important to note, however, that in practice the intrinsic layer is lightly (unintentionally) doped which results in the electric field not being entirely uniform across the depletion layer[56]. The $p-i-n$ diode is usually kept at a sufficiently high voltage which keeps the intrinsic region fully depleted of carriers. The result is a diode with a depletion width that is practically independent of applied bias, unlike the $p-n$ diode[59].

The majority of the incident photons are absorbed in the fully depleted intrinsic layer whose electric field separates the EHPs created either in the depletion region, or within a diffusion length of it. The resulting holes and electrons drift across the

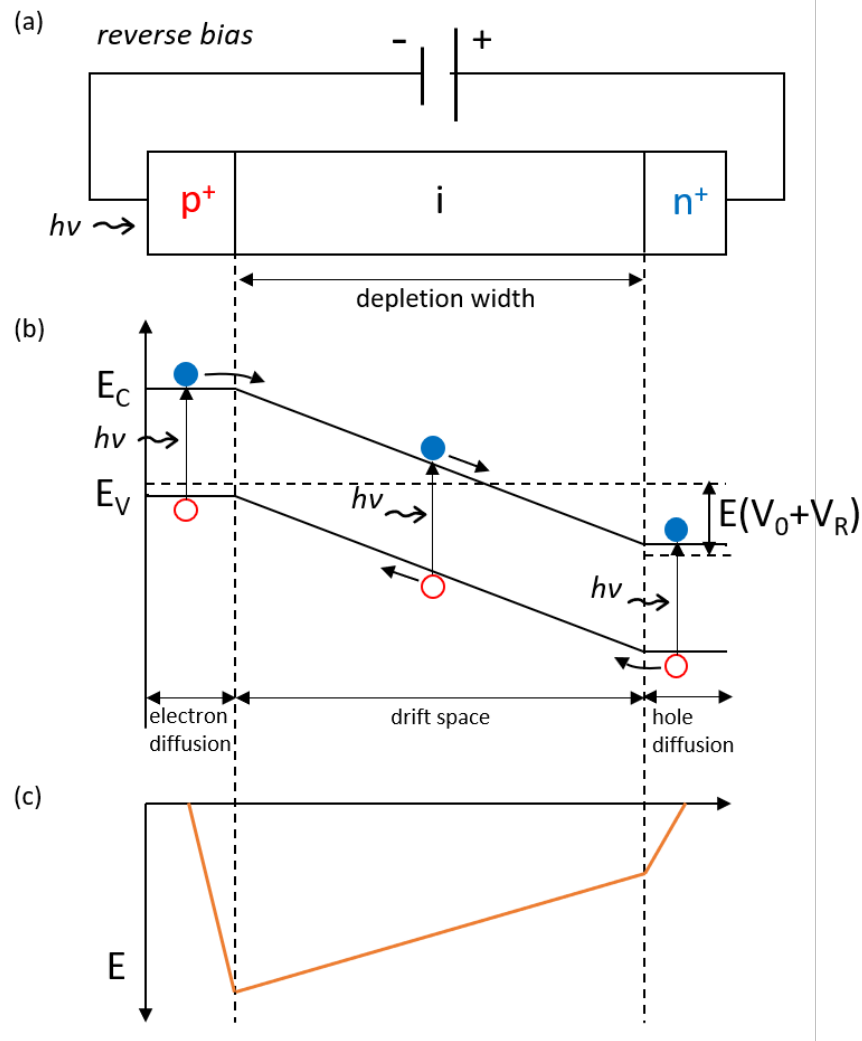


Figure 2.4: a) Operation of a $p-i-n$ photodiode. b) Energy band diagram under reverse bias. c) Electric field distribution.

depletion layer and are collected by the contacts. A thicker intrinsic layer increases the responsivity of the diode as more photons are being absorbed in the wider depletion region, however, it also reduces the response time which is limited by the drift time of the photogenerated carriers across the depletion layer[56]. The penetration depth of photons into the intrinsic region is also wavelength-dependant, all of which influences the structure design depending on the desired outcome[58]. To minimise absorption outside of the depletion region one can employ a heterojunction

p-i-n structure with transparent *n* and *p* cladding layers. In detectors that employ the InGaAsSb absorber, a common cladding (or window) layer is the wide-bandgap AlGaAsSb [60], [61]. However, this was not attempted in this work since the focus was on studying the material properties rather than optimising a specific photodetector structure.

2.2.2.1 Current-voltage characteristics

Current flowing through a biased *p-i-n* junction can generally be described by the ideal diode equation[57]:

$$I = I_0(\exp(qV/kT) - 1) \quad (2.9)$$

where I_0 is the reverse saturation current, V is the applied voltage, k is the Boltzmann constant, and T is the temperature. From equation 2.9 we can see that the current increases exponentially with forward bias, whereas with reverse bias the exponential term approaches zero and the total current in the diode is equal to the reverse saturation current (the rate of thermally generated minority carrier drift across the junction) if applied voltage is greater than a few kT/q . This represents the ideal diffusion-limited case, where the dark current under reverse bias is caused by injection of electrons from the *p* side into the *n* side and vice versa, the injection of holes from the *n* side into the *p* side. Here, dark current refers to any current that flows through a reverse biased *p-i-n* junction without illumination. However, most diodes deviate from the above expression due to additional effects that were not considered. The most notable additional contributions to the overall diode current are: (i) generation and recombination of carriers in the depletion region, (ii) band-to-band or trap-assisted tunnelling, (iii) Auger generation, (iv) Ohmic losses, and (v) surface effects. These originate either from the bulk of the material (bulk currents), or the exposed surface of the devices (surface currents).

Bulk currents

(i) Shockley-Read-Hall generation-recombination

One of the assumptions made in the derivation of equation 2.9 is that recombination and thermal generation of carriers take place in the neutral p and n regions. However, both of these processes can occur within the depletion region. Generation of carriers within the depletion region can take place via two main mechanisms; band-to-band generation of EHPs, and generation by emission from recombination centres, also known as Shockley-Read-Hall (SRH) generation-recombination. If the depletion width is smaller than the diffusion length of electron and holes, band-to-band EHP generation within the depletion region has a negligible additional contribution to the reverse current. However, most semiconductors contain recombination centres, the most significant ones being those located near the middle of the bandgap due to lattice defects and/or impurities. It is the release of carriers from these generation centres, i.e. SRH generation, that can notably increase the reverse current. An electron will be thermally excited from the recombination centre to the conduction band leaving behind an empty state which will subsequently be occupied by a thermally excited valence electron, which in turn leaves behind a hole in the valence band. Since the depletion region has a very small carrier concentration under reverse bias, the generated carriers are swept away by the strong electric field before recombination can take place, hence net generation occurs. Since this generation occurs within the depletion region, and the depletion width increases with reverse bias according to[62]:

$$W = \sqrt{\frac{2\epsilon_0\epsilon_r (N_A + N_D)}{e N_A N_D} (V_0 - V)} \quad (2.10)$$

where ϵ_0 is the vacuum permittivity, ϵ_r is the relative permittivity of the semiconductor, e is the electron charge, N_A and N_D are the concentrations of acceptors and donors respectively, and V is the applied voltage, then the reverse current also increases approximately with the square root of reverse bias[62] (unlike in

the diffusion limited case where the reverse current plateaus). This type of generation is particularly influential in wider bandgap semiconductors since band-to-band generation in neutral regions in such materials is small[62]. SRH generation is typically the main source of unwanted leakage currents in junction detectors. InGaAsSb has a small enough bandgap and a relatively high defect density compared to more mature semiconductor materials such as silicon, which would suggest SRH generation is likely to be a significant factor. Different leakage mechanisms found in InGaAsSb photodiodes, including SRH generation, will be discussed in more detail in section 6.1.1.

In forward bias, where there is no strong electric field to sweep out the generated carriers before they can recombine, current due to recombination of carriers within the depletion region becomes non-negligible. This recombination current increases approximately with $\exp(qV/2kT)$, instead of $\exp(qV/kT)$ which holds true for recombination in neutral p and n regions. Hence the diode equation can be re-written as[62]:

$$I = I_0(\exp(qV/nkT) - 1) \quad (2.11)$$

where n is the ideality factor which determines the deviation from the ideal characteristics, and is approximately equal to 1 in the ideal diffusion limited case, but approaches 2 when the recombination current dominates. Recombination current typically dominates at lower injection levels where the trapping and subsequent release of carriers from the recombination centres in the depletion region is comparable to the recombination of carriers in the neutral regions. However, at higher injection levels, this recombination pathway saturates while the recombination in the neutral regions continues to increase and becomes dominant.

(ii) Tunneling current

In a reverse biased junction, filled states of the p -region valence band are energetically on the same level as the empty states of the n -region conduction band, separated only by the width of the depletion region, which serves as a potential

barrier. It is possible for electrons to tunnel directly across the junction from the valence band to the conduction band at sufficiently high reverse voltages, where the potential barrier between the p and n regions is thinned by the large induced electric field[62]. This allows the carriers to more easily overcome the potential barrier. This tunneling current can be described by the following expression:

$$I_T = \frac{\sqrt{2m^*}q^3EV}{4\pi^2\hbar^2\sqrt{E_g}} \exp\left(-\frac{4\sqrt{2m^*}E_g^{3/2}}{3q\hbar E}\right) \quad (2.12)$$

where m^* is the electron effective mass, E is the average field inside the junction, V is the applied reverse voltage, and \hbar is the reduced Planck's constant ($h/2\pi$)[63]. This type of current is significant in highly doped junctions where the depletion region is very narrow and the electric field at the junction very large[62], since the tunneling current has an exponential dependence on the electric field. The tunneling current also depends on the electron effective mass which can vary significantly between different materials, as well as the bandgap energy which gives rise to a very weak temperature dependence of this type of current. Its dependence on both the electric field and the temperature are used to identify the tunneling IV characteristics.

Another tunneling mechanism is indirect trap-assisted tunneling. In this case, a carrier is thermally excited from one of the bands into a trap state (created by impurities or defects), before tunneling through to the other band. This type of tunneling occurs at lower voltages compared to direct tunneling since the carriers have a shorter distance to tunnel[64]. Figure 2.5 shows some of the leakage mechanisms in a reverse-biased $p-i-n$ diode.

(iii) Auger generation

Auger generation is a three-carrier band-to-band process which can take place via several different mechanisms depending on the electronic band structure of the semiconductor in question[65]. In infrared detectors, this typically refers to the thermal generation of carriers via Auger 1 and Auger 7 processes in n - and p -type semiconductors, respectively, where Auger 1 is generally greater[66]. In Auger 1, an

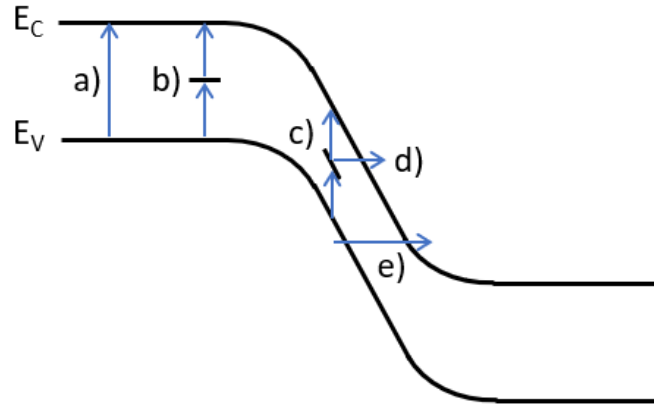


Figure 2.5: Leakage mechanisms in a reverse-biased $p-i-n$ junction diode: a) band-to-band EHP generation, b) trap-assisted generation, c) trap-assisted generation within the depletion region, d) trap-assisted tunneling, e) direct band-to-band tunneling.

electron from the conduction band gives its energy to an electron in the valence band, which is in turn excited to the conduction band leaving behind a heavy hole[48]. Auger processes are dependent on carrier concentration and as such are significant in highly doped structures and at high injection levels and temperatures. Due to the structure and operating conditions of the photodiodes in this work, Auger generation is considered negligible.

(iv) Ohmic losses

Another deviation from the ideal diode equation comes as a result of a voltage drop across imperfect external contacts, or the neutral p and n regions if their resistivity is not sufficiently low, or if the injected minority carrier density is comparable to the majority carrier concentration, i.e. if the current is high enough. In the low current regime, the voltage drop appears almost entirely across the junction. However, as the current increases, the injected minority carrier concentration exceeds the majority carrier concentration, causing an ohmic potential drop across the neutral n and p regions. In this case, the current is once again proportional to $\exp(qV/2kT)$ as is the case with SRH dominated current at much lower injection levels[63]. However,

this is not a concern for photodetector applications since such a diode is typically operated in a low current regime, with the exception of TPV or PV cells where the current is large and the ohmic losses are notable.

Additionally, at such high injection levels, this voltage drop across the neutral n and p regions causes a decrease in junction voltage. The same is true for any voltage drop across external contacts, which is more relevant in photodetector applications. In a simplified case, these ohmic losses can be represented by a resistor, R_s , connected in series with the diode[62]. In this case the junction voltage can be written as $V - IR_s$, and the diode equation becomes:

$$I = I_0(\exp(q(V - IR_s)/nkT) - 1) \quad (2.13)$$

where IR_s is the voltage drop across the neutral regions and/or external contacts represented by the series resistor. Clearly, this voltage drop increases with increasing current through the junction, which in turn causes an increasing difference between applied voltage and junction voltage. The result is a slower increase in current with increasing bias at higher injection levels, i.e. the diode current no longer increases exponentially with applied voltage.

(v) Surface currents

Surface currents are mainly caused by ionic charges on the semiconductor surface collected by its dangling bonds as the material abruptly terminates. These charges induce mirror charges in the semiconductor which leads to the formation of surface channels[63]. This in turn changes the junction depletion region at the surface. The abrupt termination of the surface also creates energy states within the bandgap which increases SRH generation-recombination[64]. Unlike bulk currents which are proportional to the area of the device mesas, surface currents scale with the device perimeter. They can often be the limiting factor of photodetector performance and as such require the development of fabrication techniques to minimise their occurrence. This is often achieved with the passivation of the semiconductor surface, a process in which the surface is chemically treated to minimise the

creation of the conduction channels. Passivation is often followed by (or combined with) encapsulation with a chemically inert and optically transparent insulating material to stabilise the surface. Another option for reducing surface currents is the development of a planar fabrication flow, but this has its own challenges, hence new material technologies are usually initially developed into mesa etched diodes.

These additional conduction paths run parallel to the surface and can be represented by a shunt resistor connected in parallel with the diode. Finally, the total current in the diode can be written as a sum of all of the aforementioned independent contributions as[64]:

$$I = I_0 \left[\exp \frac{q(V - IR_s)}{nkT} - 1 \right] + \frac{V - IR_s}{R_{sh}} + I_T \quad (2.14)$$

where R_{sh} is the shunt resistance due to surface leakage contributions. Different current mechanisms typically dominate at different voltage ranges. Figure 2.6 shows forward and reverse IV characteristics of a *p-i-n* junction diode.

In forward bias and at low current levels, generation-recombination current dominates and $n \approx 2$, at moderate current levels, diffusion current dominates and $n \approx 1$, and at high current levels, high injection occurs and n tends towards 2 once again. At even higher current levels, ohmic losses due to voltage drop across the neutral regions and external contacts reduce voltage drop across the junction leading to a slower increase in current. In reverse bias, generation of carriers within the depletion region and surface effects cause an increase in the overall diode current, so that $I_{diode} > I_0$. Additionally, this reverse saturation current density can be written as a sum of the bulk and surface current contributions as[31]:

$$\frac{I_D}{A} = J_d + J_{g-r} + \left(\frac{P}{A} \right) J_s \quad (2.15)$$

where I_D is the diode current, A is the device area, P is the device perimeter, and J_d , J_{g-r} , and J_s are the reverse saturation current densities due to the diffusion of carriers, generation-recombination of carriers in the depletion region, and the recombination of carriers at the mesa surface, respectively. In a device where bulk

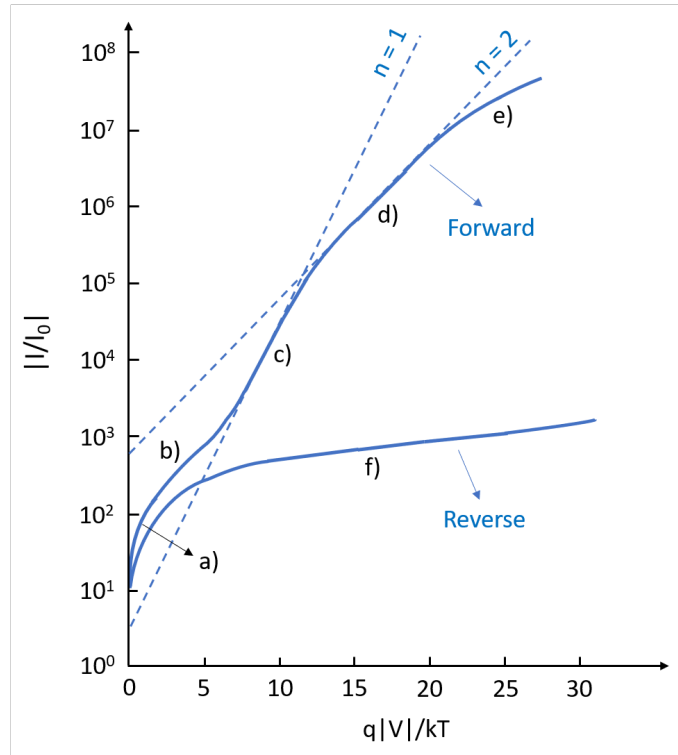


Figure 2.6: IV characteristics of a typical p - i - n junction diode, adapted from Sze et al.[63], showing voltage-dependent leakage mechanisms; a) shunt resistance effects, b) recombination current region, c) diffusion current region, d) high injection region, e) series resistance effects, and f) reverse leakage due to generation current and surface effects.

diffusion and/or generation-recombination currents dominate, the diode current is independent of the P/A ratio. However, if the surface current due to the recombination of carriers at the exposed mesa edges is the dominant source of leakage, then the dark current density increases with decreasing device dimensions, represented by an increasing P/A ratio.

Dynamic resistance

Another useful figure of merit is the dynamic resistance, R_d , defined as dV/dI , often measured at 0 V (the so-called zero bias resistance, R_0). It is often more useful to look at the $R_d A$ product which provides an insight into dynamic resistance relative

to the device size. Similarly to leakage current, dynamic resistance is dependant on the diffusion and generation-recombination bulk currents, as well as surface currents, and can be expressed as a sum of the three. Bhagwat et al.[31] adopted a model that describes the dependence of $1/R_dA$ on P/A ratio developed by Gopal et al.[67], [68] for MCT (mercury cadmium telluride) photodetectors. According to this model, the $1/R_0A$ is given by[31]:

$$\frac{1}{(R_0A)} = \left(\frac{1}{(R_0A)_D} + \frac{1}{(R_0A)_{g-r}} \right) + \left(L_p \frac{1}{(R_0A_s)_s} \right) \left(\frac{P}{A} \right) + \left(\frac{L_p^2}{4} \frac{1}{(R_0A_s)_s} \right) \left(\frac{P}{A} \right)^2 \quad (2.16)$$

where L_p is the minority hole diffusion length, and $(R_0A)_D$, $(R_0A)_{g-r}$, and $(R_0A_s)_s$ are the zero bias resistance area products due to the diffusion of carriers, generation-recombination of carriers, and surface recombination at the exposed mesa edges, respectively. The above model accounts for the fact that the the diffusion length of minority carriers is much greater than the thickness of the p and n regions. In a device with negligible surface leakage, $1/R_0A$ is independent of device dimensions. However, if surface currents are the dominant leakage mechanism, then $1/R_0A$ will increase with increasing P/A ratio, showing a quadratic dependence. The x-axis intercept (at $P/A = 0$), provides the upper R_0A limit that can be achieved for a given material system, assuming an infinite diode with no surface effects. In other words, it provides the R_0A due to the bulk properties alone.

An extension of this model that accounts for angled mesa sidewalls often seen in wet-etched devices has been developed by Prineas[69]. In this case, the $1/R_0A$ can be expressed as:

$$\frac{1}{(R_0A)} = \frac{1}{(R_0A)_D} + \left(L_p \frac{1}{(R_0A_s)_s} \right) \left(\frac{P}{A} \right) + \left(\frac{(L_p - (x_n/\cos\theta))^2}{4} + \frac{x_n^2 \tan^2\theta}{8} \right) \left(\frac{P}{A} \right)^2 \frac{1}{(R_0A_s)_s} \quad (2.17)$$

where x_n is the etch depth past the junction and θ is the angle of the sidewall. As is evident from the above equation, even in devices with angled sidewalls $1/R_0A$ has

a quadratic dependence on P/A if the device is limited by surface leakage.

The dynamic resistance of a photodiode can impact the design of a circuit used to measure or amplify its photocurrent. Hence it is also valuable to characterise and report it to the wider community, in the area normalised R_0A format.

2.2.2.2 Junction capacitance

Another important parameter of a $p-i-n$ photodiode is the junction capacitance due to the dipole in the depletion region which dominates under reverse bias. Junction capacitance is defined as $C = dQ/dV$, where dQ is the incremental change in the depletion region charge per unit area, caused by an incremental change in the applied voltage, dV . In order to maintain overall charge neutrality of the depletion region, the total amount of charges on the p and n sides respectively must remain equal, such that:

$$w_p N_A = w_n N_D \quad (2.18)$$

where w_p and w_n are widths of the depletion region on the p and n sides, respectively. Hence the diode acts as a parallel plate capacitor with an area, A , separated by the width of the depletion region, W . Therefore, the junction capacitance, C , is given by[59], [62]:

$$C = A \frac{\epsilon_0 \epsilon_r}{W} \quad (2.19)$$

According to equation 2.18, the depletion region will extend into the n and p regions unequally if the two layers have different doping levels. If the intrinsic region of the $p-i-n$ junction is lightly p doped, then $N_D \gg N_A$, and the depletion region will extend much further into the p layer. This also means that the intrinsic region will deplete of carriers much quicker due to its several magnitudes lower doping concentration than the surrounding p and n layers.

In such an asymmetrically doped junction, the depletion region will extend almost entirely into the less heavily doped side such that $w_p \approx W$, while $w_n \approx 0$. Since the

total charge, Q , on each side of the depletion region is given by

$$|Q| = qAw_nN_D = qAw_pN_A \quad (2.20)$$

where width of the depletion region given in equation 4.3 can be simplified to

$$W = \sqrt{\frac{2\epsilon_0\epsilon_r}{eN_A}(V_0 - V)} \quad (2.21)$$

in the case where $N_D \gg N_A$, then the total charge in the depletion region is equal to

$$|Q| = A\sqrt{2e\epsilon_0\epsilon_rN_A(V_0 - V)} \quad (2.22)$$

The capacitance of the single sided junction, defined as $|dQ/d(V_0 - V)|$, is then given by:

$$C = \frac{A}{2} \sqrt{\frac{2e\epsilon_0\epsilon_r}{V_0 - V}} N_A \quad (2.23)$$

if $N_D \gg N_A$, or

$$C = \frac{A}{2} \sqrt{\frac{2e\epsilon_0\epsilon_r}{V_0 - V}} N_D \quad (2.24)$$

if $N_A \gg N_D$. Hence it is possible to extract the doping concentration of the lightly doped region from a capacitance measurement, if the applied reverse voltage V is much greater than V_0 [62]. The doping concentration is then given by:

$$N_{A,D} = \frac{2C^2V}{eA^2\epsilon_0\epsilon_r} \quad (2.25)$$

2.2.3 Quantum efficiency

The external quantum efficiency (EQE), η , of a photodetector is defined as a fraction of charge carriers generated for each incident photon that flow in the external circuit[47], and is given by:

$$\eta = I_{pc} \frac{h\nu}{eP} = I_{pc} \frac{1.24}{P\lambda} \quad (2.26)$$

where I_{pc} is the photocurrent, P is the incident optical power, and λ is the wavelength in micrometers. A quantum efficiency of 1 would imply that every incident photon on the detector produces one EHP that contributes to the external current. However, EQE of a photodetector is always less than unity due to reflection losses at the top surface as well as absorption of photons outside of the depletion region where they can recombine without being collected by the electric field of the p - n junction. Even photogenerated carriers in the depletion region can recombine or fall into traps without contributing to the photocurrent[56]. The internal quantum efficiency is defined as the number of photogenerated EHPs per *absorbed* photon and is a good indicator of the material and device quality which influences the detector's ability to convert optical input into electrical signal.

Responsivity of a photodetector, R , is defined as the photocurrent (number of photogenerated carriers) produced for a given optical power and is related to the external quantum efficiency through[58]:

$$R = \frac{I_{pc}}{P} = \frac{\eta\lambda}{h\nu} = \frac{\eta\lambda}{1.24} [\text{A/W}] \quad (2.27)$$

Both responsivity and quantum efficiency initially increase with increasing photon energy with the peak located close to the bandgap energy, before gradually decreasing due to the absorption of photons outside of the depletion region[58]. As mentioned previously, at higher photon energies fewer EHPs are created in the depletion region as more light is being absorbed in the top p layer, since the fraction of light absorbed in the length of the material, t , is equal to $(1 - e^{-\alpha t})$, assuming no reflection at the top surface[47].

2.2.4 Specific detectivity

Another important device parameter is the specific detectivity, D^* , which considers both the responsivity and leakage current in order to characterise the signal-to-noise

performance of a detector. It is given by:

$$D^*(\lambda) = \frac{R(\lambda)}{\sqrt{\frac{4kT}{R_d A} + 2qJ}} \quad (2.28)$$

where J is the dark current density. Specific detectivity is also often defined as the reciprocal of the noise-equivalent power, $D^* = 1/NEP$, where NEP is the minimum power needed to produce a signal above the noise floor of the device[70]. Equation 2.28 takes into account both Johnson and shot noise, where the former is associated with thermal noise in the detector and the latter is noise due to fluctuations in the movement of charge across a junction or interface [51]. Another possible source of noise in photodetectors is flicker noise defined as $1/f$, which is caused by traps that stem from impurities and crystal defects as well as dangling bonds, and is associated with current flow[71], [72]. It is difficult to quantify flicker noise as it depends on the crystal imperfections in a given device, which often varies between devices even from the same wafer[71]. Due to its strong dependence on frequency it often dominates over Johnson and Shot noise at lower frequencies[72]. It is also strongly temperature and bias dependent, i.e. flicker noise increases with increasing bias[73]. Flicker noise has not been characterised in the photodiodes presented in this work, but can often lead to detectors having more noise than is considered in the above approximation.

Chapter 3

Literature Review

This chapter provides a summary of relevant literature on GaSb-based photodetectors. The first section outlines the growth and fabrication issues of GaSb photodetectors with a focus on the origin of native defects and leakage currents. The second section focuses on the InGaAsSb material system, outlining growth challenges and summarizing the progress achieved in InGaAsSb-based photodetectors.

3.1 GaSb

GaSb, with a cutoff wavelength of $1.7 \mu\text{m}$ (0.73 eV bandgap), has routinely demonstrated poor detector performance due to various growth and fabrication limitations. Epitaxially grown GaSb suffers from high background doping concentrations, while GaSb-based devices exhibit large unwanted dark currents. Despite these issues, it remains an integral part of many semiconductor heterostructures/optoelectronic devices with various applications in the near and mid-IR.

Nominally undoped epitaxial GaSb is known to always be *p*-type regardless of growth conditions and technique employed[20], [74]–[77], with a typical carrier concentration on the order of $10^{16} - 10^{17} \text{ cm}^{-3}$ [74], [77]–[79]. It has been well-established that this *p*-type conductivity originates from native defects in GaSb rather than impurities introduced during crystal growth[74], [76]. The origin and the

nature of such defects has been studied in great detail over the years, and is believed to be related to Sb vacancies and Ga_{Sb} antisites (Ga on Sb site)[80]. Longenbach and Wang[81] have proposed that it is the low vapor pressure of antimony and the resulting low surface mobility of Sb atoms during crystal growth that causes the Sb atoms to aggregate together forming clusters and precipitates. This leads to the creation of Sb vacancies which can become occupied by Ga atoms, finally resulting in the formation of Ga_{Sb} antisite defects which are responsible for the p -type conductivity in GaSb. Moreover, several experiments have been conducted in an attempt to minimise the occurrence of native defects in GaSb and produce samples with reduced background doping concentrations.

Lee et al.[75] investigated the effect of substrate temperature and excess antimony flux on both optical and electrical properties of MBE-grown GaSb layers and have found that the best material quality is achieved with the minimum excess antimony flux at a particular growth temperature, with the lowest background doping of $7.8 \times 10^{15} \text{ cm}^{-3}$ achieved. Similarly, Chidley et al.[76] studied the effect of growth temperature and V/III ratio on the material quality in organometallic vapour phase epitaxy (OMVPE) grown GaSb samples and have found that the latter can be used to minimise the native defect density and in turn produce samples with better optical and electrical properties. Although a higher V/III ratio was found to produce samples of higher quality, the highest ratio used was only ~ 2 , hence more data is needed to establish the effect excess Sb on material quality. Similar investigation has been conducted on liquid phase epitaxy (LPE) grown GaSb by Anayama et al.[80] who studied the effect of growth temperature and solution composition on the background carrier concentration. They found that reducing the growth temperature below 600°C and growing from Sb-rich solutions significantly reduced the native defects in the material, producing GaSb layers with carrier concentration as low as $2 \times 10^{15} \text{ cm}^{-3}$ at 590°C . While growing from a liquid phase is substantially different than growing from a vapour phase, it emphasises the importance of carefully controlling the V/III ratio regardless of the growth technique employed.

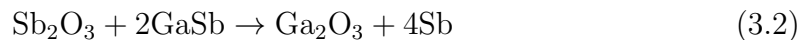
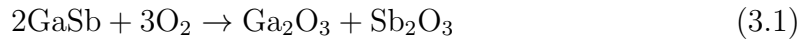
However, there are some contradictory results. A later experiment conducted by Turner et al.[77] showed little to no effect of varying the growth temperature and V/III beam-equivalent pressure (BEP) ratio on the background carrier concentration in MBE-grown GaSb samples. A similar observation was made a year later by Baraldi et al.[82] who found that the background hole concentration was almost independent of the BEP ratios in MBE-grown GaSb layers. In a more recent experimental study, Lazzari et al.[46] confirmed that growing GaSb via LPE from an Sb-rich phase and at lower temperatures reduced the background doping. Additionally, *n*-type conductivity believed to be a result of extrinsic impurities was achieved at very low temperatures. However, they did not find a notable variation in the background doping in MBE-grown GaSb layers when varying growth temperature and V/III ratio, but the small range of parameters used might have prevented noticeable change. As a result of their study, they highlight the need for developing a solid-vapor thermodynamical model for MBE-grown GaSb which takes into account the evaporation of Sb from the surface during growth in order to accurately describe the defect formation process.

Several theoretical studies employing different iterations of the hybrid density-functional theory (DFT) model have been carried out in an attempt to identify the dominant native defect responsible for the *p*-type background in GaSb, and predict the concentration of such defects under different growth conditions. Hakala et al.[83] have found, in line with previous research, that the dominant native defect is indeed the Ga_{Sb} antisite which acts as an acceptor. Another result of their calculation is a decrease in the residual hole concentration in Sb-rich conditions as well as lower growth temperatures. Later theoretical work conducted by Virkkala et al.[84] agrees with the Ga_{Sb} antisite defect being the dominant source of the background hole concentration, but only in Ga-rich growth conditions. They also predict a decrease in Ga_{Sb} antisites and a corresponding reduction in the *p*-type conductivity when moving towards Sb-rich conditions. However, counter to experimental findings, the model also predicts Sb_{Ga} antisite becoming the dominant defect in Sb-rich growth

conditions, which would result in the background doping of GaSb switching from p - to n -type when grown under such conditions. More recently, Buckeridge et al.[85] have reached a similar conclusion. Their results show that GaSb will be p -type in Sb-poor conditions, but semi-insulating when grown in Sb-rich conditions due to the compensating nature of the Sb_{Ga} antisite. In an attempt to explain the discrepancy between the calculations and experiment, they proposed that the formation of the compensating Sb_{Ga} defect might be suppressed in non-equilibrium growth techniques or other unwanted p -type impurities might be introduced during growth.

Despite some discrepancies in theoretical calculations, several other experiments employing positron lifetime spectroscopy (PAS) have been carried out in the meantime, all further supporting the conclusion that the Ga_{Sb} antisite is the dominant native defect responsible for background p -type conductivity in nominally undoped GaSb[79], [86], [87].

Beside the growth challenges, one is also faced with fabrication challenges of GaSb devices, namely the high surface leakage present in most Sb-based alloys which was shown to be the main contribution to the overall dark current in Sb-based photodetectors[19]. The GaSb surface is highly reactive and is covered in a layer of native oxides, a mixture of Sb_2O_3 and Ga_2O_3 , when exposed to air. The Sb_2O_3 then spontaneously reacts with GaSb to produce Ga_2O_3 and a layer of free Sb which is responsible for the material's high surface conductivity[69], [88]. It increases both surface recombination velocity and surface leakage by creating additional conduction paths parallel to the surface[89]. This reaction is given by:



Lin et al.[90] confirmed through XPS studies that applying a common etching procedure to the GaSb surface increases oxidisation and generation of the thin metallic layer of elemental Sb. Hence surface passivation is a crucial step in the development of GaSb technology[20], [89], [91]. While numerous etching, passivation

and capping techniques have been developed over the years to suppress surface leakage in Sb-based photodetectors with various degrees of success[20], [89]–[96], GaSb continues to under-perform compared to its much more developed counterpart InGaAs with a similar bandgap of 0.75 eV when grown lattice-matched to InP.

3.2 InGaAsSb

3.2.1 Growth of $\text{In}_x\text{Ga}_{1-x}\text{As}_y\text{Sb}_{1-y}$ alloys

$\text{In}_x\text{Ga}_{1-x}\text{As}_y\text{Sb}_{1-y}$ alloy has been studied as a promising material system since the second half of the 20th century for a range of IR applications, including optical fibers[97], [98], light emitting diodes[25], [26], lasers[27], [28], thermophotovoltaic cells[23], [24], and detectors[21], [22], [99]. What makes this material system so attractive is its highly flexible bandgap which can be tuned for wavelengths between 1.7 μm and 4.9 μm whilst remaining lattice-matched to GaSb[18]. However, the growth of In_xGaAsSb alloys is limited by the existence of a large miscibility gap - a region where the constituent binaries are not miscible, i.e. do not mix, which restricts the usable bandgap range[18], [33]. Within this miscibility gap, the alloy is metastable and is subject to spinodal decomposition which refers to the spontaneous separation of the alloy into individual phases, i.e. it decomposes into a mixture of GaAs- and InSb-rich quaternary phases[36], [37], which in turn degrades its structural, optical, and electrical properties[33]. It should be noted here, that the $\text{In}_x\text{Ga}_{1-x}\text{As}_y\text{Sb}_{1-y}$ samples discussed in this and later sections are grown lattice-matched to GaSb substrates, and as such the corresponding As (y) fractions can be calculated according to $(\text{GaSb})_{1-x}(\text{InAs}_{0.91}\text{Sb}_{0.09})_x$ [100].

The existence of the miscibility gap was first predicted by various thermodynamic models, and later confirmed via experiment, however, the exact boundaries of this region are not precisely known and are found to vary between different models and experiments[18], [35]. When growing InGaAsSb layers at temperatures below the critical temperature, T_C , and equilibrium conditions, the alloy decomposes into a

mixture of individual phases due to a large positive enthalpy of mixing[36], [37]. This critical temperature was found to be 1461°C for InGaAsSb[101], which is significantly higher than typical growth temperatures. The range of compositions that can be grown before encountering phase separation are found to be dependant on the specific growth technique and conditions employed. It is especially challenging to grow InGaAsSb alloys via liquid phase epitaxy as it requires near-equilibrium growth conditions[36]. Nakajima et al.[102] have experimentally determined the phase diagram of the InGaAsSb quaternary system via LPE and have estimated the location of the miscibility gap to be $0.3 < x < 0.6$ for growth temperatures between 600°C - 800°C, although the exact location could not be determined as the layers were not grown under constant equilibrium conditions. In a later experiment, DeWinter et al.[97] have demonstrated LPE-growth of In_xGaAsSb layers at a lower growth temperature of 530°C with In fractions up to 0.22 before encountering phase separation, where the growth of alloys with $x > 0.22$ was shown impossible. While the range of alloy compositions obtainable via LPE did expand over the years as a result of fine-tuning of the growth parameters[29], [30], [103], it still remains severely limited by the thermodynamically driven phase separation. Figure 3.1 shows an example of the InGaAsSb phase diagram with the estimate of the miscibility gap included, as inferred from LPE-growth of these alloys[104].

However, it is possible to grow metastable alloys via non-equilibrium growth techniques such as OMVPE and MBE where one can exploit the kinetic limitations of atomic rearrangement on the growth surface and suppress the phase separation[37]. C.A. Wang extensively studied the growth of InGaAsSb via OMVPE across a wide composition range and has found that the phase separation, while it could not be entirely eliminated, could be greatly reduced by manipulating the growth kinetics[33]. In a variety of different experiments, Wang et al. showed that growing In_xGaAsSb layers with increasing x fractions resulted in significant broadening of photoluminescence (PL) emission peaks and their reduced intensity or even disappearance due to an increased degree of phase separation present as one

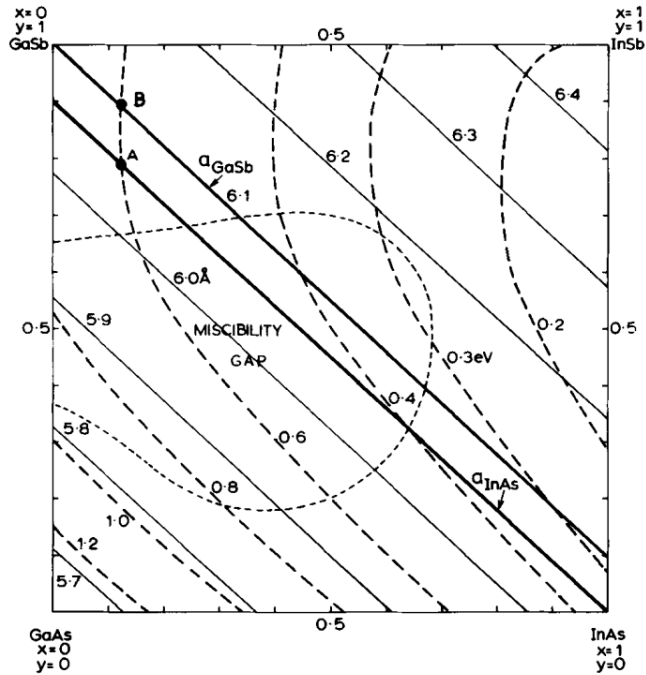


Figure 3.1: Phase diagram of $\text{In}_x\text{Ga}_{1-x}\text{As}_{1-y}\text{Sb}_y$, taken from reference [104]. The solid lines correspond to compositions lattice matched to GaSb and InAs. The immiscibility region predicted by the author’s calculations is indicated on the graph.

penetrates further into the miscibility gap and the alloys become increasingly metastable[33], [34], [45], [105]–[109]. As expected, surface morphology deteriorates and increased compositional variation with GaAs- and InSb-rich regions is present in samples with higher In fractions[33], [34]. However, it was found that reducing the growth temperature from 575°C to 550°C and 525°C produced samples with smoother surfaces and narrower PL emission peaks[34], [107]. Furthermore, increasing the growth rate from 1.2 to 5 $\mu\text{m}/\text{h}$, and even using intentionally miscut substrates noticeably improved the material quality[105], [107]. Typically, growth of InGaAsSb layers is performed on GaSb substrates with a (100) orientation which was found to be most favourable for growth of these alloys. However, Wang et al. performed growth on (100) GaSb substrates with miscut angles of 2° toward (101) or 6° toward (111)B. It was concluded that lowering the growth temperature, increasing the growth rate, and using miscut substrates reduces the adatom diffusion length and

limits the extent of phase separation which becomes too slow to occur on the growth surface[36], [107]. In other words, surface kinetics limits the thermodynamically driven phase separation[34], something that could not be achieved in LPE growth.

Similar observations were made in later MBE studies. Semenov et al.[35] grew In_xGaAsSb layers with $0.12 < x < 0.25$ at 500°C via MBE and noted a clear degradation of structural and optical properties in alloys with increasing In fractions. Samples with $x \geq 0.20$ exhibited a significant drop in PL intensity and a much broader FWHM. Growing thicker layers of such metastable alloys resulted in the disappearance of the PL peaks as well as significant broadening of XRD peaks. SEM images showed distinct regions rich with As and Sb, i.e. spinodal decomposition occurred. Similarly to OMVPE, it was shown that controlling the V/III flux ratio and reducing the growth temperature improved the quality of metastable alloys and allowed growth of samples with In fractions as high as 25% with improved structural and optical properties. In a more recent study, Yildirim et al.[18] demonstrated it is possible to suppress phase separation in MBE-grown In_xGaAsSb layers across the entire composition range with $0 < x < 1$ by lowering the growth temperature even further to $410 - 450^\circ\text{C}$, and in turn limiting the adatom diffusion length. In general, lower growth temperatures are possible in MBE compared to OMVPE partly because adatoms do not require the thermal energy to separate from a precursor[18]. Although there were still some noticeable changes in surface morphology and PL spectra, these were correlated with increasing In fractions in the alloy rather than phase separation. All samples were reported to be highly uniform and defect free with no signs of phase separation across the entire compositional range as evidenced by the XRD and transmission electron microscopy (TEM) measurements. However, further optical and electrical properties were not investigated. It was concluded that, while limiting the adatom diffusion length suppresses phase separation, it can also lead to the formation of defects and loss of crystallinity if it becomes too short, providing a lower limit for growth temperature[110]. Yildirim et al. found in a similar experiment that phase separation could also be controlled by

introducing strain during growth. Increasing strain was shown to decrease the critical temperature below which spinodal decomposition occurs in metastable alloys, therefore even for alloys grown at higher temperature phase separation could be reduced[110].

3.2.2 Optical parameters

As the importance of the InGaAsSb alloy grew, so did the need for characterising its optical properties to allow for accurate structure design and device modelling. Experimental data available on the bandgap energy is largely contradictory, while theoretical models rely on interpolation schemes and pre-existing data on III-V binary and ternary compounds. Both refractive index and absorption coefficient data are scarce, while most work focuses on theoretical models with limited success. The following section will summarise previous research on optical characteristics of InGaAsSb.

Bandgap energy

A considerable amount of effort has been put into calculating various III-V ternary and quaternary alloy parameters over the years. Since no theory exists that accurately describes these, one has to rely on interpolation schemes to derive such parameters. In the simplest case, a given ternary or quaternary alloy parameter can be described by Vegard's law which assumes a linear interpolation between the binary and/or ternary end points[111]. This is believed to hold true for lattice parameters[112], however, Thompson and Woolley[113] showed that the bandgap energies of common ternary III-V alloys exhibited a non-linear (in most cases approximately quadratic) dependence on composition, also known as bowing. Hence a bowing parameter, C , was introduced to account for this deviation from a simple linear trend. This principle was later extended to quaternary III-V alloys which showed a similar behaviour, leading to the development of many interpolation schemes in the following years[100], [111], [114], [115].

One of the earliest such interpolation methods developed by Moon et al.[114] which assumed the quaternary bowing is the sum of the bowing of each sublattice, provided a good fit to experimental data available at the time. A few years later, Glisson et al.[111] developed a similar interpolation scheme, but with smaller bowing of the quaternary bandgap. Many subsequent interpolation methods have been developed over the years, but it was believed that the one proposed by Glisson provided the closest fit to experimental data[100]. This led to Vurgaftman et al.[100] calculating the dependence of the bandgap energy of InGaAsSb on composition on the basis of Glisson's work, as illustrated in figure 3.2.

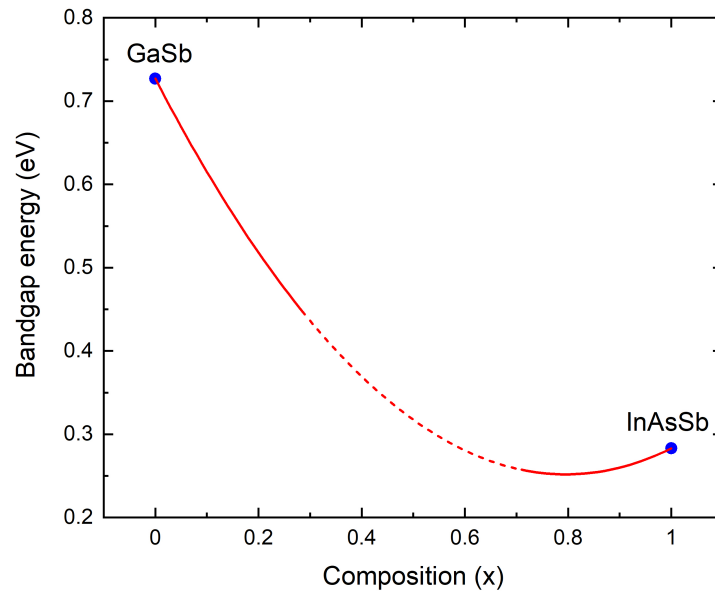


Figure 3.2: Bandgap energy variation with composition, x , for $(\text{GaSb})_{1-x}(\text{InAs}_{0.91}\text{Sb}_{0.09})_x$ according to Vurgaftman[100]. Dashed line indicates the location of the miscibility gap.

They suggested a bandgap bowing parameter of 0.75 eV, which was the average value of all bowing parameters available in literature at the time. The authors provide the following relationship:

$$E_g = [0.727(1 - x) + 0.283x - 0.75x(1 - x)]eV \quad (3.3)$$

for $(\text{GaSb})_{1-x}(\text{InAs}_{0.91}\text{Sb}_{0.09})_x$ (lattice-matched to GaSb) at 300 K.

In addition to theoretical calculations, the bandgap of InGaAsSb has also been investigated experimentally. DeWinter et al.[97] measured bandgap energies of LPE-grown $\text{In}_x\text{Ga}_{1-x}\text{As}_y\text{Sb}_{1-y}$ alloys with $0 \leq x \lesssim 0.22$ before encountering the miscibility gap. They found through both photoluminescence and transmission measurements a decrease in the bandgap energy from 0.73 eV measured in GaSb to 0.53 eV measured in $\text{In}_{0.22}\text{GaAsSb}$. Their data was in good agreement with the calculation given by Moon et al. for compositions with $x \lesssim 0.15$, however, for higher alloy fractions they measure a higher bandgap energy than predicted by Moon. That same year, Astles et al.[104] measured bandgap energies of LPE-grown $\text{In}_x\text{Ga}_{1-x}\text{As}_y\text{Sb}_{1-y}$ layers with $0.07 \lesssim x \lesssim 0.15$. The bandgap energy was found to reduce from 0.65 eV in $\text{In}_{0.071}\text{GaAsSb}$, to 0.56 eV in $\text{In}_{0.180}\text{GaAsSb}$, as inferred through absorption measurements. Cherg et al.[116], [117] grew $\text{In}_x\text{Ga}_{1-x}\text{As}_y\text{Sb}_{1-y}$ alloys via OMVPE on various substrates to achieve a wider range of compositions with $0.29 \leq x \leq 0.83$. The bandgap energy of $\text{In}_{0.32}\text{GaAsSb}$ grown on GaSb was estimated from PL measurements to be 0.442 eV. A few years later, Wen'gang and Aizhen [41] grew $\text{In}_x\text{Ga}_{1-x}\text{As}_y\text{Sb}_{1-y}$ samples with $0.047 \leq x \leq 0.395$ via MBE on GaAs substrates. The bandgap energies calculated from transmission measurements were found to vary between 0.68 eV in $\text{In}_{0.047}\text{GaAsSb}$ to 0.419 eV in $\text{In}_{0.395}\text{GaAsSb}$. Their results were in decent agreement with the calculation given by Moon, however, similarly to DeWinter, they found that the measured values were higher than the calculated ones, which was believed to be a result of residual strain in the system since the samples are grown on GaAs substrates. A similar conclusion was reached by Li et al.[44] who grew $\text{In}_x\text{Ga}_{1-x}\text{As}_y\text{Sb}_{1-y}$ samples with $0.18 \lesssim x \lesssim 0.26$ via MBE on both GaSb and GaAs substrates. The bandgap energies, estimated from transmission data, varied between 0.540 eV measured in $\text{In}_{0.178}\text{GaAsSb}$ and 0.544 eV measured in $\text{In}_{0.259}\text{GaAsSb}$, and were slightly higher than Moon's calculation. Wang

et al.[106] estimated the bandgap energies of OMVPE-grown $\text{In}_x\text{Ga}_{1-x}\text{As}_y\text{Sb}_{1-y}$ samples with $0.11 \leq x \leq 0.20$ from PL measurements, and have found that the bandgap reduced from 0.593 eV to 0.499 eV. More recently, Rakovics et al.[118] grew InGaAsSb samples via LPE on GaSb substrates over a wider range of compositions with $0 \leq x \leq 0.20$. The bandgap energy, determined via transmission measurements, reduced from 0.667 eV in $\text{In}_{0.043}\text{GaAsSb}$ to 0.550 eV in $\text{In}_{0.204}\text{GaAsSb}$. The authors proposed a bowing parameter of 0.71 eV, lower than the value recommended by Vurgaftman. The above data is summarised in figure 3.3. Please note that this figure does not include the most recent studies on single alloy detector structures, but rather focuses on any studies that investigate the variation of the bandgap energy with alloy composition.

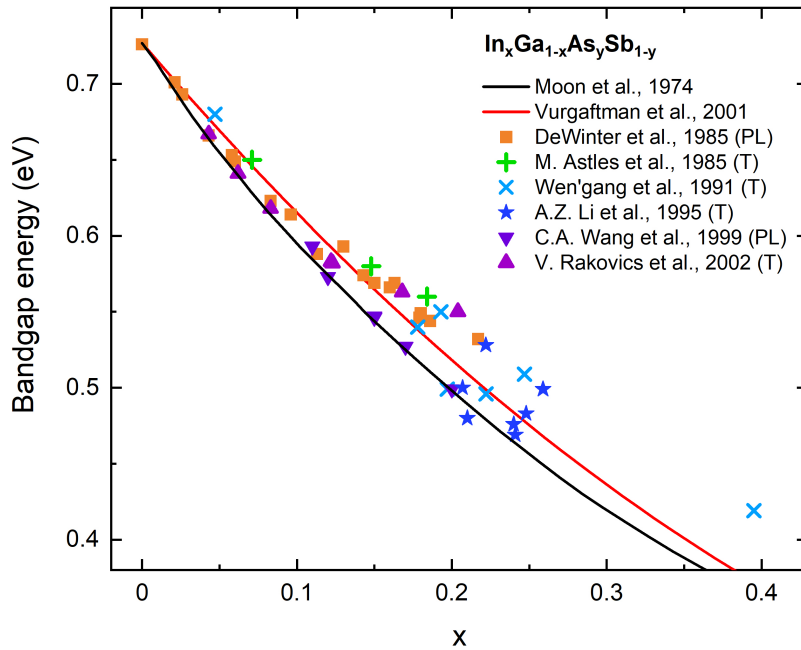


Figure 3.3: Bandgap energy variation with alloy composition for $\text{In}_x\text{Ga}_{1-x}\text{As}_y\text{Sb}_{1-y}$. Solid lines represent interpolation schemes proposed by Moon (black) and Vurgaftman (red). Symbols show experimental data available in literature.

Absorption coefficient

Several models have been developed for calculating the absorption coefficient of InGaAsSb[23], [119]–[122], however these are generally in poor agreement with one another and lack detail and accuracy around the band edge. Moreover, experimental data for the absorption coefficient of InGaAsSb remains scarce, and is focused mainly on alloys with higher In fractions.

Wengang et al.[123] were one of the first authors to measure the absorption coefficient of MBE-grown In_xGaAsSb with $x = 0.266$ via IR spectroscopy. They found, in agreement with theory, that for energies below the band edge, the absorption coefficient increases exponentially with $h\nu$, whereas for energies above the band edge the absorption coefficient increases according to equation 2.6 with $n \sim 1/2$, thus confirming that InGaAsSb is a direct gap material. However, their data does not extend much beyond the band edge. Munoz et al.[42] have measured the absorption coefficient of OMVPE-grown In_xGaAsSb with $x = 0.15$ and 0.16 via spectral ellipsometry for a much wider range of energies, up to 5.3 eV. A few years later, Rakovics et al.[118] have calculated the absorption coefficient of LPE-grown In_xGaAsSb with $x = 0.168$ from transmission measurements. Similarly to Wengang, they found that the absorption coefficient varies exponentially with energy below the absorption edge, i.e. an Urbach tail is present. Likewise, the above bandgap absorption fits well to the expression 2.6, with $n \sim 1/2$. Anikeev et al[124] and Li et al.[99] have measured the absorption coefficient in OMVPE-grown $\text{In}_{0.15}\text{GaAsSb}$ and MBE-grown $\text{In}_{0.22}\text{GaAsSb}$ respectively, however, no further analysis is presented. The above theoretical and experimental data is shown in figures 3.4b and 3.4a, respectively.

3.3 InGaAsSb detectors

The InGaAsSb material system has been investigated for various device applications over the years, with a focus on near- and mid-infrared photodetectors as well as

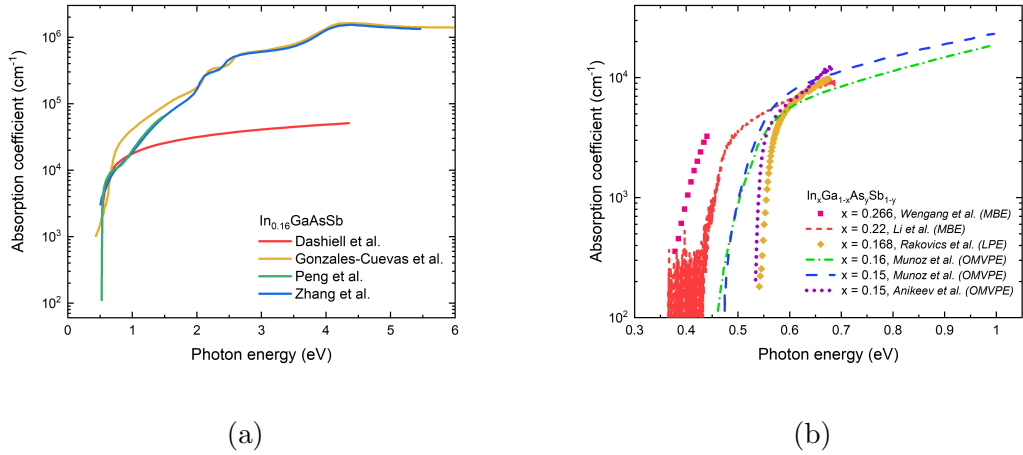


Figure 3.4: (a) Various theoretical models for the absorption coefficient of In_{0.16}GaAsSb. (b) Measured absorption coefficient of In_xGa_{1-x}As_ySb_{1-y} with $0.15 \leq x \leq 0.266$ grown by various techniques.

TPVs[23], [24], [45], [106], [108], [125]–[127]. The most commonly investigated detector structure that employs this material system is a homojunction p - n [31], [69], [128]–[131] or p - i - n [44], [99], [132]–[135] diode, although heterojunction photodiodes have also been researched[35], [43], [60], [61], [136], [137]. In more recent years, there has been an increased interest in barrier detectors as a low-leakage alternative to traditional junction diode detectors[2], [22], [26], [138]–[142]. However, despite the increased interest in InGaAsSb, the focus remains on high In fraction alloys with no study to date that investigates the detector performance across the full alloy range. The following section summarises InGaAsSb photodetector performance with a focus on leakage currents, quantum efficiency, and specific detectivity. Note that the following studies were performed at room temperature, if the temperature is not otherwise stated.

Heterojunction photodetectors

The first InGaAsSb-based photodetector was reported by Srivastava et al.[137] in 1986. The back-illuminated mesa-type p - n InGaAsSb/GaSb photodiodes were

grown via LPE on *n*-type GaSb. The InGaAsSb layer was grown with an In fraction of 18%. The devices exhibited a soft breakdown under reverse bias, with dark currents between 50 and 100 μA . The room temperature voltage dependent quantum efficiency increased from 44% at zero bias to 67% at -0.1 V and 2.2 μm . The specific detectivity of 7×10^9 Jones at 2.2 μm was measured at zero bias and room temperature. Several other heterojunction *p-n* InGaAsSb photodiodes have been reported over the years, often with the addition of a passivating AlGaAsSb window layer which reduces the loss of photo-generated carriers via surface recombination[60], [61]. The dominant dark current mechanism in these heterostructures was reported to be bulk generation-recombination[43], [60], [61], [136].

Homojunction photodiodes

Several homojunction *p-n* and *p-i-n* InGaAsSb photodiodes have been reported over the years, with In fractions between 13 and 30%. Although these structures are most commonly grown on GaSb substrates, growth on mismatched GaAs substrates was also shown possible[135]. A wide bandgap passivating AlGaAsSb top window layer was often employed to reduce unwanted leakage. Furthermore, both front and back illuminated photodiodes were realized, with similar optical and electrical properties[134].

Li et al.[44] reported the first growth of InGaAsSb *p-i-n* homojunction photodiodes via MBE with In fractions between 15 and 26%. The front-illuminated devices with a 2.6 μm cut-off were encapsulated in a polyimide, and measured a specific detectivity of 3×10^9 Jones and a maximum EQE of 65% at 2.5 μm and room temperature. No further analysis of dark current mechanisms were carried out.

A few years later, Shellenbarger et al.[143] have grown InGaAsSb *p-n* photodiodes via LPE with an In fraction of 15%. The devices were encapsulated with a photosensitive polyimide layer in order to insulate the junction and passivate the mesa edges. The authors noted a significant improvement in dark current profiles of

photodiodes with the addition of a wide bandgap AlGa(As)Sb window layer which reduced surface recombination. While the peak responsivity reduced slightly from 0.70 A/W to 0.62 A/W with the addition of an AlGaAsSb window layer, both the saturation current and the zero-bias dynamic resistance-area product improved from 2.1 to 1.0 μA and from 44 to 108 Ωcm^2 , respectively. This resulted in an increase in specific detectivity from 3.6 to 5.0×10^{10} Jones.

A similar observation was made by Lin et al.[133] a few years later in MBE-grown InGaAsSb *p-i-n* photodiodes with an In fraction of 17%. Although the dark current reduced significantly due to the suppression of surface recombination with the addition of the AlGaAsSb window layer, the specific detectivity remained unchanged at $\sim 5 \times 10^8$ Jones. Likewise, due to the suppression of surface currents, the zero-bias resistance-area product increased from 56.3 to 76.4 Ωcm^2 with the addition of the window layer.

Reddy et al.[134] reported on MBE-growth and fabrication of the first back-illuminated InGaAsSb *p-i-n* photodiodes with In fractions between 15 and 23%. The R_0A product decreased from 2.2 to 1 Ωcm^2 in the B-I (back-illuminated) diodes with an In fraction of 21%, compared to the F-I (front-illuminated) ones. It was also shown from the R_0A dependence on mesa dimensions that the devices are limited by side wall leakage. A larger maximum responsivity of 1.19 A/W was seen in the B-I devices, compared to 1 A/W measured in the F-I diodes at 2.2-2.35 μm . This corresponds to a maximum EQE of 65 and 62%, respectively. This increase in responsivity in the B-I case was attributed to photon recycling due to the reflection at the back metal of photons that were not initially absorbed in the active layer, as well as absorption of photons near the active layer/substrate interface which leads to a reduced surface recombination. Furthermore, the incoming light is not obstructed by contact layers, as is the case in the F-I devices. In conclusion, the authors successfully realized the first B-I InGaAsSb photodiodes with electrical properties comparable to their F-I counterparts.

Bhagwat et al.[31] were the first to investigate the contribution of bulk and

surface leakage currents in InGaAsSb photodiodes by adapting a model originally developed by Gopal et al.[67], [68] for mercury cadmium telluride (MCT)- based detectors. The model separates bulk diffusion, bulk g-r, and surface g-r which were found to be the leading dark current contributions to overall leakage. Bhagwat adapted the model by accounting for the fact that diffusion length of minority carriers is much greater than the thickness of the p and n regions. It was shown that, in a surface leakage dominated device, both the saturation current density, as well as $1/R_0A$ increase with decreasing device dimensions (increasing P/A ratio), where the latter exhibits a quadratic dependence. On the other hand, in devices dominated by bulk leakage, $1/R_0A$ is independent of the P/A ratio. The subsequent characterisation of MOCVD-grown $\text{In}_{0.13}\text{GaAsSb}$ p - n photodiodes unveiled a increase in both the saturation current density and $1/R_0A$ with increasing P/A ratio, confirming that InGaAsSb photodiodes are indeed limited by surface leakage. The surface recombination velocity was shown to be relatively high indicating a high density of surface states at the exposed mesa edges.

A similar observation was made by Prineas et al.[69] in MBE-grown $\text{In}_{0.20}\text{GaAsSb}$ back-illuminated p - n photodiodes. The largest R_0A and responsivity were measured to be $25 \Omega\text{cm}^2$ and 0.8 A/W , respectively, which gives a peak specific detectivity of 6×10^{10} Jones. The devices exhibited a strong dependence of R_0A on P/A indicating that sidewall leakage is the dominant dark current mechanism. Prineas adapted the pre-existing models from Gupal and Bhagwat for undercut mesas with angled sidewalls which is often the case in wet-etched devices. It was shown that, even in mesas with angled sidewalls, $1/R_0A$ also has a quadratic dependence on P/A ratio. Furthermore, the authors applied a leakage model to their measured J-V data which separates bulk diffusion, bulk g-r, and surface g-r currents. The subsequent analysis of voltage dependence of current density confirmed that the main surface leakage mechanism is generation-recombination at mesa sidewalls. Once again, the sidewall surface recombination velocity obtained from the fit was found to be relatively high. The diffusion current dominates only at large enough forward biases. Furthermore,

a degradation of the J-V characteristics was noted in 6 month aged devices, where Ohmic leakage due to shunt resistance was found to play an important role, and in fact become the dominant leakage mechanism in these devices. This is believed to be due to the build-up of oxides at the mesa sidewalls. The results of their work once again highlight the need for adequate passivation and encapsulation of mesas to limit surface g-r and ohmic leakage.

One of the best-performing InGaAsSb *p-i-n* photodiodes was reported by Nunna et al.[135]. The photodiodes with an In fraction of 18% were successfully (MBE) grown on mismatched GaAs substrates for the first time via the interfacial misfit (IMF) dislocation array technique. The authors report a significant reduction of surface leakage currents in freshly wet-etched mesas that were treated with an HCl-based etchant to reduce the oxide layer and encapsulated in SU-8 photoresist. An improvement was also noted in dry-etched photodiodes, though to a lesser degree, after the treatment with HCl and SU-8. The best dark current density of $34 \mu\text{A}/\text{cm}^2$ at -10 mV was achieved in a dry-etched passivated device. Both the dry- and wet-etched devices measure the highest R_0A products of 260 and $220 \Omega\text{cm}^2$, respectively. Interestingly, while the passivated wet-etched devices still appear to be limited by surface currents due to a noted dependence of $1/R_0A$ on P/A ratio, the $1/R_0A$ of dry-etched devices is almost independent of P/A, indicating that the main source of leakage are bulk currents. The peak responsivity of 0.8 A/W, corresponding to an internal quantum efficiency of 74%, was reached at $2 \mu\text{m}$. The peak specific detectivity of 4.5×10^{10} Jones was achieved at zero bias.

Hurtado-Castañeda et al.[130] reported on LPE-growth of back-illuminated $\text{In}_{0.14}\text{GaAsSb}$ *p-n* photodiodes. The devices were passivated with an aqueous solution of sodium sulfide to reduce the impact of surface oxidation. The devices measured a relatively low R_0A product of $2.49 \Omega\text{cm}^2$ at room temperature. The authors investigated the dominant leakage mechanisms in InGaAsSb photodiodes at different temperatures through the analysis of the temperature variation of R_0A . While the dominant processes in the passivated devices at medium and high

temperatures were found to be diffusion and g-r currents, at very low temperatures (< 60 K) the device performance was limited by trap-assisted tunneling.

More recently, Shafir et al.[131] grew InGaAsSb p - n photodiodes via MBE with an In fraction of 23%. The front-illuminated devices were encapsulated with SU-8 photoresist. The dark current density at -0.1 V and room temperature was measured to be 4.6 mA/cm² and was found to be dominated by diffusion currents. The devices with no anti reflection coating measured an external quantum efficiency of 73% at 300 K and 2.2 μ m. The EQE was also found to be independent of reverse bias indicating that the carrier diffusion length is much greater than the active layer thickness. The specific detectivity of 2.2×10^{10} Jones was measured at -0.1 V and room temperature.

Li et al.[99] investigated quantum efficiency loss and trap-assisted tunneling (TAT) current in MBE-grown In_{0.22}GaAsSb p - i - n photodiodes. Mesa sidewalls were passivated with a sodium sulfide solution and encapsulated with SiO₂. The photodiodes measured typical current densities between 3 and 4 mA/cm² at -0.05 V, and R₀A products between 4 and 13 Ω cm². Li noted an increase in dark current with the introduction of a p -type dopant in the active region, indicating that the dominant leakage mechanism is no longer generation-recombination. The leakage current was found to have an exponential dependence on voltage, which was believed to be caused by tunneling mechanisms, whereas in devices dominated by g-r currents one can expect a square root dependence on voltage. The authors applied a current model that separates diffusion, g-r, TAT, band-to band tunneling, and ohmic leakage to fit their measured data. The analysis showed that higher leakage currents in samples with higher donor concentrations in the active region were indeed caused by trap-assisted tunneling. Furthermore, electron and hole diffusion lengths of 4 and 0.2 μ m were extracted from QE modelling. However, these values are much lower than previous reports on electron and hole diffusion lengths in InGaAsSb photodiodes with similar In fractions, which are typically between 15-26 μ m and 10-12 μ m at room temperature, respectively[22], [69], [125], [131].

Barriode photodetectors

The barriode architecture employing InGaAsSb absorbers has become the most prominent photodetector type for this material system over the last decade. These detectors contain a layer of a wider bandgap material which serves as a potential barrier to majority carriers in the conduction band. The flow of minority carriers remains un-obstructed through a careful selection of a barrier material such that it does not create a valence band offset. In other words, the valence bands of the absorber and barrier layers are aligned, while the conduction band of the barrier prevents majority carrier flow. A typical band diagram of this structure taken from reference [22] is shown in figure 3.5.

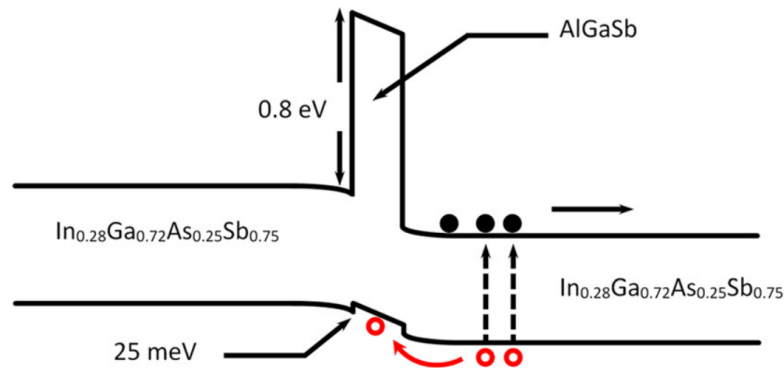


Figure 3.5: Band diagram of a barriode photodetector employing an InGaAsSb absorber taken from reference [22].

Craig et al.[22] were one of the first to report such a structure. The MBE-grown unpassivated In_{0.28}GaAsSb photodetectors employ an AlGaSb barrier which suppressed the dark current by preventing majority carrier flow in the conduction band, while maintaining a flow of photogenerated holes which remained un-obstructed by the very small 0.025 eV valence band offset. The photodetector leakage was found to be dominated by diffusion currents, which confirms that the SRH g-r and surface currents were successfully suppressed by the barrier design. Furthermore, the specific detectivity was found to be largely independent of reverse bias due to dark currents which were also found to be approximately

bias independent. Specific detectivity and EQE of $\sim 1 \times 10^{10}$ Jones and 30% were measured at $1.55 \mu\text{m}$, respectively.

A few years later, Li et al.[139] carried out a comparison between an MBE-grown nBn barrier photodetector and a *p-i-n* homojunction photodiode employing the same InGaAsSb material system with an In fraction of 28%. The dark current was successfully suppressed in the nBn device due to the employment of an AlGaSb barrier, leading to an increase in the R_0A product. The room temperature dark current density and R_0A product improved from 37 mA/cm^2 at -50 mV and $0.8 \Omega\text{cm}^2$ measured in the *p-i-n* device, to 13 mA/cm^2 at -200 mV and $3.6 \Omega\text{cm}^2$ measured in the nBn device. Once again it was shown that the nBn architecture successfully suppresses generation-recombination currents. The trade-off is a lower quantum efficiency of 32.3% in the nBn device, compared to the 57.7% in the *p-i-n* device at zero bias. Furthermore, similarly to what Craig[22] found, the small valence band offset between the absorber and barrier regions leads to a bias dependence of quantum efficiency, as some small applied voltage is needed for the holes to overcome the small residual potential barrier. Although the specific detectivities of both the *p-i-n* and nBn devices are largely the same at zero bias ($\sim 1.2 - 1.3 \times 10^{10}$ Jones), the nBn device measures a higher peak specific detectivity of 4.8×10^{10} Jones at -200 mV , compared to 3.0×10^{10} Jones measured in the *p-i-n* device, due to an increase in QE with applied bias.

Shortly after their original work was published, Li et al.[141] have successfully eliminated the bias dependency of quantum efficiency in $\text{In}_{0.28}\text{GaAsSb}$ barrier photodetectors by employing a novel pBn design which consisted of a highly *p*-doped top InGaAsSb contact. This structure can be seen as a *p-n* junction with a wide gap AlGaSb barrier placed between the two regions. Similarly to the nBn architecture, the large conduction band offset limits the flow of electrons from *p* to *n* side, while the depletion region is mostly shifted into the wide bandgap AlGaSb barrier which suppresses unwanted g-r, TAT, and band-to-band tunneling currents. The mesa sidewalls were further passivated with a sulphur treatment and encapsulated in a

thick SiO₂ film. The pBn device measured a room temperature dark current density at -50 mV and R₀A product of 1.2 mA/cm² and 22 Ωcm², respectively. The pBn devices measure a slightly improved peak specific detectivity of 2.0 × 10¹⁰ Jones at zero bias and room temperature.

Hanks et al.[140] reported on a similar InGaAsSb pBn photodetector design, but with a lower In fraction of 14%. The built-in field of the *p-n* junction enables zero-bias operation of these photodiodes at room temperature, with reduced leakage due to the AlGaSb barrier. What differentiates this design from the one reported by Li, is a top *p*-type GaSb contact layer in place of the *p*-InGaAsSb layer, which improves the ohmic contact. The photodiodes measured a room temperature R₀A product of 150 Ωcm², corresponding to a saturation current density of 0.175 mA/cm². With this detector design, a record-high value for specific detectivity of 9.7 × 10¹⁰ Jones was achieved at room temperature and zero bias (R_{peak} = 1.05 A/W).

The above values of specific detectivity and external quantum efficiency found in literature for InGaAsSb-based photodetectors are compiled in the graph in figure 3.6. Amongst the detectors with longer wavelength cut-offs ($\lambda > 2.4\mu\text{m}$; $x > 0.2$), the highest D* and EQE values of 2.2 × 10¹⁰ Jones and 73%, respectively, were measured in an In_{0.23}GaAsSb front-illuminated *p-n* photodiode with a 2.6 μm cut-off encapsulated with SU-8 photoresist[131].

3.4 Summary

Both GaSb and InGaAsSb are associated with certain growth and fabrication challenges. The high *p*-type background in GaSb, originating from Ga_{Sb} antisite defects, was found to be influenced by the V/III growth rate ratio and growth temperature. Despite some contradicting results, lower V/III growth rate ratios and temperatures generally lead to a reduced defect density and a lower unintentional doping concentration regardless of the growth technique employed, where doping concentrations in the low 10¹⁵ cm⁻³ region were achieved. GaSb-based devices also

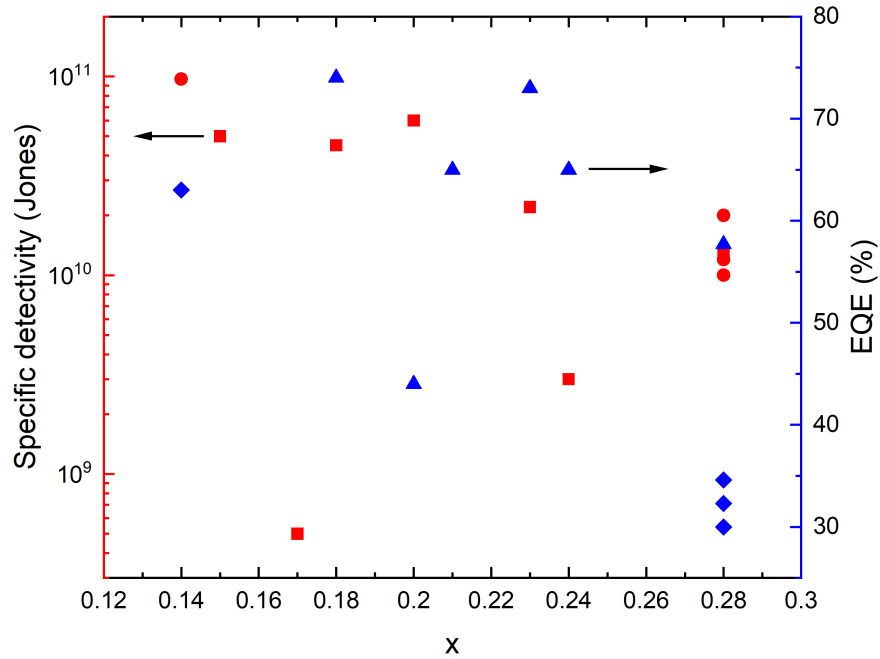


Figure 3.6: Summary of the specific detectivity and EQE values found in literature for InGaAsSb-based photodetectors. Red squares and blue triangles correspond to D^* and EQE values of homojunction p -(i)- n photodiodes, respectively. Red circles and blue diamonds correspond to D^* and EQE values of barrier nBn/pBn photodiodes, respectively.

suffer from surface leakage believed to be caused by surface oxidation, leading to the creation of elemental Sb which creates additional conduction paths on the surface. Despite the employment of various passivation techniques, GaSb-based devices continue to exhibit undesirable performance.

Growth of $In_xGa_{1-x}As_ySb_{1-y}$ alloys on the other hand is mostly hindered by the existence of a large miscibility gap which is of thermodynamical origin and restricts the usable bandgap range. Within this region, the InGaAsSb alloy has a tendency to decompose into a mixture of GaAs- and InSb-rich quaternary phases due to their large positive enthalpy of mixing. The exact boundaries of the miscibility region

are dependant on the specific growth technique and conditions employed. The best results are achieved with molecular beam epitaxy due to the lower growth temperatures attainable in this technique, which allows one to exploit surface kinetics and suppress the phase separation. Namely it was found that reducing the growth temperature below 500°C and controlling the V/III flux ratio reduces the adatom diffusion length and limits the extent of phase separation which becomes too slow to occur on the growth surface.

InGaAsSb-based photodetectors employing various structures have been investigated over the years. The most common photodetector structure that employs this material system is a homojunction $p-n$ or $p-i-n$ diode with In fractions between 13 and 30%. Current densities as low as $\sim 2 \text{ mA/cm}^2$ at -100 mV and R_0A products as high as $\sim 60 \text{ }\Omega\text{cm}^2$ have been achieved in unpassivated devices. The performance of these photodiodes was limited by surface leakage, which was in many cases successfully reduced with the employment of a passivating window layer or other types of chemical passivation. The passivated photodiodes achieved dark current densities as low as $\sim 30 \text{ }\mu\text{A/cm}^2$ at -10 mV and R_0A products as high as $260 \text{ }\Omega\text{cm}^2$. Both unpassivated and passivated photodiodes with no anti-reflection coating measure high external quantum efficiencies of up to an impressive 74%. Typical specific detectivity values are in the range between 3×10^9 and 5×10^{10} Jones, with one of the highest values of 6×10^{10} Jones measured in an unpassivated back-illuminated InGaAsSb $p-n$ photodiode with 20% In.

The best photodiode performance was achieved with a barriode structure which successfully suppresses the dark current, and has become the most prominent photodetector type for this material system. Such structures were found to be diffusion limited which suggests that both bulk generation-recombination and surface currents were successfully minimised. The highest specific detectivity of 9.7×10^{10} Jones was achieved in an $\text{In}_{0.14}\text{GaAsSb}$ pBn photodiode at zero bias and room temperature. This novel structure exploits both the barriode design as well as the built-in electric field to reduce unwanted leakage while enabling zero-bias

operation.

Despite the many improvements achieved over the years with InGaAsSb-based photodetectors, surface leakage remains an issue in many structures, and the need for the development of appropriate passivation techniques is highlighted. Moreover, very little attention has been given to dilute alloys whose full potential is yet to be explored. Additionally, no existing study to date investigates the detector performance across the full alloy range.

Chapter 4

Experimental Methods

In order to perform a comprehensive study of the InGaAsSb alloy, a wide range of samples had to first be prepared. The following chapter outlines epitaxial growth procedures performed with molecular beam epitaxy presented in section 4.1, as well as device fabrication techniques including photolithography, contact deposition, wet chemical etching, and passivation, presented in section 4.3. Finally, various characterisation methods are summarised in section 4.4 including FTIR spectroscopy, current-voltage, capacitance-voltage, and spectral responsivity measurements.

4.1 Sample growth

All of the samples discussed in this work have been grown via solid source molecular beam epitaxy (MBE). Two main types of structures illustrated in figures 4.1a and 4.1b have been grown; In_xGaAsSb *p-i-n* photodiodes on *n*-GaSb substrates and In_xGaAsSb single layers on undoped GaAs substrates, respectively. These structures will be discussed in more detail in chapter 5.

This epitaxy technique relies on the evaporation of constituent elements from their solid state onto a substrate in a vacuum system. MBE is advantageous to other growth techniques such as LPE, OMVPE, and CVD (chemical vapour deposition)

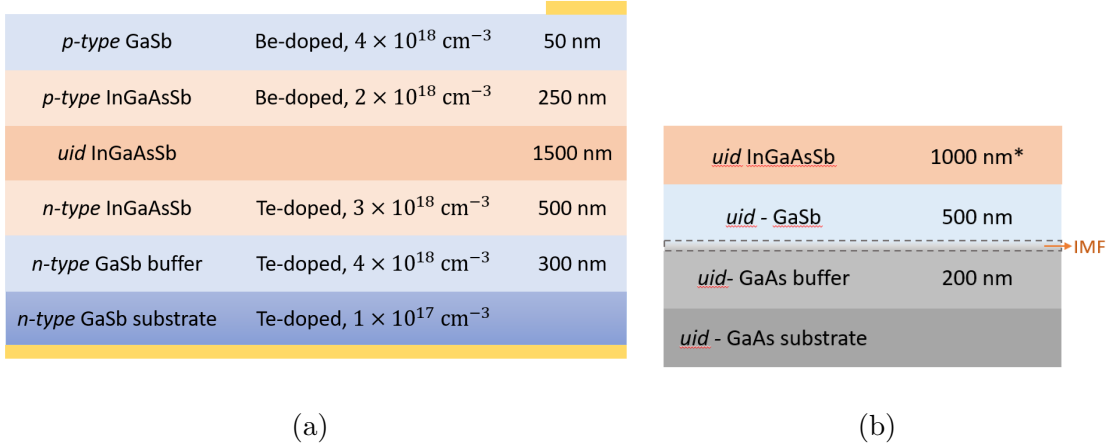


Figure 4.1: (a) In_xGaAsSb *p-i-n* photodiode structure grown on *n*-type GaSb substrates with various In fractions to enable the comparison of InGaAsSb detector properties with varying alloy composition. (b) InGaAsSb transmission sample structure grown on semi-insulating GaAs substrates with the aim of obtaining extended absorption coefficient data. *This layer thickness is 4500 nm for the GaSb transmission sample.

due to its ability to reproducibly grow structures with dimensions on the atomic monolayer scale with fewer thermodynamical defects due to the relatively low growth temperatures, as well as the ability to monitor the growth process in situ and in real time[144], [145]. MBE is a versatile technique that can be used to grow a range of diverse materials and structures with precise compositions and doping profiles.

The samples were grown with a Veeco GenXplor reactor equipped with arsenic and antimony cracker cells. A simplified schematic of the reactor is illustrated in figure 4.2. The reactor consist of: (i) a growth chamber that is held under ultra high vacuum (UHV, 10^{-9} - 10^{-11} Torr) to avoid unintentional contamination of the epitaxial layer with impurities during growth, (ii) temperature controlled cylindrical cells that contain ultra-pure crucibles with high purity source elements (6-7 N) that evaporate onto the substrate, (iii) mechanical cell shutters that switch the evaporated molecular beams on/off (iv), a substrate holder and heater system that rotates around the axis perpendicular to the cell flange, and (v) a load lock

system which allows the wafers to be loaded and unloaded into the growth chamber without disrupting the UHV environment.

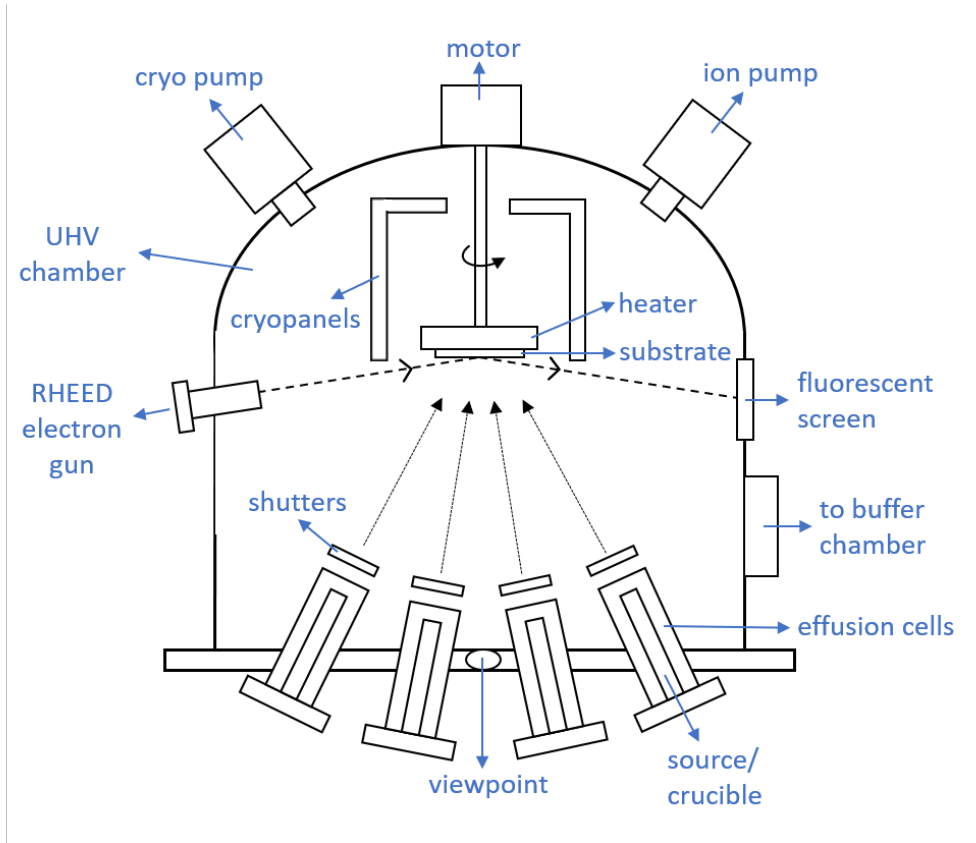


Figure 4.2: Schematic of an MBE growth chamber showing thermal effusion cells with cell shutters, substrate holder/heater assembly, RHEED system, cryopanel, and pumps.

The load lock system consists of two additional chambers - the load lock chamber, and the buffer (prep) chamber. All of the chambers are separated from one another by mechanically operated air-tight gate valves. Prior to growth the substrate undergoes three thermal cleaning stages. The substrate wafer is first loaded into the load lock chamber. A two pump system consisting of a scroll pump and a turbo pump is used to bring the base pressure down to $\sim 10^{-6}$ before the first bake-out cycle is initiated. At this stage, the wafer (including the wafer holder and the cassette) is outgassed at 200°C to ensure the removal of the absorbed gases

introduced from the environment. Once the pressure in the load lock chamber has become sufficiently low ($\sim 10^{-7}$), the wafer is transferred into the buffer chamber which is kept at a base pressure of $10^{-7} - 10^{-8}$ by an ion pump. A second bake-out ensues as the wafer is heated up to the appropriate outgas temperature (for a GaSb substrate this is typically $350 - 400^\circ\text{C}$). Finally, once the pressure in the buffer chamber has become sufficiently low ($\sim 10^{-8}$) and the sample has been outgassed, the wafer is moved to the growth chamber by a mechanically operated transfer arm. The final stage in substrate preparation prior to growth is the substrate deox which takes place in the growth chamber. Here, the substrate is heated until the layer of oxides formed on the surface is desorbed and a clean surface is revealed.

During epitaxial growth the substrate is held at the appropriate growth temperature by the substrate heater, and is continuously rotated to enable even distribution of the constituent elements that impinge upon its surface from the source cells. The substrate is not in contact with the heater, but is rather radiatively heated by it, thus a calibration of the actual substrate temperature compared to the one measured by a thermocouple placed on a pseudosubstrate on the opposite side of a heater is required. This is achieved by observing the onset of oxide desorption and the transition of the GaSb surface reconstruction pattern from 2×5 to 1×3 under constant Sb_2 flux via RHEED. Both of these occur at a known temperature, hence a calibration plot that relates the measured and real temperatures can be created. The RHEED monitoring technique as well as the reconstruction patterns will be discussed in more detail later in this section. The growth rate, which is precisely controlled by the cell temperatures and valve positions, can be kept sufficiently low to allow for compositional changes on the scale of the lattice constant[62]. The UHV conditions and low growth rates enable the use of mechanical shutters placed in front of the source cells to switch the molecular beams on/off. This makes MBE the best technique for growing complex heterostructures with layers as thin as a few nanometers with abrupt interfaces and precise doping profiles which can be either abrupt or graded continuously[56]. The UHV environment is maintained by

an ion pump and a helium cooled cryogenic pump which enables condensation and subsequent removal of gasses from the growth chamber. The background pressure in the chamber is monitored with an ion gauge. Additionally, several cryopanel cooled with liquid nitrogen are placed around the substrate holder and the cells in order to remove condensable contaminants from the growth environment and thermally insulate the cells from one another[144].

Group III elements, such as gallium (Ga) and indium (In), are contained within thermal effusion (evaporation) cells inside high-purity crucibles and their evaporation rate (and by extension, growth rate) is controlled by the temperature of the cells. The crucibles are radiatively heated by Ta wires to a desired temperature, and are surrounded by radiation shields which provide thermal insulation from the environment and adjacent cells. The dopants are similarly contained within effusion cells and the concentration of each dopant that is incorporated into the lattice is controlled by the cell temperature which is pre-calibrated through Hall measurements. Group V elements such as arsenic (As_4) and antimony (Sb_4), are contained within valved cracker cells. In this case, the source material is contained within a heated crucible which is separated from an additional cracking region by a valve that controls the flux. In the cracking region, tetramers of arsenic and antimony are partially converted into dimers and monomers by interactions with surfaces heated up to close to 1000 degrees Celsius. This is because, unlike group III elements which are atomic sources, group V elements are molecular sources, i.e tetramers. It was found that cracking As_4 and Sb_4 increases their surface incorporation rates and reduces the number of defects in MBE-grown GaAs and GaSb layers[146], [147]. Unlike with the the effusion cells, the beam flux is controlled primarily by the valve position. The layer thickness is controlled by the rapid mechanical shutters located in front of each cell. Closing the shutters blocks the molecular beams and immediately stops the growth.

A beam flux monitor consisting of an ion gauge attached to a retractable arm is used to measure the beam equivalent pressure (BEP) of individual molecular beams.

However, to get an accurate measure of the incorporation of individual elements into the crystal lattice, i.e. to obtain growth rates, it is necessary to use RHEED (Reflection High Energy Electron Diffraction). The RHEED system consists of an electron gun which emits a collimated beam of electrons at a very shallow angle with respect to the growing surface, and a fluorescent screen on the opposite side of the chamber that reacts with the diffracted electrons. RHEED enables in situ monitoring of the surface reconstruction, which in turn enables: (i) the measurement of growth rates by studying the RHEED intensity oscillations, (ii) monitoring of the substrate deox prior to growth, and (iii) the study of growing layer quality in real time. RHEED oscillations occur as a result of the periodic change of surface morphology during the deposition of a monolayer. Hence one period of intensity oscillation is equal to the time it takes for a single monolayer to form[144]. The growth rate of each constituent element for a particular cell temperature and/or valve opening has been calibrated prior to growth using RHEED. This approach also takes into account the sticking coefficient of different elements, which plays an important role in the growth of III-V compound semiconductors. For group III elements such as indium and gallium, almost every atom that hits the surface of the substrate is incorporated into the crystal lattice, hence they have a sticking coefficient of close to unity. However, group V elements such as arsenic and antimony have a sticking coefficient of less than unity, implying that only a fraction of incident atoms will be incorporated into the lattice. Therefore, it is not sufficient to look at the BEP ratio of incident beams alone to establish a particular compositional relationship between constituent elements.

Another usefulness of RHEED is in the real time in situ study of the surface reconstruction pattern. Surface reconstruction refers to the re-ordering of the outermost atomic layer(s) of a crystal to reduce the energy of the free surface[145]. This is the principle under which epitaxial growth takes place in MBE. Because the angle of incidence of the electron beam is extremely shallow, the electrons penetrate only the first few monolayers of the surface.

If the atomic surface is smooth, the electrons will "see" a 2D surface where only the topmost layer of adatoms forms a 3D structure leading to a coherent diffraction pattern that forms streaks. However, if the surface is rough, the electrons will "see" a 3D surface bigger than just the outer monolayer which leads to a less coherent diffraction pattern that forms spots rather than streaks. If the surface is completely rough and disordered as is the case with surfaces covered in oxides, the diffraction is incoherent and no pattern is visible. In the case of the atomically smooth, two-dimensional surface, the reconstruction pattern stems from the re-ordering and incorporation of the topmost layer of adatoms into the crystal. The exact reconstruction pattern can vary depending on growth conditions and is associated with different surface stoichiometries. For example, when growing GaAs under As rich conditions, a 2×4 reconstruction occurs, whereas in Ga rich conditions, a 4×2 reconstruction occurs[144]. This means that, depending on the crystal orientation, either a $2 \times$ ("two by") or $4 \times$ ("four by") will be visible on RHEED. A $2 \times$ is characterised by one dimmer secondary streak between two brighter primary streaks, and a $4 \times$ is characterised by 3 dimmer secondary streaks between two brighter primary streaks. GaSb is characterised by a 1×3 reconstruction pattern. An example of the surface reconstruction pattern as seen via RHEED is shown in figure 4.3. Hence surface reconstruction can be used as an extremely useful system-independent monitor of the growth conditions[145].

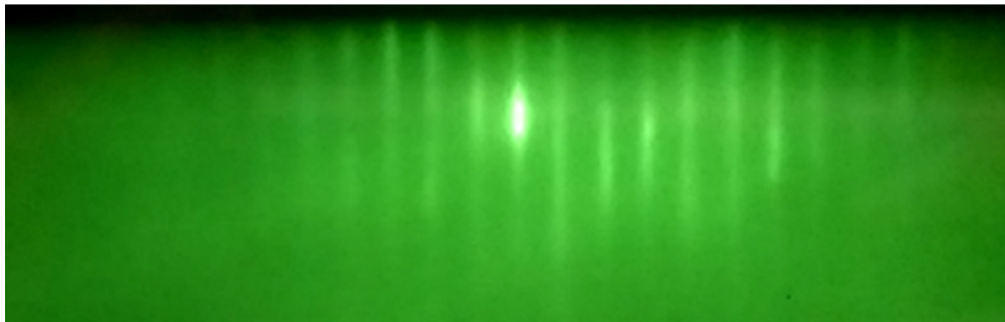


Figure 4.3: Image of the RHEED screen showing a $3 \times$ surface reconstruction during GaSb buffer growth, taken from reference [70].

4.2 X-ray diffraction

X-ray diffraction is a crucial step in sample growth and analysis. In complex, multilayer structures, each layer has to be lattice matched to the previous one, which usually implies all layers are grown lattice-matched to the substrate. An epilayer is considered to be lattice-matched when its lattice constant is equal to the lattice constant of the preceding layer, as illustrated in figure 4.4a.

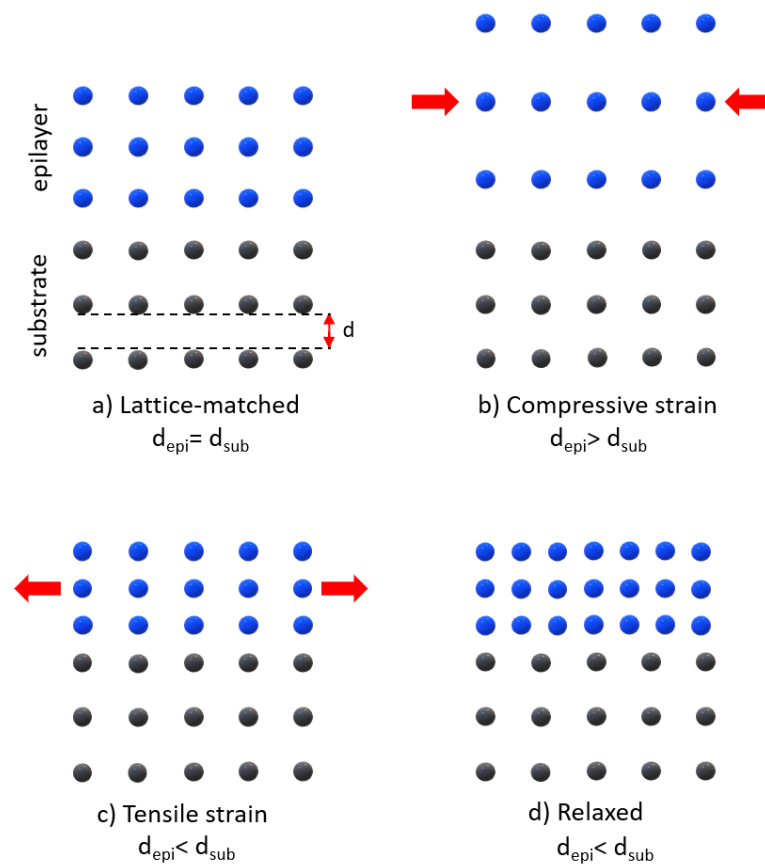


Figure 4.4: Simplified representation of lattice-matched and strained epitaxial layers.

For a small difference in lattice constants, the mismatched layer can grow strained up to a certain thickness known as the critical thickness, i.e. it conforms to the lattice constant of the preceding layer. This critical thickness depends on the material in question and the degree of mismatch/strain present, and can be calculated according to a model given by Matthews and Blakeslee[148]. However, it was found

experimentally that this model often underestimates the critical thickness, hence it is only useful in providing a rough indication of where this limit may be for a given composition. For example, a layer of $\text{In}_{0.05}\text{GaAs}_{0.06}\text{Sb}$ with a 270 arcsecond mismatch can only be grown 660 nm thick before the onset of relaxation according to Matthews and Blakeslee. If the critical thickness is exceeded, the layer will relax either fully or partially into its native lattice constant to relieve the built-up strain. This relaxation is accompanied by defect formation at the interface, which can often propagate into the electrically active layers (such as threading dislocations), thus compromising material quality and device performance. If the lattice constant of the epilayer is greater than that of the substrate, the epilayer will grow compressively strained. Similarly, growing epilayers with a smaller lattice constant than the substrate, results in tensile strain. Different types of strain are illustrated in figure 4.4b-d. To ensure well lattice-matched epitaxial layers, XRD measurements are used to ascertain the lattice constants of individual layers, and the structures are re-grown if needed.

In this technique, a collimated beam of monochromatic x-rays is incident upon a sample and diffracted by the crystal planes to produce a diffraction pattern. Every material has a characteristic diffraction pattern which can be used to identify it and study its geometry. The measurements were performed with a Bruker D8 Discover diffractometer. In this system, a heated tungsten filament emits electrons which are accelerated in a shielded x-ray tube and directed towards a metal anode. Upon impact with the anode, the incident electrons interact with the electrons of the metal and emit x-rays in the process. The wavelength of the x-rays is dependant on the type of metal used for the anode [149]. A copper anode is used in this experiment with an X-ray wavelength of 1.54 \AA . The x-rays are then conditioned to ensure they are collimated and monochromatic, before being incident upon the sample and reflected by the highly ordered atoms of the crystalline material. X-ray diffraction is a result of elastic scattering of the incident electrons, a process in which the incident radiation excites the electrons of the crystal lattice which then release this energy

in the form of secondary x-rays with the same wavelengths as the incident x-rays. When the secondary x-rays are in phase with one another, constructive interference occurs. This will take place when the following condition is satisfied:

$$n\lambda = 2d\sin\theta_B \quad (4.1)$$

where n is an integer order of reflection, λ is the wavelength of the X-rays, d is the spacing between the atomic planes in the growth direction, and θ_B is the Bragg angle at which constructive interference occurs. The diffracted x-rays will interfere constructively only at specific angles due to the regular atomic spacing of the crystal lattice. X-rays penetrate deeply into the material making it a bulk measurement technique which allows us to determine the lattice constants of all of the different layers in the material. During the measurement, a coupled $\omega-2\theta$ scan is used, where ω is the angle between the source and the sample, and 2θ is the angle between the source and the detector, as illustrated in figure 4.5.

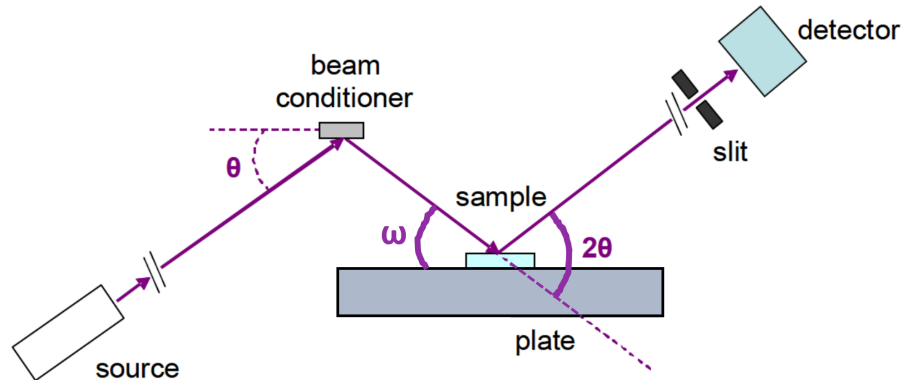


Figure 4.5: Schematic of the X-ray diffraction apparatus.

In this configuration, the x-ray source is stationary, while the sample and the detector rotate around the same axis. During a scan, the detector moves at twice the rotational speed of the sample to ensure it is correctly positioned at the site of diffraction such that $\omega = \theta$. The intensity of the reflected x-rays will reach a maximum at $\theta = \theta_B$. If the epilayer(s) is lattice-matched to the substrate, then

the structure will have a singular lattice constant, d , and the XRD scan will show only one intensity peak whose location will be dependent on the substrate used. If multiple peaks are visible, the epilayer(s) is mismatched, i.e. its lattice constant is different than the lattice constant of the substrate. According to equation 4.1, if the epilayer peak is located at an angle greater than the substrate peak, then its lattice constant is smaller than the lattice constant of the substrate, and vice versa. Figure 4.4 shows this tetragonal distortion in strained layers where the spacing between the layers in the growth direction is affected (either increased or decreased) due to the epilayers conforming to the lattice constant of the substrate. It is this layer spacing in the growth direction that is measured through XRD. In order to confirm the composition and thickness of individual layers, a Bede RADS software is used to model the expected structure. The changes are then made to the input parameters of the modelled structure (layer thicknesses, composition, and relaxation) until it closely matches the measured XRD spectra. Figure 4.6 shows an example of a simple XRD scan with the simulated spectrum overlaying the measured one.

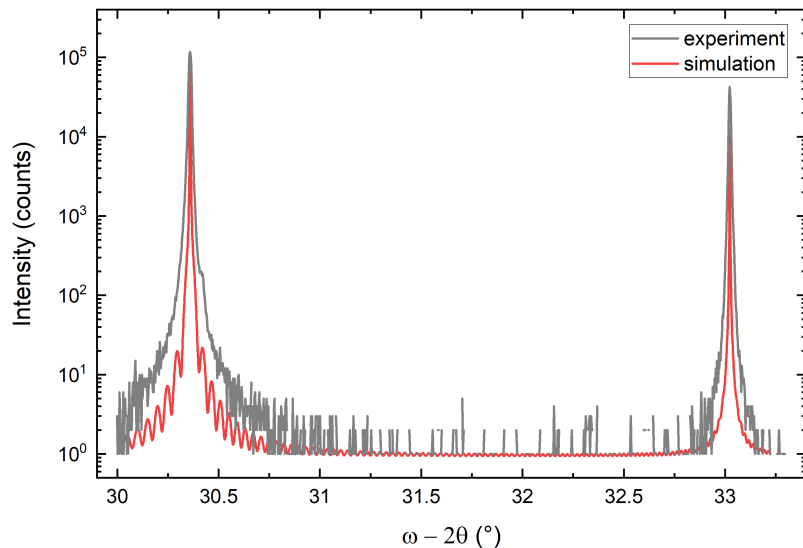


Figure 4.6: An example XRD scan of a thick GaSb layer epitaxially grown on a GaAs substrate. Red line shows the spectrum simulated via the Bede RADS software.

The sample consists of a 5 μm thick GaSb layer epitaxially grown on a GaAs substrate. Due to the relatively large difference in the lattice constants of the two materials (7.5%), the GaSb layer grew relaxed (with the aid of an interfacial misfit array which will be discussed in more detail in chapter 5). From the location of the GaSb peak it can be determined that this layer grew 99.84% relaxed. Evidently the layer spacing in the growth direction of the epitaxial GaSb is still marginally bigger than the native lattice constant of GaSb due to this layer not growing 100% relaxed, but with a negligible amount of residual strain.

4.3 Fabrication

The next step in sample preparation is device fabrication. It is at this stage that epitaxially grown bulk *p-i-n* structures are transformed into photodetector devices that can be electrically characterised. All samples in this work have been processed in Lancaster University's Quantum Technology Centre cleanroom. Each sample is subject to the same fabrication process consisting of multiple steps, from cleaning to chemical etching and contact deposition. During the fabrication, the highest temperature the samples were exposed to was 180°C during a soft bake - well below the Sb desorption temperature of 400°C at UHV. This temperature is even higher at atmospheric pressure. Another consideration is diffusion of gold contacts into GaSb when annealing at temperatures in excess of 250°C, which occurs even when an intermediate layer of Ti is employed. However, this temperature was never approached during fabrication. The samples were not exposed to plasma at any point, hence the effect it might have on InGaAsSb is not known. For the purposes of this project, it is important to maintain consistency between samples during fabrication and to minimise any variation in processing steps that might impact device properties and induce changes between different samples that are not representative of the material properties. The individual fabrication steps will be described in detail in the following section.

4.3.1 Sample cleaning

The first step in device fabrication is wafer cleaning to rid the surface of any contaminants and debris. This is achieved by soaking and rinsing of the samples in three solvents. Firstly, a sample is placed in a beaker of acetone and left to soak for several minutes. It is then transferred to a beaker of isopropyl alcohol (IPA) to remove any stains or residues from the heavier solvent. The sample is then rinsed in de-ionised water and dried with a high pressure nitrogen gun. Finally, the sample is baked at 100°C for 1 minute on a conduction hot plate to thermally remove any water residue or remaining contaminants. Parts of this process are repeated at various stages of fabrication to ensure samples remain clean between different processing steps.

4.3.2 Photolithography

Photolithography is used to define patterns on the surface of the sample prior to contact deposition, chemical etching, and passivation. In this technique, the sample is first covered with a layer of polymer-based photosensitive resist, and a mask with chosen features is used to cover or expose certain areas of the surface before it is exposed to ultraviolet (UV) radiation. The UV light either breaks down a positive resist or hardens a negative resist. The sample is then soaked in a developer to remove the broken down (or not hardened) resist, revealing a pattern on the surface. The exposed parts of the surface can now either be etched or subject to deposition. Figure 4.7 shows the fabrication process involving multiple photolithography steps carried out in this work.

Resist deposition

Once the sample has been thoroughly cleaned by following the steps described in section 4.3.1, a bi-layer of resist is deposited to enable the deposition of the top contact. The sample is loaded onto a chuck inside a SUSS MicroTec LabSpin spinner, and a vacuum is activated to ensure the sample is fixed in place. A pipette is then used to deposit a layer of LOR 3A[150] resist on the surface of the sample. LOR 3A

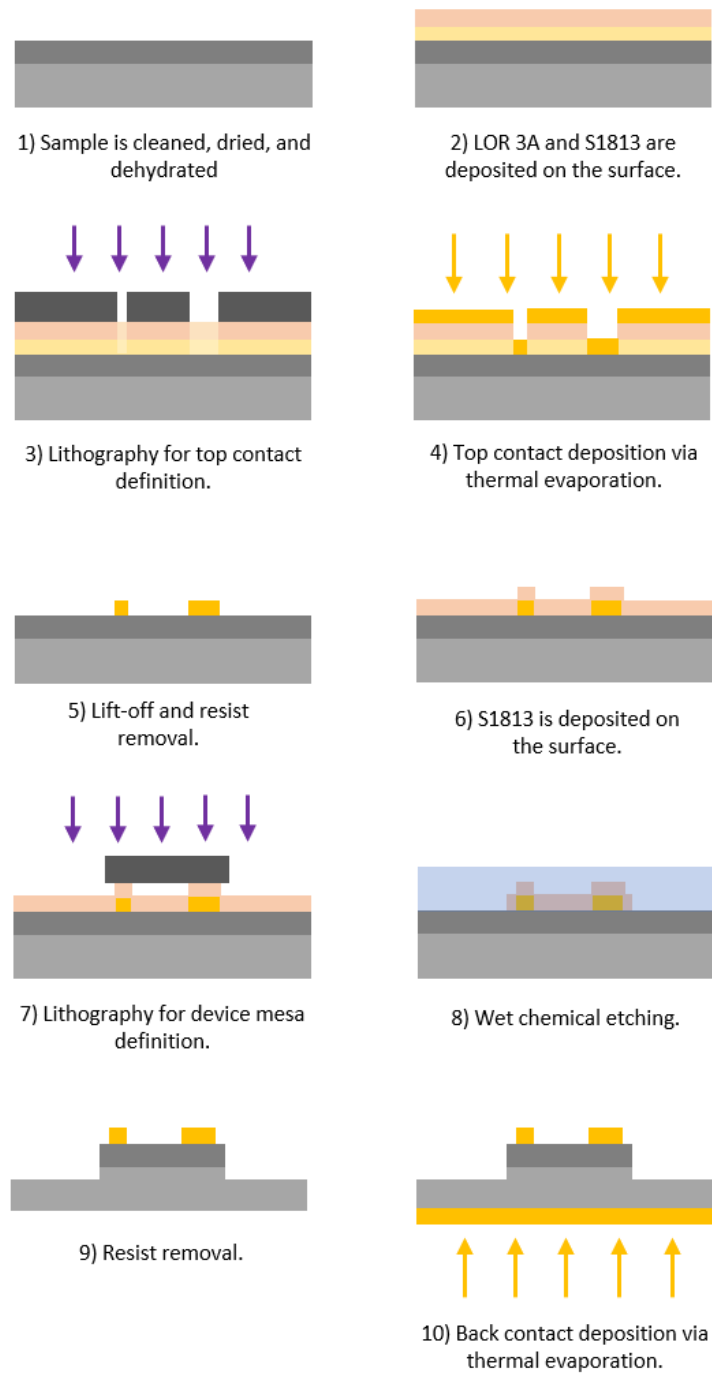


Figure 4.7: Processing flow for $p-i-n$ photodiodes showing several lithography steps, contact deposition, and wet chemical etching.

is not photosensitive, i.e. it does not react to UV radiation. The spin acceleration, speed and time are varied to achieve the desired resist thickness. In this case, the

desired primary film thickness is ~ 300 nm which was achieved by spinning the sample at 3000 rpm for 45 seconds. The sample is then soft-baked at 180 °C for 5 minutes on a conduction hot plate to dry the LOR 3A film and remove any remaining solvent before the second layer of resist can be applied. Post bake, the sample is loaded back into the spinner, and a positive photoresist microposit S1813[151] is applied with a pipette. After spinning the sample at 3000 rpm for 30 seconds which results in a secondary resist thickness of ~ 2000 nm, the sample is baked at 115 °C for 2 minutes. The sample is now ready for exposure.

Exposure and chemical treatment

The selective exposure to UV light was achieved with a SUSS MicroTec MJB4 mask aligner and a purpose-build mask. This system allows a top-side alignment accuracy of < 0.5 μm [152]. The mask is a 4" x 4" glass plate with a UV-resistant patterned chrome film on one side. Each mask contains several different patterns which correspond to various stages of device fabrication. The sample is first loaded onto a stage and a mask with the desired pattern is firmly fixed above it with the aid of a vacuum. The height of the stage, as well as its x , y , and θ positions are manually controlled to enable the precise alignment of the sample with the desired mask pattern. A microscope fixed above the mask with a direct perpendicular view of the mask surface and the sample below it is used to aid the alignment process. The first step in the alignment procedure is the semi-automated wedge error compensation which ensures the sample surface is parallel to the mask and determines the correct distance between the two for exposure. After creating a small (< 50 μm) gap between the sample and the mask, the user then manually carries out the x , y , and θ corrections with the aid of the alignment features integrated within the mask. Once the sample is aligned perfectly with the desired pattern on the mask, the gap is eliminated and a soft contact is once again created between the two, where the mechanical pressure keeps the mask and the sample aligned. In this mode, a resolution of 2 μm can be achieved[152], which is sufficient for the feature sizes used in this work. The sample is then exposed to UV light from a mercury

lamp source, with a wavelength of 365 nm (I-line of mercury spectrum). Only the clear parts of the mask will transmit the light, and hence the chosen pattern will be imprinted on the surface. The exposure length depends on the resist type and thickness, and was varied between 1.8 - 2.6 seconds to achieve the correct feature definition. The selective exposure to UV light breaks down the chemical bonds in the positive photoresist, which is then easily removed by chemical treatment with a suitable developer. In this case, the sample was soaked in MF-CD-26[153] for 60-90 seconds to remove the broken down resist and reveal the desired pattern on the surface. MF-CD-26 contains tetramethyl ammonium hydroxide (TMAH) which is a substance known to etch GaSb[154]. However, due to the short development times and the very slow etch rate of GaSb in MF-CD-26, the exposed parts of the surface were unaffected. LOR 3A develops at a faster rate than S1813 which creates an undercut profile and ensures a discontinuous film deposition. This enable a smooth contact lift-off by creating a break in the evaporated metal, as illustrated in figure 4.8. The sample is finally rinsed in deionised water for ~ 10 seconds to neutralise the developer, and dried with the high pressure nitrogen gun.

4.3.3 Contact deposition

Once the appropriate pattern has been defined on the surface, the sample is ready for top contact deposition. Deposition of contacts (semiconductor to metal interfaces) is necessary to enable the creation of an electrical circuit between the semiconductor device and the external electronics. The contacts should be Ohmic, i.e non-rectifying with linear I-V characteristics. The resistance of the contacts should be negligible to minimise any voltage drop across them. Typically a two-layer contact system is employed, in this case titanium and gold (Ti/Au). Titanium has a dual purpose: (i) it serves as a barrier to prevent gold from diffusing into the semiconductor where it can act as a dopant, and (ii) it aids the adhesion of gold. Gold is the preferred choice for the upper contact layer since it's inert, does not oxidise, and is relatively easy to bond to.

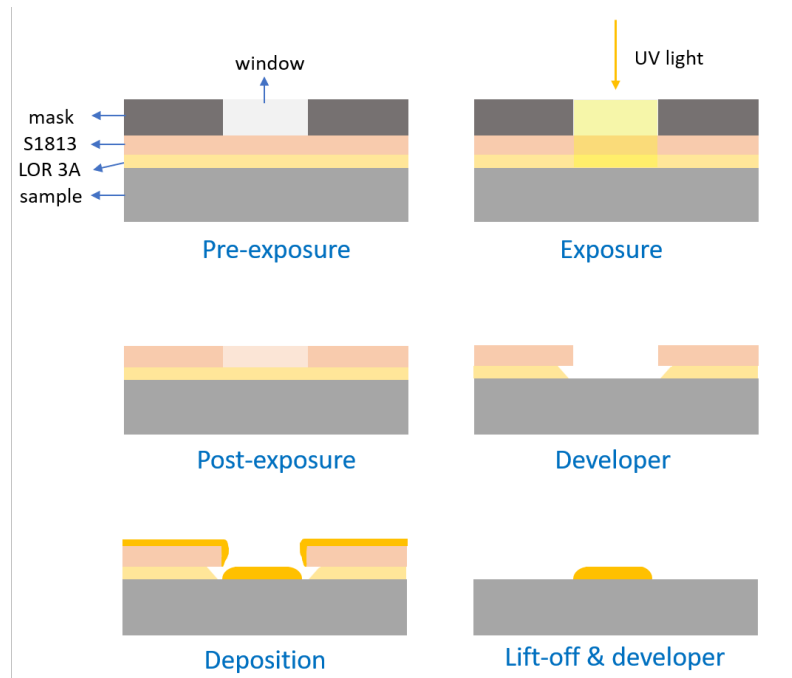


Figure 4.8: Deposition of a resist bi-layer enables a clean lift-off by creating a break in the deposited contact.

Thermal evaporation

The deposition of contacts is achieved via thermal evaporation with a Moorfield Minilab 060 reactor equipped with a turbomolecular pumping system. The source materials are contained within baskets located at the bottom of the chamber. The baskets are made up of various highly resistive materials which heat up when a current is passed through them. The titanium basket is a coil of tungsten wire, while the gold basket is additionally coated in alumina. The baskets are cleaned prior to first use to remove any contaminants. This is achieved by firstly soaking them in acetone and IPA, followed by heating them up to typical operational temperatures by passing the equivalent current through them while empty. Likewise, the source materials are first cleaned in acetone and IPA, and then rinsed in deionised water and dried with the nitrogen gun before being loaded into the baskets. The samples are fixed to a plate with DuPont's chemically and thermally resistant Kapton tape[155], which is placed above the baskets with the samples facing down. A shutter located

between the plate and the baskets prevents unwanted deposition of impurities before starting the evaporation. The shutter is also used to control the thickness of the metal contacts. It is important to remove any excess resist from the exposed parts of the surface of the samples prior to evaporation, since resist is known to impede the adhesion of contacts and compromise their quality.

Once the samples have been loaded, the door is closed and the turbo pump activated. The base pressure is lowered to $\sim 10^{-6}$ mBar before evaporation can start, to prevent the contamination of contacts with impurities. Once the desired pressure has been reached, a current passing through the Ti basket is slowly increased until a pressure drop is recorded in the chamber. This marks the start of the titanium sublimation which typically happens at currents between 55 and 65 A. This pressure drop is caused by the high reactivity of titanium, which coats the chamber walls and subsequently captures impurities. Once the pressure drop has been noted, the current is allowed to stabilise before the shutter can be opened and deposition started. The evaporation rate is monitored with a QPod software which uses sensor data and a set of input parameters to calculate the thickness of the deposited metal. The sensor is made up of a quartz crystal connected to an AC source, whose frequency of oscillation changes depending on the amount of material deposited onto it. The input parameters required to correctly measure the growth rate are material density, Z-ratio, and tooling. Z-ratio accounts for the change in frequency depending on the mass being deposited. The tooling factor accounts for the difference in the thickness of the material deposited on the sample compared to the sensor, and is mostly dependent on the distance between the two. The growth rate is kept around $\sim 2 \text{ \AA/s}$ for titanium, and $\sim 5 \text{ \AA/s}$ for gold. Once the desired thickness has been reached (20 nm of Ti, 200 nm of Au), the shutter is closed and the deposition abruptly discontinued.

The evaporation of gold ensues directly after titanium without removing the samples from the chamber between evaporations, since titanium immediately and irreversibly oxidises when exposed to air. The gold layer needs to be sufficiently thick (but not so

thick that the total contact thickness exceeds that of the LOR 3A film) to withstand any subsequent probing and/or bonding. Gold evaporates when the current in the basket has been increased to 26-32 A. Unlike with titanium, there is no observed pressure drop in the chamber, and previous evaporations are used as a reference to confidently select the right current that gives the desired evaporation rate before opening the shutter. Care must be taken to keep the evaporation rate sufficiently high to minimise the length of time samples are confined to the chamber as the temperature in the chamber rises continuously due to heat from the baskets. As both the plate and the samples heat up, there is a risk of baking the resist which might compromise the lift-off process. A thermocouple located above the samples is used to monitor the temperature in the chamber.

Lift-off

Upon completing the evaporation of contacts, the samples are soaked in acetone for several minutes to dissolve the S1813. Once gold flakes can be seen detaching from the surface, a pipette is used to agitate the solution and aid the removal of gold. Care must be taken to keep the samples submerged in acetone at all times until all unwanted gold has been completely removed, to avoid the gold flakes being permanently bound to the surface by van der Waals forces.

If acetone alone does not remove gold from the surface, samples can be treated with a Shipley 1165 remover, without allowing the samples to dry during relocation. For particularly stubborn samples, the remover can be heated up to $\sim 60^{\circ}\text{C}$ and further agitated with a pipette. A mild ultrasonic bath can further aid the removal of excess gold if needed. If only acetone has been used to complete lift-off, the samples need to be additionally soaked in MF-CD-26 developer anywhere between 30 seconds and several minutes to remove the LOR 3A. Once all resist has been removed, the developer is neutralised with deionised water and the samples dried with the nitrogen gun. Microscopic imaging should reveal horseshoe-shaped circular contacts of various sizes on the surface of the sample.

Once lift-off has been successfully completed and the samples cleaned, photolithog-

raphy is once again used to define the device mesas in preparation for wet chemical etching. The same steps described in section 4.3.2 are followed, with one difference - only a layer of the S1813 photoresist is applied.

4.3.4 Wet chemical etching

Wet chemical etching is used to electrically isolate the devices, i.e. to chemically remove unwanted material. In order to selectively etch the material between (what are to become) individual device mesas, the samples are first patterned with resist by following the steps described in section 4.3.2. As mentioned before, only S1813 is needed to protect the parts of the sample we do not want etched (resist does not react to chemical etchants).

A citric acid ($C_6H_8O_7$) and hydrogen peroxide (H_2O_2) solution was used with a 2:1 ratio to etch the samples. Citric acid granules are first mixed with deionised water in a 1:1 ratio (typically 30 g of citric and 30 ml of DI water). The mixture is then stirred until all of the granules have completely dissolved and the remaining solution is clear. 15 ml of hydrogen peroxide is then added to the mixture which is stirred for several more minutes to ensure a uniform solution. The samples should have been subject to the second round of lithography at this stage and have the correct pattern defined on the surface with the resist covering the parts of the surface that are NOT to be etched - in this case we want circular device mesas with the horseshoe contacts on top. The prepped samples are submerged in the etchant for the appropriate length of time. Hydrogen peroxide reacts with the exposed surface and creates oxides of the constituent elements. The citric acid then strips this layer of oxides from the surface, and the cycle repeats until it is stopped by removing the sample from the solution.

To electrically isolate the devices the etch depth needs to exceed 1800 nm (into the n -InGaAsSb layer). Since GaSb and InGaAsSb layers have a relatively slow etch rate in citric acid (between 2 and 6 nm/min), the samples were left in the etching solution overnight (~ 12 hr) to ensure a depth greater than 2600 nm (thickness of

the entire epilayer stack) is reached regardless of the exact quaternary composition, i.e. all of the samples were etched several hundred nanometers into the substrate. Once etching has been complete, the samples are thoroughly rinsed in DI water to quench the etchant and remove any residue from the surface. Finally, the samples are dried with the nitrogen gun and the surface profiled. A KLA-Tencor Alpha-Step IQ surface profiler was used before and after the etch to check the etch depth and surface quality. If the desired etch depth has been reached, the remaining resist can be removed from the device mesas with a brief (~ 5 min) acetone bath.

If no passivation is to be applied to the surface, a common contact is deposited at this stage to allow electrical characterisation. All samples in this work employ a Ti/Au (20/200 nm) back contact which is deposited via thermal evaporation post etch on the back surface of the samples by following the steps described in section 4.3.3. To protect the surface of the samples, Kapton tape is first placed on the evaporator plate before the samples are fixed to it. Lithography and lift-off are not necessary in this case, since we want the entirety of the back surface to serve as the common contact.

If encapsulation of the surface is needed to prevent oxidisation, passivation ensues immediately after the etch has been completed to minimise the length of time the surface is exposed to air and subject to oxidation.

4.3.5 Passivation

Surface oxidation as a result of exposure to air is a known cause of unwanted surface currents in many materials and structures. Hence a passivating layer is often deposited on the surface as the last step in device fabrication to combat this issue. Surface passivation is referred to a chemical treatment of the surface with the aim to neutralise the dangling bonds. It is often followed by encapsulation (also sometimes referred to as passivation), a process by which a thin layer of dielectric and chemically non-reactive material is deposited to stabilise the surface. When treating optical devices care needs to be taken to choose a material that is optically

transparent to the wavelengths of interest.

Different types of passivation processes have been demonstrated for InGaAsSb, with varying degrees of success. The simplest one is encapsulation of the surface without prior chemical treatment to limit oxidation. This is often achieved with a polyimide[128], [129], or SU-8 resist[131]. A layer of silicon nitride (Si_3N_4) or silicon dioxide (SiO_2) is also sometimes deposited on the surface as both a passivating and anti-reflection layer[60], [127], [140]. An addition to this process is a chemical treatment of the surface either with an acid-based etchant to remove the oxide layer[135] and/or a sulfide-containing solution to additionally neutralise the dangling bonds prior to encapsulation. Sulfur passivation was found to reduce the native oxide layer and limit surface recombination[156], [157]. Some such solutions include, but are not limited to, thioacetamide (CH_4CSNH_2)[88], ammonium sulphide ($(\text{NH}_4)_2\text{S}$)[88], [156], [158], [159], $\text{Na}_2\text{S}\cdot\text{C}_3\text{H}_7\text{OH}$ [160], octadecylthiol ($\text{CH}_3(\text{CH}_2)_{17}\text{SH}$)[157], and sodium sulfide (Na_2S)[99], [130], [161]. The devices are then often encapsulated in a layer of silicon dioxide (SiO_2)[2], [141] or polyimide[162] to prevent long-term degradation often noted in sulfur-treated devices. It is difficult to ascertain which one of the above techniques is most favourable for the passivation of InGaAsSb devices, as further investigations need to be carried out.

The samples in this work have been passivated with a layer of SU-8 resist, as illustrated in figure 4.9. SU-8 is an epoxy-based, negative photoresist with a very high optical transmission above 360 nm, making it an excellent choice for treatment of infrared devices[163]. Before the resist is applied, the samples are cleaned and dried by following the steps described in section 4.3.1. A small amount of SU-8 is then applied to the surface of the sample with a pipette, and subsequently spun to create a thin uniform layer. An initial speed of 500 rpm for 10 seconds is used to evenly distribute SU-8 across the surface. The speed is then increased to 3000 rpm for 30 seconds to achieve a film thickness of ~ 500 nm. The sample is soft baked at 95 °C for 1 minute and placed in the MJB4 mask aligner ready for exposure.

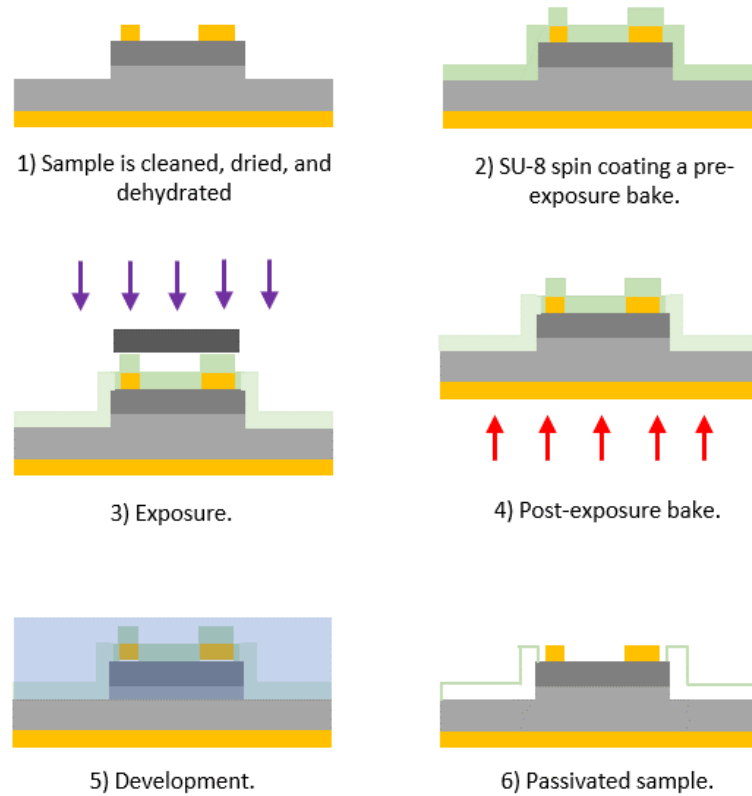


Figure 4.9: Processing steps for the passivation of the photodiodes' sidewalls with SU-8 photoresist.

The alignment process described in section 4.3.2 is followed before the sample is exposed to UV light for 2 seconds through the appropriate pattern on the mask. Since SU-8 is a negative photoresist, parts of the surface that we want to passivate (mesa sidewalls) are exposed. A post-exposure bake ensues at 95 °C for 2 minutes, to complete the epoxy cross-linking which renders it insoluble to liquid developers. The sample is then placed in SU-8 developer (2-methoxy-1-methylethyl acetate) for 1 minute and the solution agitated to aid the development process. The final step is rinsing the sample in fresh developer for ~10 seconds, followed by rinsing in IPA for another ~10 seconds, and drying with the nitrogen gun. Only the exposed parts of the SU-8 should remain on the surface. The samples are now ready for electrical characterisation.

Figures 4.10a and 4.10b show a cross-section of the finished *p-i-n* InGaAsSb photodiode, and a microscopic image of its surface post-fabrication.

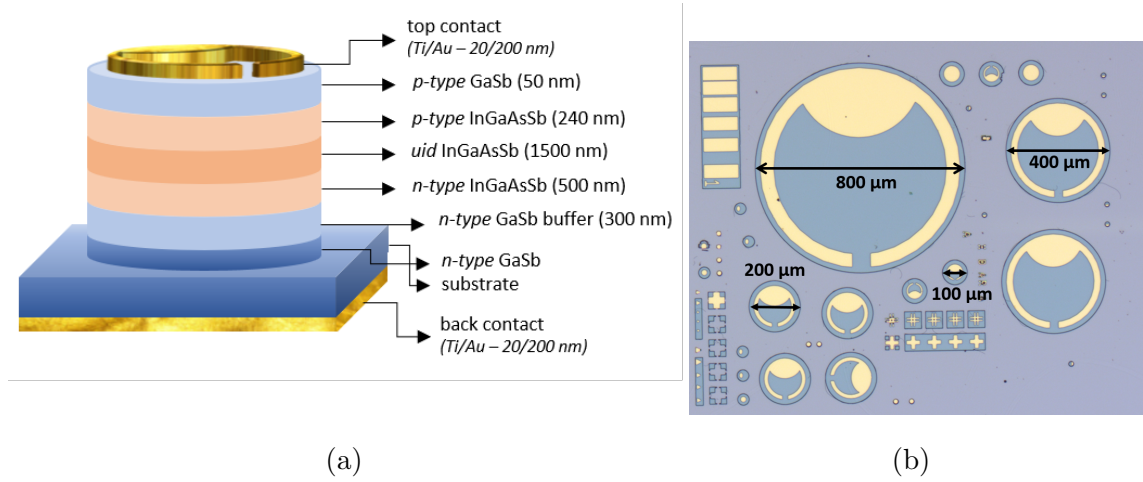


Figure 4.10: (a) *p-i-n* device structure. (b) Surface of a fabricated sample as seen under a microscope showing the circular mesas and the horseshoe top contacts.

4.4 Characterisation

The following section outlines the characterisation techniques utilised in this work. Prior to device fabrication, the spectral response of as-grown samples is investigated via Fourier Transform Infrared spectroscopy (FTIR) which enables the extraction of the bandgap energy as well as the calculation of the absorption coefficient. After fabrication of the devices, further electrical characterisation can ensue, primarily current-voltage (IV) measurements for the purpose of investigating leakage characteristics, dynamic resistance, and quantum efficiency under direct illumination from an infrared laser. Furthermore, capacitance-voltage (CV) measurements shed light on the background carrier concentration in the intrinsic layer. Finally, specific detectivity can be calculated for each device based on the above information.

4.4.1 Fourier Transform Infrared spectroscopy

The first step in device characterisation is Fourier transform infrared spectroscopy (FTIR), which takes place before device fabrication. This technique allows one to measure the amount of light that is transmitted through a sample. This information can then be used to determine the bandgap energy of the material and to calculate the absorption coefficient of the epilayer.

Transmission through the samples was measured with a Bruker Vertex 70 FTIR spectrometer[164]. It is equipped with two light sources - a near infrared (NIR) source consisting of a tungsten halogen lamp, and a mid infrared (MIR) source consisting of a U-shaped silicon carbide piece (globar). The spectrometer is also equipped with two beamsplitters - a KBr and a CaF₂ beamsplitters for MIR and NIR measurements, respectively. The standard detector used for the majority of measurements is a pyroelectric DLaTGS detector which covers a spectral range from 0.83 to 40 μm . The right combination of a source, detector, and a beamsplitter is chosen to perform the transmission measurements. For InGaAsSb samples this is the MIR source, KBr beamsplitter, and the internal DLaTGS detector. This configuration allows for spectral measurements in the range between 1.25 and 28.6 μm . The spectrometer is connected to a PC and is entirely computer-controlled via the spectroscopy software OPUS which is used to configure the spectrometer, specify the measurement parameters, acquire the measurement, as well as display and manipulate the data. At the heart of the spectrometer is the interferometer which is responsible for encoding information into the light by creating an interference pattern. The spectrometer is also equipped with a red (632.8 nm) HeNe laser which controls the position of the moving interferometer mirror, and is also used to determine the data sampling positions[165].

The FTIR spectrometer operation can be explained with reference to figure 4.11. Light from the source is first reflected by a focusing mirror onto the aperture wheel which is used to control the power of incident light. It is then reflected by a collimating mirror onto the beamsplitter which acts as a partial reflector. Part of the

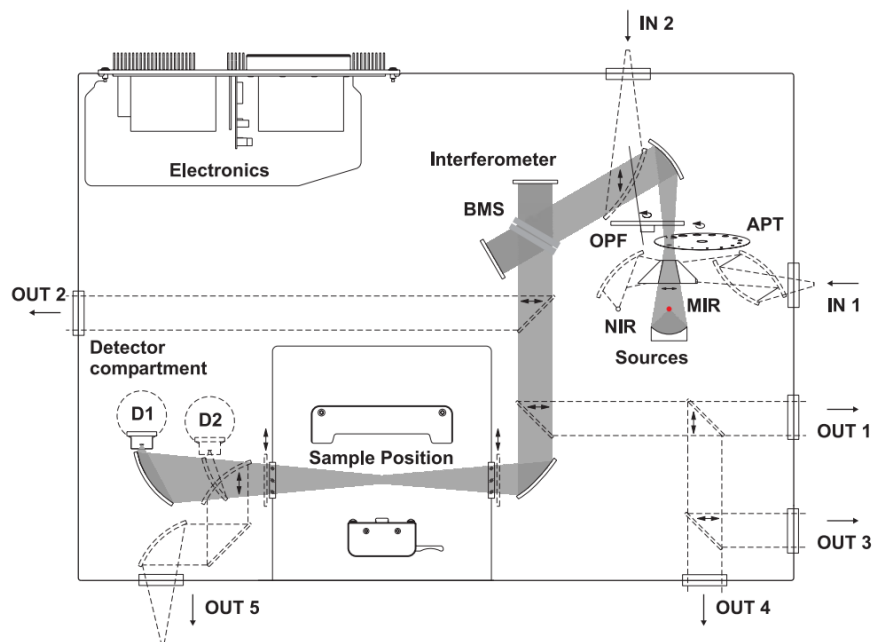


Figure 4.11: A schematic diagram of the Vertex 70 FTIR spectrometer showing the optical path for a typical transmission measurement, with relevant components labelled[165]. OPF is the optical filter wheel, APT is the aperture wheel, BMS is the beamsplitter, and D1 and D2 are detector positions.

light is reflected onto a stationary mirror, while the remaining light is transmitted onto a continuously moving mirror. The two beams are then re-combined at the beamsplitter into a single beam of light. Since the moving mirror is continuously changing the path length of one of the beams, once they recombine the resulting difference in the path lengths of the two beams will create an interference pattern. This part of the spectrometer is known as the interferometer and is permanently aligned. The single beam is then focused by another mirror through one of the windows of the sample compartment and onto the sample. Finally, the light that is transmitted through the sample exists the sample compartment through the second window and is focused onto a detector by the final mirror. The time varying interference pattern (interferogram) is analysed via Fourier transform and re-constructed into a transmission spectrum displayed in OPUS. Note that the GaSb

sample was measured with a different configuration. The tungsten halogen lamp was used as the NIR source, CaF_2 as the beamsplitter, and an external prototype InGaAsSb detector similar to the one reported in reference[140] was used to achieve a spectral range between 1.33 and 2.5 μm .

Prior to measurement, the sample is installed onto a metallic plate with a small circular hole at the centre, and placed inside the sample compartment perpendicular to the beam path. The beam of light passes through the hole in the plate, through the sample (enters via the substrate and exists via the top epilayer surface), and onto the DLaTGS detector (labelled D1 on the diagram in figure 4.11). To ensure correct analysis of the transmitted spectrum, a background measurement must first be taken, with only the empty sample plate in the sample compartment. Since some of the incident light will be reflected by the back surface of the sample at the substrate-air interface, and likewise absorbed by the substrate itself, it is important to ascertain both absorption and reflection due to the substrate alone prior to sample measurement. To achieve this, a measurement is performed on a piece of the substrate wafer.

4.4.2 Current-voltage and quantum efficiency measurements

Current-voltage (IV) measurements are at the core of electrical characterisation of devices presented in this work. Investigating current flow through the diode under reverse bias and dark conditions enables one to ascertain the nature and significance of unwanted leakage currents present in the devices. Likewise, in forward bias the IV relationship will deviate from the ideal diode case due to the presence of both shunt and series resistance which are caused by defects in the material and imperfect contacts respectively (refer to section 2.2.2.1). Furthermore, repeating the above IV measurements but under light conditions with a laser directed at the surface of the device will provide a voltage dependent measurement of the external quantum efficiency.

The IV measurements were taken with a Keithley 2400 sourcemeter and a

Wentworth probe station MP-2010. The Keithley is connected to a PC and externally controlled by a LabView software. Since the samples employ a back contact, instead of being placed directly onto the probe station stage, they were placed on a gold leaf (a thin glass sheet with a thick layer of gold deposited on the surface via thermal evaporation) to ensure a good contact between the probe tip and the back surface of the sample. Hence, one probe tip is placed on the top contact of the device under test, while the other probe tip is placed on the gold leaf. A circuit is thus created between the device and the sourcemeter as can be seen from the diagram in figure 4.12.

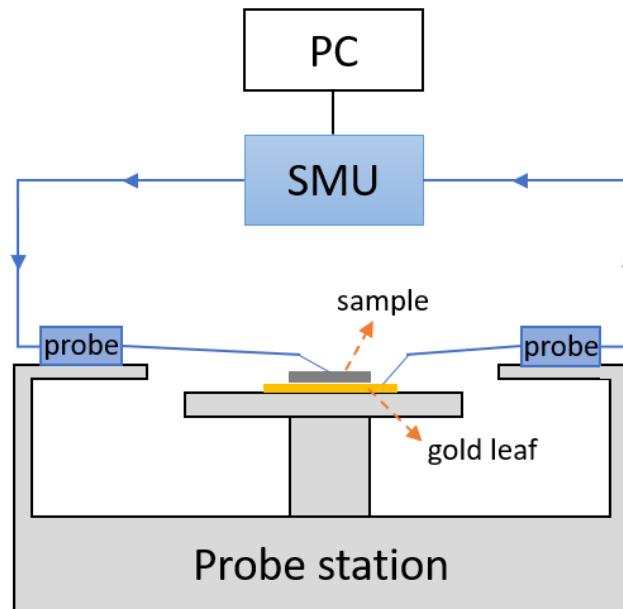


Figure 4.12: A schematic diagram of the IV setup. SMU (sourcemeter unit) is a Keithley 2400.

For quantum efficiency measurements, a $1.55\ \mu\text{m}$ ThorLabs fibre coupled laser source (model S3FC1550) was used to illuminate the devices. The exposed tip of the optical fibre is fixed to a microadjuster to allow for a precise positioning of the laser over the device mesa. The alignment is completed with the aid of a computer controlled ThorLabs C1284R13C camera. Additionally, the diode current is monitored in real time during the alignment process to ensure maximum (and

stable) current output, which would indicate that all of the light from the laser is falling onto the surface of the mesa. The output power of the laser is verified with a reference detector - a commercial InGaAs photodetector (FGA01FC) with a known responsivity of 1.04 A/W at 1.55 μm . The laser output is split so that 10% of the light is incident upon the reference detector, while the remaining 90% is incident upon the sample. The reference detector is operated at -5 V by a Keithley 6340 sourcemeter. The setup can be seen in figure 4.13.

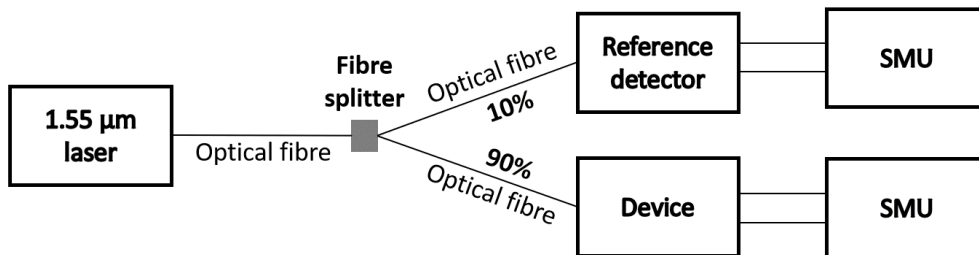


Figure 4.13: A schematic diagram of the QE setup with the InGaAs detector as a reference.

4.4.3 Spectral responsivity measurements

Spectral responsivity/external quantum efficiency measurements were performed with a Bentham PVE300 photovoltaic QE system[166] which consists of a xenon-quartz tungsten halogen dual light source and a TMc300 monochromator[167] with a triple grating turret. The setup is fitted with a sample stage and probes as well as Si, Ge, and PbS reference detectors. The samples in this work were characterised using both Ge and PbS as reference detectors with a combined 800-3000 nm spectral cover. The measurements were performed at zero bias and room temperature. Due to the difficulty in successfully probing the devices with the Bentham probe station which is best suited for larger samples, the measurements were not performed on all samples. Likewise, due to the smallest spot size still being larger than the biggest devices fabricated in this work, the resulting spectrum had to be scaled to the

responsivity measurement obtained with a 1.55 μm laser as described in section 4.4.2.

4.4.4 Capacitance-voltage measurements

Capacitance-voltage (CV) measurements were carried out with an Agilent E4980A precision LCR meter. The meter is first calibrated in the open circuit mode with only one probe in contact with the gold leaf. To enable a CV measurement, an AC voltage is superimposed onto the DC biasing voltage. During measurements, an AC signal amplitude of 25 mV, and a frequency of 1 MHz was used. The phase angle between the measured and applied AC signal was monitored to ensure the measured device was behaving like a capacitor with the expected phase difference of $\sim 90^\circ$. The unintentional doping concentration (uid) of the intrinsic layer can then be extracted by fitting the CV data to a model. The model calculates the capacitance of a device by treating the individual layers as parallel plate capacitors in series. The doping of the p , i , and n regions is varied until the model provides an excellent fit to data.

4.4.5 Capacitance modelling

Capacitance of the p - i - n devices can be calculated by solving Poisson's equation in one dimension. The electric fields, E_i , at layer boundaries of such a structure (illustrated in figure 4.14) can be calculated through

$$D_1 = qN_1X_1 \quad D_2 = qN_2X_2 \quad D_3 = qN_3X_3 \quad (4.2)$$

where q is the electron charge, N_i is the doping concentration, X_i is the depletion width, and D_i is the electric displacement field given by $D = \epsilon_0\epsilon_r E$. Here, ϵ_0 and ϵ_r are the permittivity of vacuum and the dielectric constant respectively. Combining the above equations yields

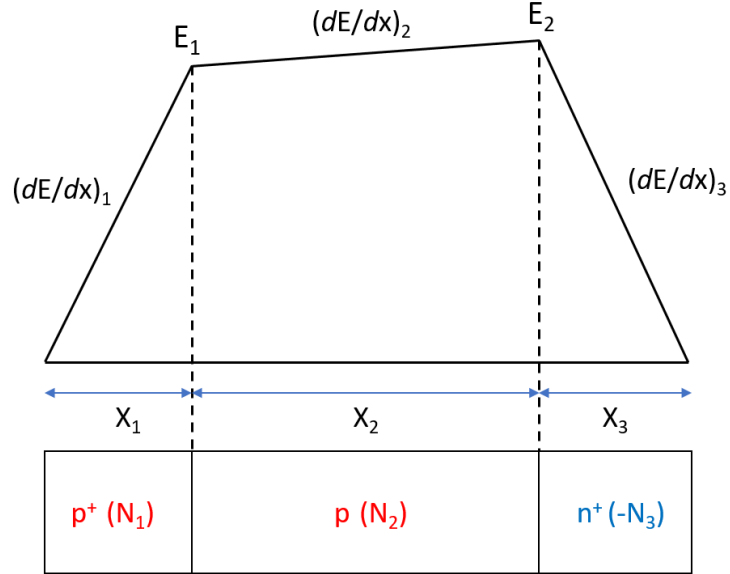


Figure 4.14: Electric field distribution in a p - i - n device structure with N_i doping concentrations, and X_i depletion widths, assuming p and n regions are fully depleted of carriers. E_1 and E_2 are the boundary electric fields.

$$X_3 = \frac{-qN_1X_1 - qN_2X_2}{qN_3} \quad (4.3)$$

The total voltage drop, V , across the device, given by the sum of the built-in and applied voltages, is related to the integral of the electric field through

$$V = \frac{1}{2} \left(\frac{D_1 X_1}{\epsilon_1} + \frac{D_2 X_3}{\epsilon_3} + \frac{(D_1 + D_2) X_2}{\epsilon_2} \right) \quad (4.4)$$

Substitution of equations 4.2 and 4.3 into equation 4.4 gives a quadratic equation in X_1

$$X_1 = \frac{-b + \sqrt{b^2 - 4ac}}{2a} \quad (4.5)$$

where the a , b , and c coefficients are given by

$$a = N_1 \left(\frac{1}{\epsilon_1} - \frac{N_1}{N_3 \epsilon_3} \right) \quad (4.6)$$

$$b = 2N_1 \left(\frac{X_2}{\epsilon_2} - \frac{N_2 X_2}{N_3 \epsilon_3} \right) \quad (4.7)$$

$$c = \frac{-(N_2 X_2)^2}{N_3 \epsilon_3} + \frac{X_2^2 N_2}{\epsilon_2} - \frac{2V}{q} \quad (4.8)$$

Finally, the capacitance of the device can be calculated through

$$C = \epsilon_0 \epsilon_r / W \quad (4.9)$$

where W is the total depletion width of all three layers.

The above calculation can be extended for an arbitrary number of layers, which is often useful when dealing with layer interfaces where the change in the doping concentration is not always abrupt. Insertion of one or more thinner layers with intermediate doping concentrations at the interfaces sometimes provides a better fit to experimental data. An example of such a fit can be seen in figure 4.15.

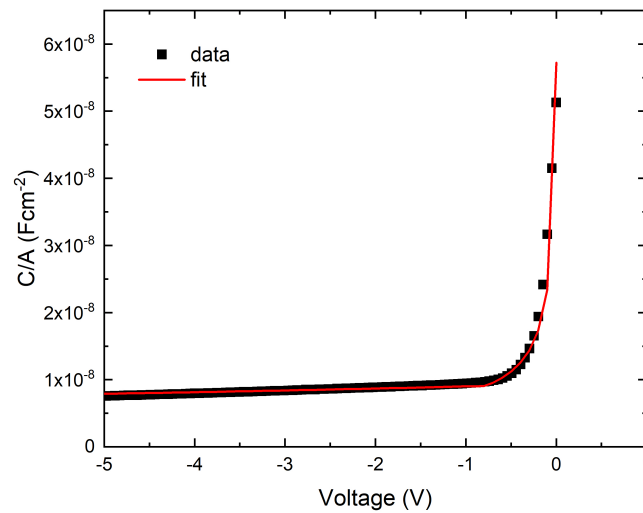


Figure 4.15: An example of the CV model fit to experimental data.

More information about the extended calculation for N number of layers can be found in reference [168].

Chapter 5

Results I

The following sections focus on the MBE growth of InGaAsSb *p-i-n* photodiodes, as well as the growth of InGaAsSb single layers, outlining substrate preparation and epilayer growth as well as subsequent characterisation via x-ray crystallography. Moreover, optical characterisation results are presented, with a focus on absorption coefficient data and bandgap energy.

5.1 Photodetector design

In order to investigate the material properties of the InGaAsSb alloy and characterise InGaAsSb-based photodetectors, a homojunction *p-i-n* structure illustrated in figure 5.1 was chosen. The intrinsic region thickness of 1500 nm is sufficiently thin to limit signal attenuation during transmission measurements, but thick enough to provide good absorption coefficient data, high quantum efficiency, and reliable unintentional background doping information. The intrinsic region is clad with a tellurium-doped, 500 nm thick *n*-type InGaAsSb layer with a carrier concentration of $3 \times 10^{18} \text{ cm}^{-3}$, and a beryllium doped, 250 nm thick *p*-type InGaAsSb layer with a carrier concentration of $2 \times 10^{18} \text{ cm}^{-3}$. The top *p*-type InGaAsSb layer is made thinner to minimise absorption outside of the depletion region, and is slightly lighter doped than the bottom *n*-type InGaAsSb. With this configuration, the depletion region

extends further into the p -layer to ensure the collection of photogenerated carriers nearer the surface of the top-illuminated device by the strong electric field. The 50 nm GaSb cap serves as a contact layer and is highly Be-doped with a concentration of $4 \times 10^{18} \text{ cm}^{-3}$. The cap is kept sufficiently thin to ensure absorption in this layer is negligible.

p -type GaSb	Be-doped, $4 \times 10^{18} \text{ cm}^{-3}$	50 nm
p -type InGaAsSb	Be-doped, $2 \times 10^{18} \text{ cm}^{-3}$	250 nm
uid InGaAsSb		1500 nm
n -type InGaAsSb	Te-doped, $3 \times 10^{18} \text{ cm}^{-3}$	500 nm
n -type GaSb buffer	Te-doped, $4 \times 10^{18} \text{ cm}^{-3}$	300 nm
n -type GaSb substrate	Te-doped, $1 \times 10^{17} \text{ cm}^{-3}$	

Figure 5.1: InGaAsSb p - i - n photodetector structure showing layer thicknesses and doping profile.

Since this alloy can be grown lattice-matched to GaSb for a wide range of compositions, with indium fractions up to $\sim 30\%$ before encountering the miscibility limit (refer to section 3.2.1), multiple $\text{In}_x\text{Ga}_{1-x}\text{As}_y\text{Sb}_{1-y}$ p - i - n photodiodes were grown with different compositions ranging from $x = 0$ (GaSb), to $x = 0.3$, over several growth campaigns. The corresponding As fraction that satisfies the lattice matching condition according to Vurgaftman[100] is calculated through $(\text{GaSb})_{1-x}(\text{InAs}_{0.91}\text{Sb}_{0.09})_x$. For simplicity, and due to most epilayers being lattice-matched to the substrate within 250 arcseconds, only the In fraction will be indicated henceforth. The list of grown p - i - n samples and the degree of lattice mismatch is summarised in table 5.1.

Additionally, single layers of both GaSb and InGaAsSb were grown on undoped GaAs for further optical characterisation, since transmission data above 0.65 eV of the p - i - n samples is obscured by the absorption tail of the GaSb substrate. This

In fraction (%)	device number	lattice mismatch (arcsec)
0	XK1788	0
4.3	XK1744	72
5	XK1635	250
10	XK1573	< 20
12	XAB1582	~ 280
15	XLH1503	~ 100
20	XK1785	~ 130
26	XAC1476	~ 120
30	XK1779	/

Table 5.1: $\text{In}_x\text{Ga}_{1-x}\text{As}_y\text{Sb}_{1-y}$ *p-i-n* photodiodes grown via MBE, with indium fractions between $0 \leq x \leq 0.3$. The degree of lattice mismatch is indicated for each sample.

is particularly relevant in the case of the GaSb *p-i-n* grown on GaSb, since the epilayer's absorption and bandgap are completely obscured by the absorption of the thick substrate. In order to differentiate between the epitaxial GaSb and the doped substrate, it is necessary to grow GaSb on undoped GaAs, which is optically semi-transparent (transmits ~60% of incident light) in the wavelength range of interest. However, growing these transmission layers on GaAs introduces interference effects due to the relatively large difference in refractive indices of InGaAsSb and GaAs, which needs to be accounted for during data analysis. The structure of the InGaAsSb and GaSb transmission samples grown on undoped GaAs is shown in figures 5.2a and 5.2b, respectively.

Firstly, a 200 nm undoped GaAs buffer was grown, followed by a 500 nm GaSb layer, before the final layer of InGaAsSb is deposited. Interfacial misfit (IMF) arrays, which will be discussed more in section 5.3, are employed to enable growth on a mismatched substrate. The only difference between the InGaAsSb and GaSb samples is their thickness - InGaAsSb layers were kept at 1 μm , while

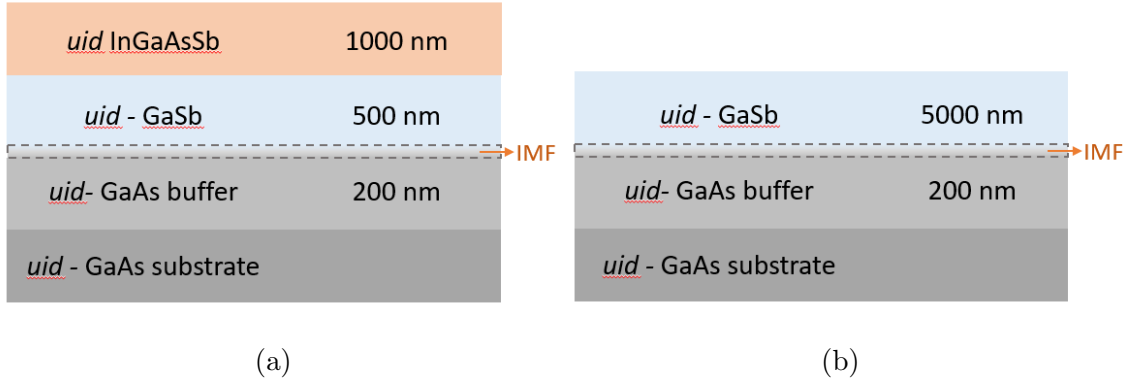


Figure 5.2: Transmission sample structure of (a) InGaAsSb, and (b) GaSb.

the GaSb layer was grown thicker at $5 \mu\text{m}$. While such a thick layer significantly attenuates the transmission signal for wavelengths above the GaSb bandgap due to its strong absorption, it also minimises the effect of interference fringes which allows data extraction around and below the absorption edge where the absorption is much weaker. Since we obtain a clear view of the sub-bandgap absorption for the InGaAsSb samples grown on GaSb, a thinner layer of InGaAsSb was grown on GaAs in favour of a stronger signal for wavelengths above the absorption edge. Table 5.2 lists all of the transmission layers grown and their lattice mismatch.

In fraction (%)	device number	lattice mismatch (arcsec)
0	XGS2409	0
5	XK1787*	195
10	XK1786*	137
14	XAB1309	367
20	XAB1308*	368
25	XAB1315	540

Table 5.2: $\text{In}_x\text{Ga}_{1-x}\text{As}_y\text{Sb}_{1-y}$ transmission layers grown via MBE, with indium fractions between $0 \leq x \leq 0.25$. The degree of lattice mismatch is indicated for each sample. *Samples grown on single side polished GaAs.

The single layers were allowed a higher degree of lattice mismatch due to the focus being on the high energy absorption rather than the bandgap. Unfortunately, none of the InGaAsSb transmission samples could be used for the purpose originally intended due to several reasons. Firstly, the samples marked with an asterisk were grown on single-side polished GaAs substrates, which rendered FTIR transmission measurements meaningless due to the diffuse reflection of incident light from the back surface of the samples. While it was possible to attempt reflection measurements with the FTIR in conjunction with the reflection accessory, this was deemed unfeasible due to the added complications with the setup and data analysis. Secondly, the absorption coefficient could not be extracted even from the samples grown on double-side polished GaAs substrates due to their slightly more complicated structure compared to the GaSb sample with regards to interference analysis which rendered the chosen approach unusable. The interference modelling will be explain more in section 5.5.1. The growth of photodetectors and transmission layers is described in more detail in sections 5.2 and 5.3, respectively.

5.2 Growth of InGaAsSb *p-i-n* photodiodes

The InGaAsSb photodiodes are grown on $\frac{1}{4}$ 2 inch (100) *n*-GaSb (Te-doped) substrate wafers from Wafertech[169]. Each 2 inch wafer is cleaved into four equal pieces, which are individually loaded onto substrate holders and into the load lock. After the completion of the load lock bake, the wafer is transferred to the buffer chamber by following the steps outlined in section 4.1. The wafer is then outgassed at 350 °C for several hours, or until the pressure in the buffer chamber has fallen below $\sim 5 \times 10^{-8}$ bar. Finally, the wafer is transferred into the growth chamber, where substrate deox is initiated.

The substrate is heated up to the GaSb oxide desorption temperature in incremental steps, starting from 200 °C, while under continuous azimuthal rotation at a rate of 10 degrees per second. At $\sim 450 - 500^\circ\text{C}$, Sb flux is introduced to

compensate for the faster desorption of Sb from the surface. As the substrate temperature is further increased, the surface is monitored carefully until spots start to appear on the RHEED screen, indicating the beginning of oxide desorption (typically at $\sim 540^\circ\text{C}$). The temperature is then increased by a further 10°C , and maintained for ~ 10 minutes. The subsequent removal of the oxide layer unveils a rough GaSb surface with a bright spotty pattern visible on RHEED, indicative of 3D surface structuring. After the completion of oxide desorption, the substrate temperature is decreased to GaSb growth temperature of 500°C . Once the temperature has stabilised, Ga flux is introduced and growth of the GaSb buffer ensues at the growth rate of 1 ML/s . Within the first few monolayers of growth, the surface smooths out and the RHEED pattern becomes streaky, indicating favourable 2D growth. GaSb is grown under Sb stable conditions which are represented by the 1×3 reconstruction pattern visible during growth.

When growing a quaternary alloy such as InGaAsSb, several considerations need to be made. Firstly, the composition needs to be lattice-matched to the GaSb substrate. Secondly, the overall V/III growth rate ratio needs to be adjusted to account for the lower sticking coefficient of group Vs, and finally, the difference in the relative incorporation of As and Sb into the crystal, which was shown to also be temperature dependent, needs to be accounted for. It was shown that Sb incorporation decreases at increasing temperatures, which means that any change in the growth temperature also changes the As/Sb ratio. Multiple calibration growths are often needed to achieve an acceptable lattice-matched composition.

While the substrate deox is performed manually, epitaxial growth is controlled by the Veeco's Molly Growth Control Software[170]. Molly is used to write and execute recipes to allow for precise sample growth with abrupt interfaces and carefully controlled layer thicknesses. Each recipe starts with the GaSb buffer growth, and is initiated after a successful oxide removal and once the substrate temperature has stabilized at the correct growth temperature. After the 300 nm buffer has been grown, the substrate temperature is lowered to the appropriate growth temperature

for InGaAsSb layers, between 440 and 450 °C. Cells containing group III elements (In and Ga) are pre-heated to precise temperatures to ensure the correct growth rate ratio corresponding to a particular In/Ga compositional ratio. Growth rates as a function of cell temperatures are pre-calibrated via RHEED oscillations, as described in section 4.1. Similarly, dopant cells (Tellurium for *n*-type, and Beryllium for *p*-type) are pre-heated to the appropriate temperature to provide the required doping concentration in each layer. The valve openings of cells containing group V elements (As and Sb) are set to a desired value to give the correct As/Sb ratio that satisfies the lattice matching condition. Finally, cell shutters of all constituent elements and dopants are opened to allow the evaporated elements to escape into the vacuum and onto the surface of the substrate. InGaAsSb layers were grown at a rate of 1 ML/s, while the total group V/III growth rate ratio was maintained at ~ 1.8 across all samples. Higher group V flux is necessary to compensate for their lower sticking coefficient.

5.3 Growth of InGaAsSb transmission layers

InGaAsSb transmission layers were grown on undoped $\frac{1}{4}$ 2 inch (100) GaAs substrate wafers from Wafertech[171]. Most of the substrate preparation steps outlined in the previous section are followed, with a few minor differences. GaAs outgas and deox are achieved at higher temperatures of 400 and 580 °C, respectively. Unlike GaSb, GaAs starts exhibiting a spotty pattern on RHEED before the oxide desorption temperature is reached, due to it having a thinner native oxide layer. However, the successful completion of the oxide removal is signified by a notable increase in spot brightness. As flux is introduced during deox to compensate for the desorption of As atoms from the surface. Since the melting point of GaAs is much higher than its oxide desorb temperature, the deox steps can be included in the recipe without the risk of compromising the quality of the surface.

After the removal of the surface oxides, growth of the GaAs buffer proceeds

at a rate of 0.6 ML/s and a temperature of 565°C. The surface is now ready for the implementation of the IMF array to allow growth of GaSb on a mismatched substrate. The first step is a brief cessation of arsenic flux which creates a Ga terminated growth surface, followed by the addition of Sb flux for several minutes, before Ga flux is finally introduced, and growth of the GaSb layer can proceed. During this process, the substrate temperature is incrementally reduced from the GaAs to the GaSb growth temperature. Successful IMF is represented by a 2x8 RHEED pattern. Once GaSb growth is initiated, the RHEED pattern first transforms into spots, and finally streaks with a 1x3 reconstruction pattern as the surface smooths out and a good quality epilayer is formed. After a few hundred nanometers of the intermediate GaSb layer have been deposited, the growth of InGaAsSb layer can finally ensue.

The IMF implementation process essentially enables GaSb to grow fully relaxed (> 99% relaxation) without introducing threading dislocations which extend into the electrically active region. The strain relief due to a large lattice mismatch between the two materials occurs only through an array of lateral misfit dislocations which do not extend into the electrically active layers[168]. More detail about this technique can be found in reference [168].

5.4 XRD analysis

As previously mentioned, X-ray diffraction measurements are an important step in achieving high quality, lattice-matched epitaxial layers, particularly when working with quaternary III-V alloys. XRD measurements, detailed in section 4.2, were performed on every sample immediately after growth to infer the degree of lattice mismatch and the corresponding composition of InGaAsSb layers. For photodetector samples, if lattice mismatch exceeded 150 arcseconds, the sample was re-grown until a satisfactory result was achieved. This was done primarily to minimise the occurrence of any strain-induced defects in the electrically active region, which

would negatively impact the device properties. Additionally, any change in the composition also changes the lattice constant, and by extension the bandgap energy of the material. Therefore, in order to obtain a fair representation of the variation of the InGaAsSb bandgap with In fraction, it is important to grow very closely lattice-matched alloys. The InGaAsSb transmission layers were allowed a higher degree of mismatch since their main purpose was to extend the absorption data beyond the GaSb absorption tail at 0.65 eV, hence the impact of potential strain-induced defects and dislocations on the material quality, as well as the slight shift in the bandgap energy could be ignored.

After obtaining the measurements, the Bede RADS software was used to simulate the diffraction spectrum of the structure to confirm the exact composition of the InGaAsSb layers. What makes the compositional calibration via XRD modelling possible, is the fact that group III elements (In and Ga) have a unity sticking coefficient. This knowledge, combined with the group III growth rate calibrations, allows us to fix the In and Ga fractions as known parameters of the modelled structure, and vary the As and Sb fractions until the simulated spectrum closely matches the measured one. While there is potential for error when determining the composition of InGaAsSb layers due to the reliance on group III growth rates, they were shown to be extremely stable and were found to deviate by no more than 5% of the calibrated value over extended growth campaigns. An attempt was made to provide an independent measure of the III/III (Ga/In) ratio through an XPS (X-ray photoelectron spectroscopy) study conducted in collaboration with another research group. However, despite the lengthy characterisation of a large number of samples and comparison to binary alloys as references, the uncertainties remained excessive and ultimately this technique could not provide useful precise compositional information. While the group V growth rates were also calibrated via RHEED oscillations, due to their non-unity sticking coefficient and the fact that both the overall V/III ratio, as well as the relative As/Sb incorporation is temperature sensitive, it is often necessary to re-grow samples after XRD analysis

with a slight change in the Sb and/or As valve positions. In the case of very dilute alloy compositions, the As bulk temperature was additionally lowered to enable such low As fractions that satisfy the lattice-matching condition.

$\text{In}_x\text{Ga}_{1-x}\text{As}_y\text{Sb}_{1-y}$ *p-i-n* samples with $0 < x < 0.15$ exhibit well defined and narrow epilayer peaks, as evident from XRD data of two lattice-matched (figures 5.3a and 5.3c) and two mismatched (figures 5.3b and 5.3d) samples, indicating a uniform crystal growth.

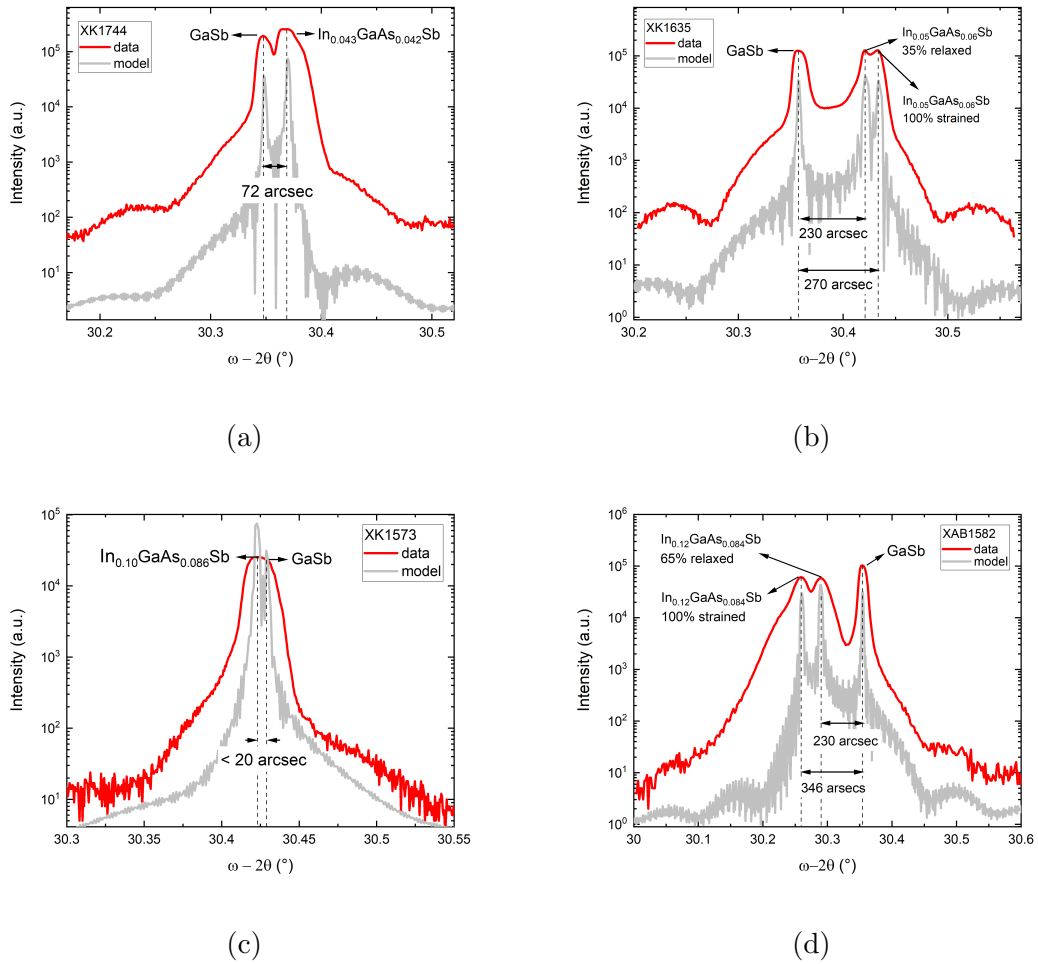


Figure 5.3: X-ray diffraction data for $\text{In}_x\text{Ga}_{1-x}\text{As}_y\text{Sb}_{1-y}$ *p-i-n* samples with: (a) $x = 0.043$, (b) $x = 0.05$, (c) $x = 0.1$, and (d) $x = 0.12$.

Alloys with $x = 0.043$ and 0.1 are extremely well lattice-matched, with the

InGaAsSb epilayers only 72 and < 20 arcseconds apart, respectively. The simulated diffraction spectra are in very good agreement with the measured ones, and the As content is within a fraction of a percent of the target.

The two mismatched alloys with $x = 0.05$ and 0.12 , exhibit two epilayer peaks each, 50 and 100 arcseconds apart, respectively. Due to a larger degree of lattice mismatch, around ~ 300 arcseconds in both cases, the InGaAsSb epilayers initially grew strained until reaching the critical thickness, at which point the strain could no longer be supported. This resulted in the relaxation of the successive layers, evident from the appearance of the second peak on the XRD scan, located closer to the substrate peak. The degree of relaxation depends on the degree of lattice mismatch - if sufficiently great, the alloy will grow fully relaxed from the start. It is difficult to ascertain precisely where this cutoff may be and the degree of relaxation associated with each intensity peak. However, an assumption can be made that, for a moderate degree of mismatch, the InGaAsSb layer initially grows 100% strained. This is further supported by the fact that, in order to fit the measured spectra assuming the InGaAsSb initially grows with a certain degree of relaxation, group V content needs to significantly deviate from the expected one, as inferred from growth rate calibrations, which is deemed unlikely. With the above assumption, graphs in figures 5.3b and 5.3d can be analysed as follows.

The sample with $x = 0.05$ initially grew 100% strained with an As content 1.65% higher than the lattice-matched case, resulting in a primary diffraction peak 270 arcseconds to the right of the substrate peak. A higher As content corresponds to a lower lattice constant, which caused a build-up of tensile strain. Strain-relief was achieved through the 35% relaxation of the successive InGaAsSb layers, resulting in a secondary diffraction peak located closer to the substrate, only 230 arcseconds off. Hence the two peaks visible on the XRD scan in figure 5.3b correspond to strained and relaxed InGaAsSb layers with the same composition. The sample with $x = 0.12$ grew with a larger degree of mismatch (~ 350 arcseconds) due to an As content 2.06% lower than the lattice-matched target. The lower As content increased the

lattice constant which lead to a build-up of compressive strain and finally caused a greater degree of relaxation (65%) of the successive InGaAsSb layers. The relaxed peak is 230 arcseconds to the left of the substrate peak. The two samples, while fully processed and characterised, were not included in the analysis of the compositional trend due to the higher degree of mismatch present.

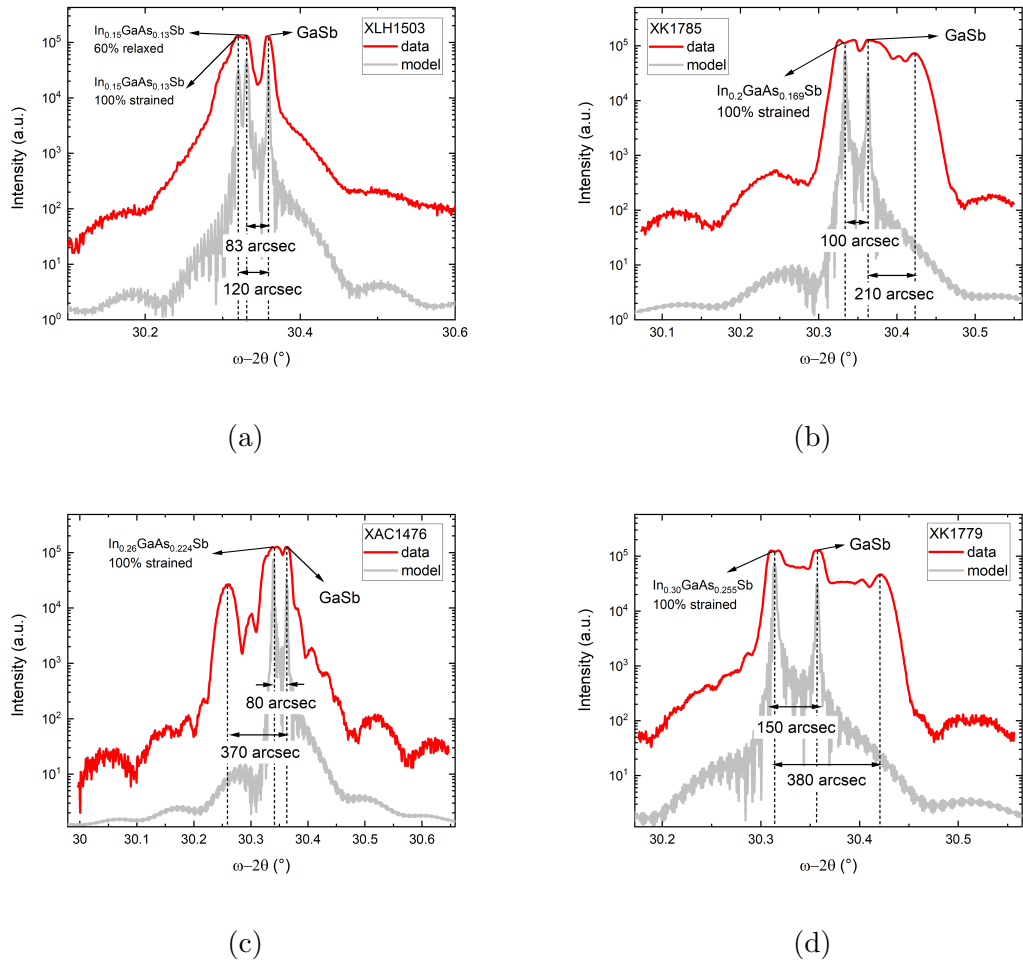


Figure 5.4: X-ray diffraction data for $\text{In}_x\text{Ga}_{1-x}\text{As}_y\text{Sb}_{1-y}$ *p-i-n* samples with: (a) $x = 0.15$, (b) $x = 0.20$, (c) $x = 0.26$, and (d) $x = 0.30$.

Samples with $0.15 < x < 0.3$ exhibit a general broadening of XRD peaks and even decomposition into multiple peaks despite their mismatch never exceeding 150 arcseconds, as can be seen in figures 5.4a-5.4c. The sample with the highest In

fraction of 30% shown in figure 5.4d could not be grown within the lattice-matched range at this growth temperature.

The analysis of the diffraction spectra is more difficult in this case due to the large number and spread of the peaks. Attempts have been made to fit the multiple peaks with various degrees of relaxation of the InGaAsSb epitaxial stack, but with limited success. This is due to the epilayer peaks being located at both sides of the substrate peak, suggesting certain regions of the bulk InGaAsSb contain excess As, while others lack in As. One potential explanation is an instability in As and/or Sb fluxes. However, this is deemed unlikely since the samples were grown over multiple growth campaigns. The most likely explanation for this large variability in group V content is phase separation, where the alloy decompositions into GaAs- and InSb-rich phases. The phase separation worsens as we approach the onset of the miscibility limit, culminating finally in the 30% sample which exhibits not only multiple peaks spread out ~ 400 arcseconds around the substrate peak, but the region between the peaks also remains relatively high and flat in intensity.

Phase separation in InGaAsSb alloys is a known issue, and is of thermodynamical origin (refer to section 3.2.1). Growth of this material system via epitaxy techniques that require near-equilibrium conditions is extremely challenging, and seldom produces a uniform material due to its tendency to decompose into GaAs- and InSb-rich quaternary phases[36], [37]. While the growth of InGaAsSb with suppressed phase separation was shown possible via MBE for a wider range of compositions[18], [110], it remains dependant on the specific growth conditions employed for each composition. In general, lower growth temperatures were correlated with a lesser degree of phase separation and increased material uniformity for alloys with higher In and As fractions[18], [34], [35]. In this work, the growth parameters were optimised for dilute alloy fractions and were fixed for all growth campaigns which resulted in non-ideal growth conditions for alloys with $x > 0.15$, as evidenced by the onset of phase separation in these samples. This is believed to be in large part due to the growth temperature which was too high for these alloys. While maintenance of the

same growth conditions felt important to obtain a fair comparison between different epitaxial layers, a lower growth temperature might be beneficial for samples with alloy fractions greater than 15%.

5.5 Optical characteristics

5.5.1 Absorption coefficient

Transmission analysis

Absorption coefficient of the InGaAsSb layers was calculated from the transmission data taken with the FTIR spectrometer, as described in section 4.4.1. The measurement was taken on a single $\sim 13 \text{ mm}^2$ spot from the centre of each 1/4 2" sample. Given the size of the spot, a single measurement would give a representative transmission spectrum even in samples with observed phase separation. Repeating the measurement on different points on the sample resulted in very slight variations, i.e the samples were highly uniform. An example of the transmission spectrum of a *p-i-n* sample and the GaSb substrate is shown in figure 5.5.

Transmission through the multi-layer structure can be understood with reference to figure 5.6, where the *p*, *i*, and *n* layers are treated as a single InGaAsSb layer.

Transmission through the InGaAsSb layer, T_2 , is then given by:

$$T_2 = T_{InGaAsSb} = \frac{T_{sample}}{T_3 T_1} \quad (5.1)$$

where T_{sample} is directly measured with the FTIR spectrometer, and T_1 and T_3 are transmission through the GaSb substrate and cap, respectively, and are given by equation 2.2. Since $R_1 = R_4 = R$ and $R_2 = R_3 \approx 0$, the final expressions for the transmission through the substrate and cap can be simplified to:

$$T_1 = \frac{(1 - R)\exp(-\alpha_{GaSb}t_{subs})}{1 - R\exp(-2\alpha_{GaSb}t_{subs})} \quad (5.2)$$

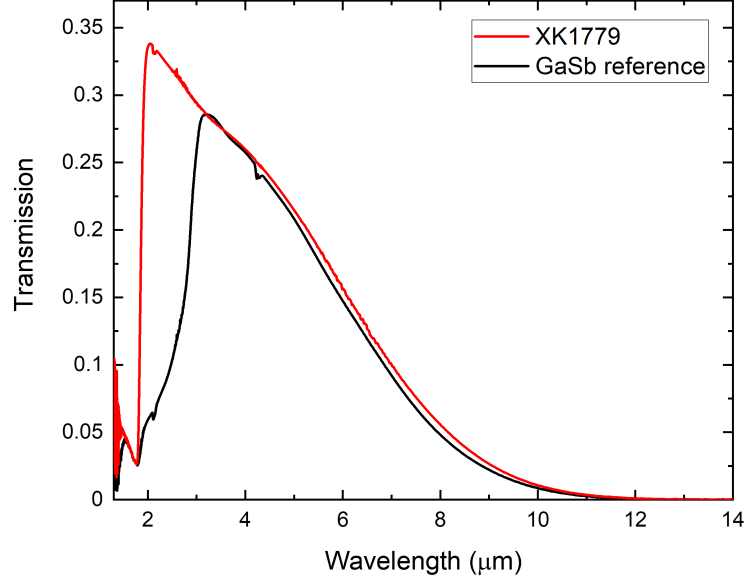


Figure 5.5: Transmission spectra of the XK1779 sample and the GaSb substrate reference.

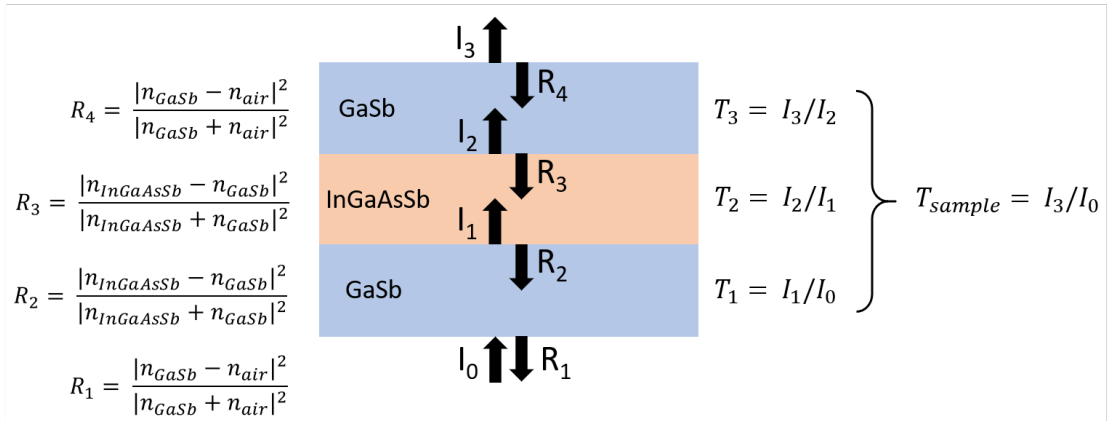


Figure 5.6: Diagram of the transmission and reflection through the p - i - n structure.

$$T_3 = \frac{(1 - R)\exp(-\alpha_{GaSb}t_{cap})}{1 - R\exp(-2\alpha_{GaSb}t_{cap})} \quad (5.3)$$

where R is given by $|n_{GaSb} - 1|^2 / |n_{GaSb} + 1|^2$. The wavelength-dependent refractive index of GaSb is taken from literature[78], [172]. Transmission through the

InGaAsSb layer is also given by equation 2.3. However, in this case reflection at the GaSb-InGaAsSb interface is approximately zero due to their very similar refractive indices[42], allowing us to simplify the equation to:

$$T_{InGaAsSb} = \exp(-\alpha_{InGaAsSb}t_{InGaAsSb}) \quad (5.4)$$

Finally, by combining equations 5.1 and 5.4 and solving for α , we obtain the expression for the absorption coefficient of the InGaAsSb layer:

$$\alpha = \frac{1}{t} \ln \left(\frac{T_1 T_3}{T_{sample}} \right) \quad (5.5)$$

where t is the thickness of the InGaAsSb layer.

The absorption coefficient of the GaSb substrate can be calculated from the transmission data of the substrate alone, which is given by equation 2.3. Transmission is measured on a piece of the substrate wafer. Since the reflection at the front and back surfaces is non-negligible in this case, the absorption coefficient of the GaSb substrate is given by the slightly more involved expression:

$$\alpha_{GaSb} = \frac{1}{t_{subs}} \ln \left(\frac{1}{2T_{subs}} \left(\sqrt{4R^2 T_{subs}^2 + (-R^2 + 2R - 1)^2} + R^2 - 2R + 1 \right) \right) \quad (5.6)$$

Similarly, the absorption coefficient of the epitaxial GaSb, was calculated from the transmission data of the thick 5 μm GaSb sample grown on GaAs, shown in figure 5.7a as a function of wavelength, and 5.7b as a function of energy. Prior to measurement being taken the sample was treated with an HF solution to remove the unintentional material deposit from the back surface of the sample that was introduced during growth.

It is evident that the above bandgap absorption (for $\lambda > \sim 1.7\mu\text{m}$ in figure 5.7a, and $E_p < \sim 0.73$ eV in figure 5.7b) is affected by the interference fringes caused by the relatively large difference in refractive indices between GaAs and GaSb. Therefore, in order to appropriately analyse the transmission data, a consideration of the phase angle difference between the reflected and transmitted light at the

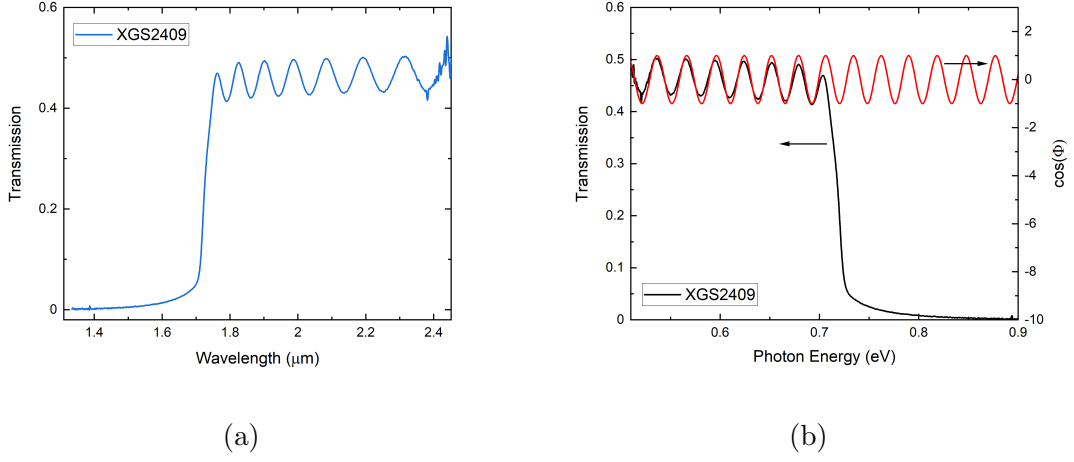


Figure 5.7: (a) Transmission against wavelength of the thick GaSb on GaAs sample. (b) Cosine of the phase angle, ϕ , as a function of photon energy superimposed onto the raw transmission data.

GaAs-GaSb interface needs to be made. Transmission through the structure in this case can be understood with reference to figure 5.8.

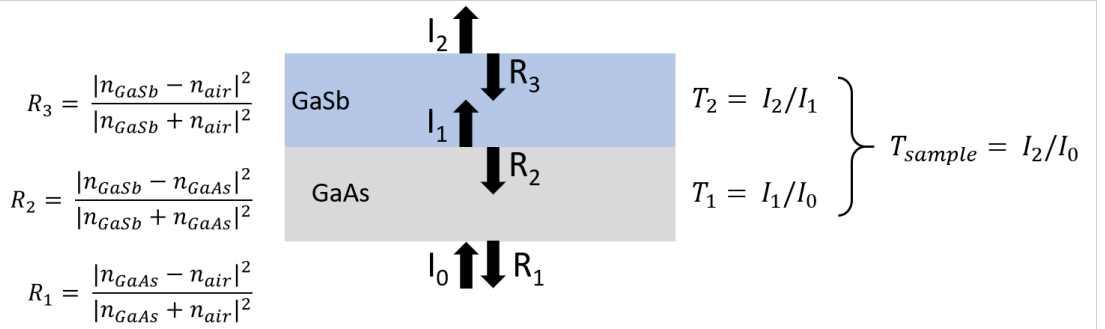


Figure 5.8: Diagram of the transmission and reflection through the GaSb sample.

In this case, transmission through the GaSb layer is given by:

$$T_2 = T_{GaSb} = T_{sample}/T_{GaAs} \quad (5.7)$$

where T_{GaAs} is transmission through the GaAs substrate. Since absorption in the GaAs substrate is negligible ($\alpha_{GaAs} \approx 0$), and the interference effects can be ignored

due to the thickness of the substrate which is much greater than the wavelengths of interest ($t_{GaAs} \gg \lambda$), then the transmission through the GaAs layer is given by:

$$T_{GaAs} = \frac{(1 - R_1)(1 - R_2)}{1 - R_1 R_2} \quad (5.8)$$

where R_1 and R_2 are the reflectivities at the GaAs-air and GaAs-GaSb interfaces, respectively, given by:

$$R_1 = \frac{|n_{GaAs} - n_{air}|^2}{|n_{GaAs} + n_{air}|^2} \quad (5.9)$$

$$R_2 = \frac{|n_{GaSb} - n_{GaAs}|^2}{|n_{GaSb} + n_{GaAs}|^2} \quad (5.10)$$

The wavelength-dependent refractive index of GaAs is taken from literature[173]. Transmission through the GaSb layer alone is also given by equation 2.5, such that

$$T_{GaSb} = \frac{(1 - R_2)(1 - R_3)\exp(-\alpha_{GaSb}t_{GaSb})}{1 - 2\sqrt{R_2 R_3}\exp(-\alpha_{GaSb}t_{GaSb})\cos(\phi) + R_2 R_3 \exp(-2\alpha_{GaSb}t_{GaSb})} \quad (5.11)$$

where R_3 is the reflectivity at the GaSb-air interface, and ϕ is the phase angle between the transmitted and reflected light given by $4\pi n_{GaSb}t_{GaSb}/\lambda$. By substituting equation 5.11 into equation 5.7 and solving for α_{GaSb} , we obtain the final expression for the absorption coefficient of GaSb:

$$\alpha_{GaSb} = \frac{1}{t_{GaSb}} \ln \left(\frac{1}{2T_{sample}} (\sqrt{a - 4R_2 R_3 T_{sample}^2} + b) \right) \quad (5.12)$$

where the a and b coefficients are given by:

$$a = (-2\sqrt{R_2 R_3} T_{sample} \cos(\phi) + R_2 T_{GaAs} - R_2 R_3 T_{GaAs} + R_3 T_{GaAs} - T_{GaAs})^2 \quad (5.13)$$

$$b = 2\sqrt{R_2 R_3} T_{sample} \cos(\phi) - R_2 T_{GaAs} + R_2 R_3 T_{GaAs} - R_3 T_{GaAs} + T_{GaAs} \quad (5.14)$$

Figure 5.7b shows excellent agreements between the calculated phase angle and the interference fringes observed in the measured data.

As previously mentioned, three out of the five InGaAsSb single layers were grown on single side polished GaAs substrates, as indicated by the asterisk in table 5.2. Unfortunately, it was not possible to perform transmission measurements on such samples due to the roughness of the back surface which diffused the incident light. Hence the absorption coefficient of these samples was not calculated. Moreover, the transmission through the remaining two InGaAsSb samples grown on double side polished GaAs substrates could not be appropriately analysed due to their three-layer structure with different reflectivities from the front and back surfaces. This rendered the above model inapplicable, i.e. the interference fringes could not be removed from the measured spectra and a different model needs to be employed or developed, which was not attempted in this work due to time constraints. Hence only the absorption coefficient of the InGaAsSb *p-i-n* samples will be presented.

Absorption coefficient data

The room temperature absorption coefficient data of $\text{In}_x\text{Ga}_{1-x}\text{As}_y\text{Sb}_{1-y}$ *p-i-n* samples with $0.05 \leq x \leq 0.30$ is presented in figure 5.9a. As mentioned previously, due to the absorption tail of the GaSb substrate, the data above 0.65 eV is excluded from analysis.

All samples exhibit a sharp onset of absorption at the bandgap energy followed by a slow continuous increase towards higher photon energies. Likewise, the absorption increases in alloys with a narrower bandgap and a higher In fraction as expected, up to the sample with $x = 0.26$ which measured the highest absorption coefficient of 8500 cm^{-1} at $2.2 \mu\text{m}$. Interestingly, the absorption coefficient of the sample with the highest In fraction of $x = 0.30$ is slightly lower, which might indicate a beginning of a downward trend in absorption with even higher In fractions in the alloy. However, it might also be a reflection of the below-average material quality in this sample caused by a higher degree of lattice mismatch present and even more so, the presence of phase separation clearly noted in XRD data. If growth conditions were optimised for this alloy, one might observe a decrease in phase separation and a commensurate

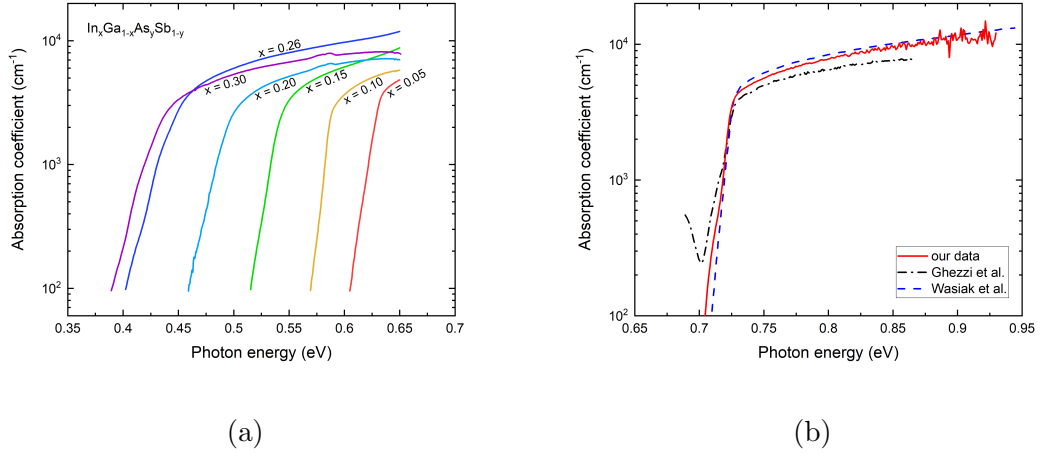


Figure 5.9: (a) Room temperature absorption coefficient of $\text{In}_x\text{Ga}_{1-x}\text{As}_y\text{Sb}_{1-y}$ samples with $0.05 \leq x \leq 0.30$ on a log-linear scale. (b) Room temperature absorption coefficient of GaSb measured in this work compared to literature.

increase in absorption.

Figure 5.9b shows the room temperature absorption coefficient data of the GaSb sample measured in this work compared to experimental data found in literature. The absorption coefficient of epitaxial GaSb increases up to $\sim 10^4 \text{ cm}^{-1}$. Our data is in excellent agreement with that of Wasiak et al.[174] who developed a more advanced model of calculating absorption of a thin film.

The slight deviation of the absorption edge from the expected straight line visible on the log-linear scale might be a result of under- or overcorrection of the interference effects in this lower energy region, or a consequence of any mismatch between the modelled phase angle and the measured one; even a slight difference between the two can cause a noticeable shift in the absorption edge. A similar deviation is seen in data from Ghezzi et al.[175] who similarly measured the absorption in GaSb with infrared spectroscopy, but did not attempt any correction of the interference effects, and data from Wasiak et al.[174], though on a much smaller scale. This deviation from a straight line might just be a reflection of the Urbach tail, i.e. broadening of the absorption edge due to alloy disorder, as described in section 2.1.1.

Figure 5.10 shows the experimental absorption coefficient data of various binary and ternary III-V alloys as well as quaternary InGaAsSb alloys grown by various techniques available in literature, alongside GaSb and InGaAsSb data measured in this work.

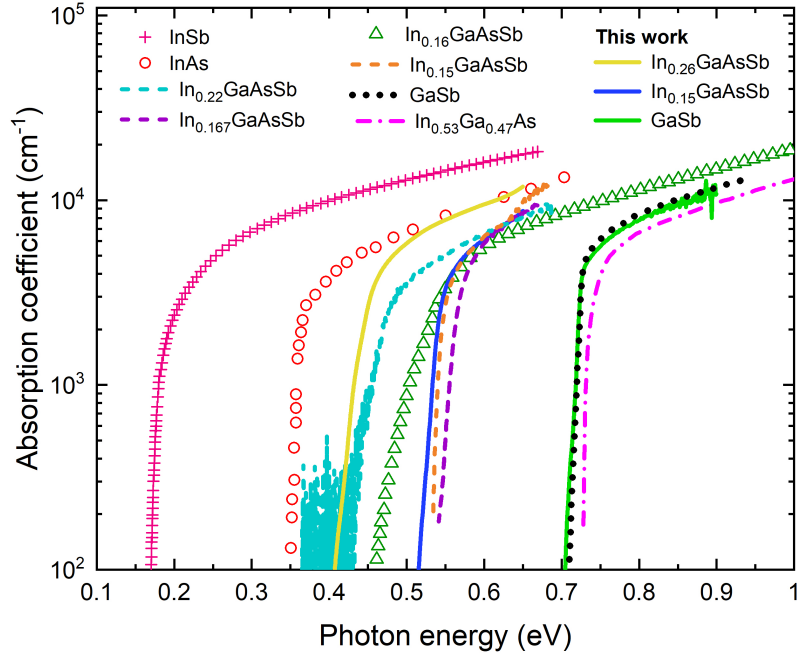


Figure 5.10: Experimental absorption coefficient data of binaries InSb[176], InAs[177], and GaSb[174], ternary In_{0.53}Ga_{0.47}As[178], and quaternary In_{0.22}GaAsSb (MBE)[99], In_{0.167}GaAsSb (LPE)[118], In_{0.16}GaAsSb (OMVPE)[42], and In_{0.15}GaAsSb (OMVPE)[124] taken from literature. In_{0.26}GaAsSb, In_{0.26}GaAsSb, and GaSb measured in this work are also shown.

The absorption coefficient measured in this work is in very good agreement with previously reported data. Some discrepancy in the cutoff energies of alloys with the same reported In fraction is notable, although this is most likely a reflection of the difficulties in determining the exact alloy composition of such quaternary alloys. Furthermore, any disorder in the alloy will lead to a broadening of the absorption

edge, making the determination of the precise cutoff energy more challenging.

5.5.2 Urbach energy

All samples exhibit an exponential dependence on energy in the region below the absorption edge, consistent with the Urbach energy relation given by equation 2.7. The experimental absorption coefficient data was fit to this equation in order to extract the value of the Urbach energy, E_U , which is indicative of the material quality. Likewise, the above bandgap absorption was fit to equation 2.6 in order to extract the value of the exponent, n . Figures 5.11a and 5.11b show the Urbach tail and absorption edge fits for the $\text{In}_x\text{Ga}_{1-x}\text{As}_y\text{Sb}_{1-y}$ and GaSb samples, respectively. The extracted Urbach energies are presented in figure 5.12a.

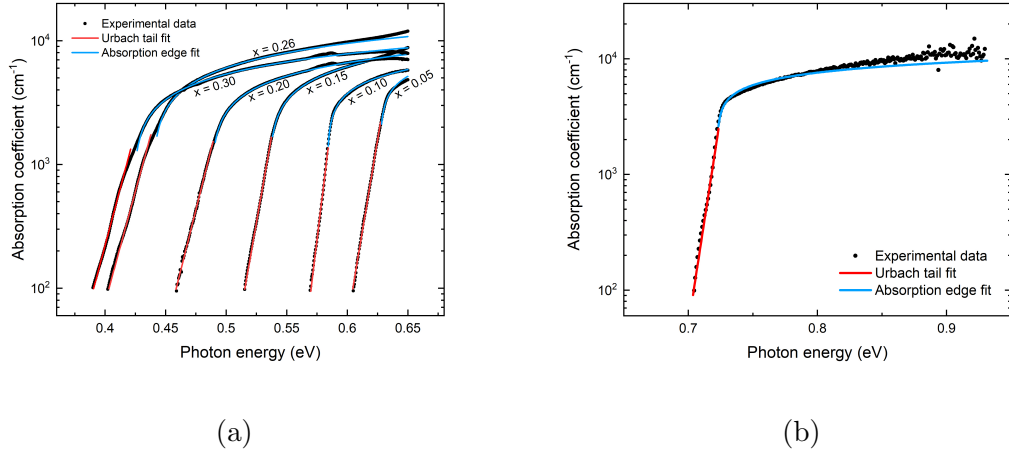


Figure 5.11: Urbach tail and absorption edge fits for (a) $\text{In}_x\text{Ga}_{1-x}\text{As}_y\text{Sb}_{1-y}$ samples with $0.05 \leq x \leq 0.30$, and (b) GaSb.

The Urbach energy of GaSb was measured to be 5 meV, similar to a previously reported value of 2.68 meV for epitaxially grown GaSb[174]. Other reports for the GaSb Urbach energy are estimated from thick GaSb substrates, and are usually in the range of 12-15 meV[49], [179]. A similar value of 12 meV was measured for a GaSb substrate in this work, suggesting that epitaxially grown GaSb is of higher crystallinity and as such exhibits lower Urbach energies.

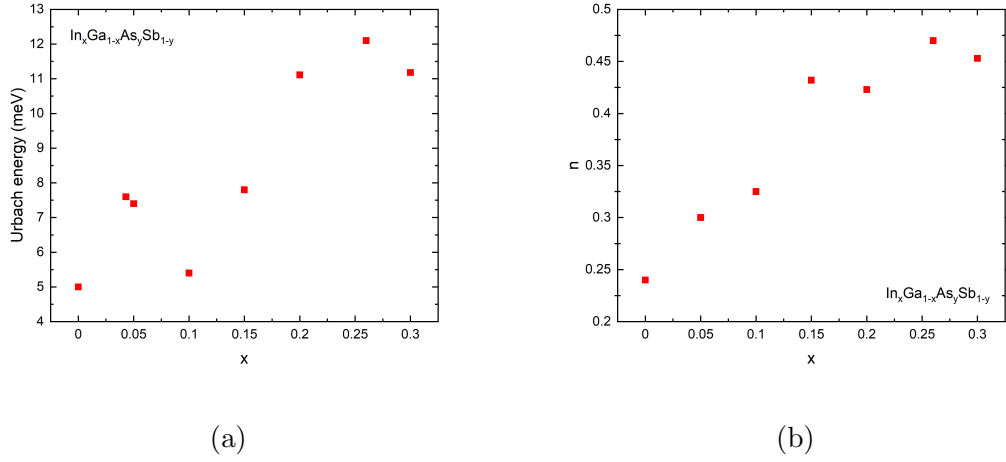


Figure 5.12: The variation of (a) Urbach energy, and (b) the exponent, n , with In fraction in the alloy.

InGaAsSb alloys with $x \leq 0.15$ similarly exhibit low Urbach energies in the range 5-8 meV, with an initial decrease towards the lowest energy of 5.4 meV measured in the sample with $x=0.10$, followed by an increase towards higher alloy fractions. The highest Urbach energy of 12.1 meV is measured in the sample with $x=0.26$, before slightly reducing to 11.18 meV in the sample with the highest In fraction of $x=0.30$. This unexpected decrease is most likely a result of the difficulty in fitting the absorption tail region with an exponential dependence for the two highest In fraction alloys. In fact, different regions of the absorption tails can be fit with different Urbach energies. This deviation from a simple exponential dependence is believed to be a direct consequence of the phase separation noted in the two samples. As the alloy decomposes into GaAs- and InSb-rich quaternary phases, so does the absorption tail decompose into regions with various gradients.

Figure 5.12b shows the variation of the exponent, n , extracted from the fit of the experimental absorption coefficient data to the expression $\alpha(h\nu) = A(h\nu - E_g)^n$. While all InGaAsSb samples can be said to have an approximately square root dependence on energy ($n \approx 1/2$) consistent with a direct gap material, the poorest fit is achieved in the GaSb sample, with a value of $\sim 1/4$. This failure to fit the

absorption coefficient of GaSb with a square root dependence on energy for $h\nu > E_g$ was already noted in literature, leading to a development of alternate models[174], [175]. InGaAsSb samples in general provide a better fit to the above expression, with a near perfect square root dependence seen in samples with $x \geq 0.15$.

5.5.3 Bandgap energy

The bandgap energy was extracted from the absorption coefficient data via several different approaches. The most common method involves linearly fitting the absorption edge on an α^2 vs $h\nu$ graph and extrapolating to $\alpha = 0$ [123], [175], [177], [179]. The bandgap energy can also be defined as the energy at which the first derivative of the absorption coefficient reaches a maximum, as this corresponds to the onset of band-to-band absorption[49]. An example of the two methods is given in figure 5.13.

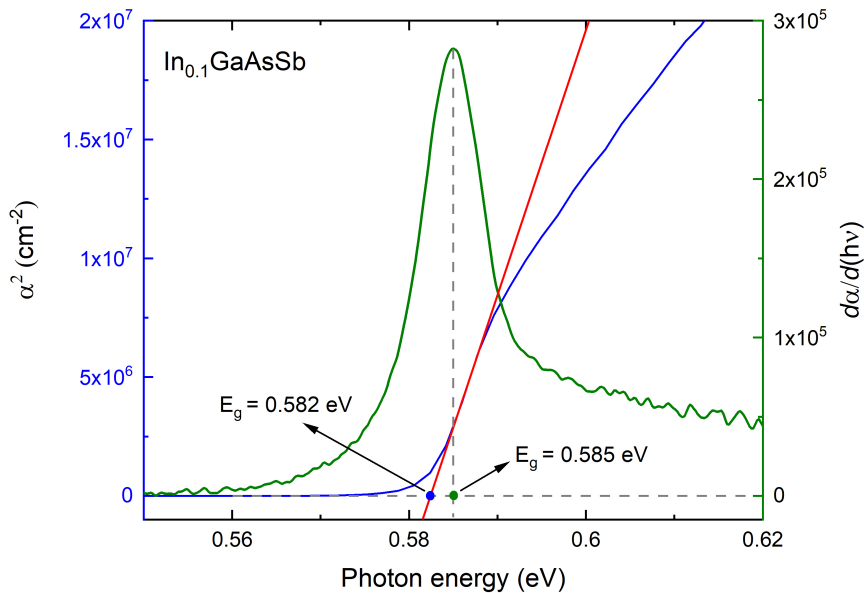


Figure 5.13: An example of the two graphical methods for extracting the bandgap energy from absorption coefficient data for the $\text{In}_{0.1}\text{GaAsSb}$ sample.

Furthermore, the bandgap energy can be extracted by fitting the expressions 2.7 and 2.6 to the experimental absorption coefficient data and finding the value of the bandgap energy, E_g , that provides the best fit. All four methods were used to ascertain the value of the bandgap energy for each sample. Figure 5.14 shows the mean value of the bandgap energy and the standard deviation as the error. On the graph are also shown the interpolation methods provided by Vurgaftman et al.[100] and Moon et al.[114]

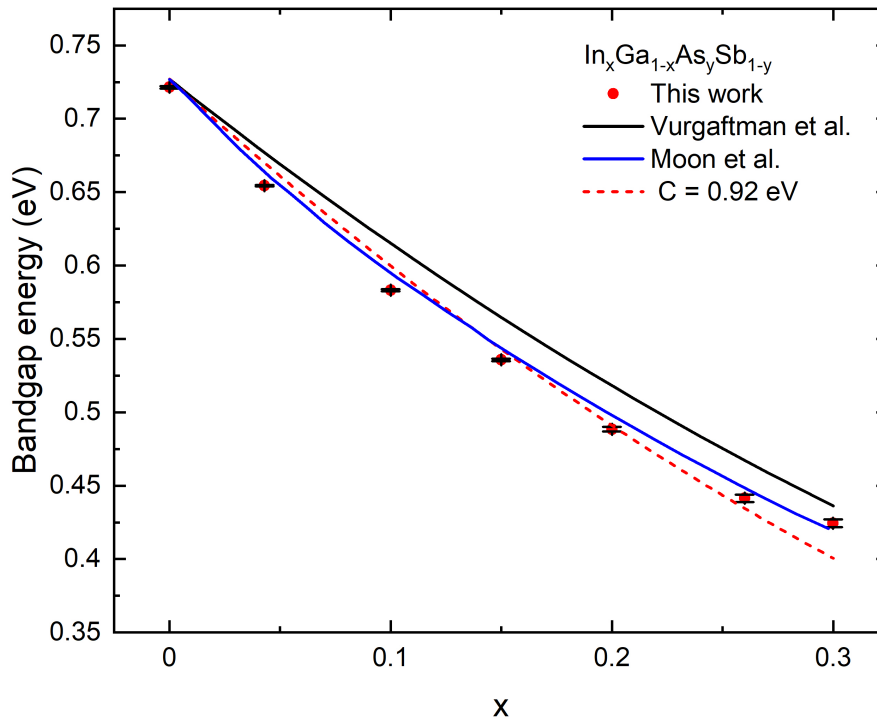


Figure 5.14: Variation of the bandgap energy with In fraction in the alloy. The two solid lines correspond to interpolation methods from Vurgaftman et al.[100] with a bowing parameter of 0.75 eV, and Moon et al.[114]. The same interpolation method from Vurgaftman applied to our data with a higher bowing parameter of 0.92 eV is represented by the dashed line.

GaSb measures a bandgap energy of 0.722 eV, which is slightly lower than typical

values reported in literature, between 0.724-0.727 eV[20], [97], [100], [118], [175], [180]. However, our value is in very good agreement with that reported by Wasiak[174], who measured a bandgap energy of 0.7228 eV. As expected, the bandgap reduces with the introduction of In and As to the alloy, with the lowest value of 0.422 eV measured in the sample with $x=0.30$. This reduction is non-linear with an observed downward bowing in agreement with previous literature. While the interpolation given by Vurgaftman (equation 3.3) is generally considered to provide the best fit to experimental data, we find that the suggested bowing parameter of 0.75 eV underestimates the bowing observed in our data. This is unsurprising since this value was obtained by averaging all of the bowing parameters reported in literature at the time, and therefore is not representative of the actual trend. One could argue that any discrepancy between the Vurgaftman interpolation and our data is a result of an uncertainty in the growth rates which would affect the compositional calibration. However, as mentioned previously, the group III growth rates are extremely stable and do not diverge by more than 5% over extended growth campaigns, which leads to a variation in the In fraction of less than 1%. Furthermore, while the presence of any lattice mismatch or phase separation also affects the bandgap energy, this was only significant in the alloys around the onset of the miscibility gap. While an improved fit to our data can be achieved by using a higher value of the bowing parameter of 0.92 eV, a superior agreement is seen with the interpolation method given by Moon. Interestingly, this method was historically found to overestimate the bowing, particularly in alloys with higher In fractions[41], [44], [97]. Nevertheless, our data shows excellent agreement with this interpolation method.

5.6 Conclusion

To summarise, several homojunction In_xGaAsSb *p-i-n* photodiodes and transmission layers with $0 \leq x \leq 0.3$ have been grown via MBE. The XRD measurements showed

well defined and narrow epilayer peaks indicating a uniform, high-quality crystal growth in $\text{In}_x\text{Ga}_{1-x}\text{As}_y\text{Sb}_{1-y}$ *p-i-n* samples with $0 < x < 0.15$. Samples with $0.15 < x < 0.3$ exhibited a general broadening of XRD peaks and even decomposition into multiple peaks despite their mismatch never exceeding 150 arcseconds. This is believed to be a result of phase separation caused by a growth temperature that was too high for alloys that approach the onset of the miscibility limit. A lower growth temperature should limit this decomposition of the alloy into GaAs- and InSb-rich phases by limiting surface restructuring.

The room temperature absorption coefficient of In_xGaAsSb *p-i-n* samples, calculated from transmission data taken with the FTIR spectrometer, increased in alloys with a narrower bandgap and a higher In fraction as expected, up to the sample with $x = 0.26$ which measured the highest absorption coefficient of 8500 cm^{-1} at $2.2 \mu\text{m}$. Additionally, all samples exhibited a sharp onset of absorption at the bandgap energy followed by a slow continuous increase towards higher photon energies. The absorption coefficient of GaSb, measured on a $5 \mu\text{m}$ thick GaSb layer epitaxially grown on a semi-insulating GaAs substrate, increased up to $\sim 10^4 \text{ cm}^{-1}$, and is in excellent agreement with previous reports[174], [175].

An exponential dependence of the absorption coefficient on photon energy was noted in all samples in the region below the absorption edge. This absorption is believed to be due to lattice disorder typically caused by impurities or alloying. The Urbach energy which represents this absorption tail was found to be 5 meV in epitaxial GaSb. A higher value of 12 meV was measured for a GaSb substrate, suggesting that epitaxially grown GaSb is of higher crystallinity. InGaAsSb alloys with $x \leq 0.15$ similarly exhibited low Urbach energies in the range 5-8 meV. Alloys with $x \geq 0.15$ measured higher Urbach energies, up to ~ 12 meV. Additionally, the absorption tails of these alloys were shown to deviate from the simple exponential dependence, most likely due to the phase separation noted in these samples.

Finally, the bandgap energy, extracted from the absorption coefficient data, was found to decrease from 0.722 eV measured in GaSb, to 0.422 eV measured in the

sample with the highest In fraction of 30%. A downward bowing of the bandgap with energy consistent with literature was also noted. Interestingly, we found that this bowing was best described the less known interpolation method provided by Moon et al.[114], rather than the widely used method given by Vurgaftman et al.[100], which was found to underestimate the bowing in our data.

Chapter 6

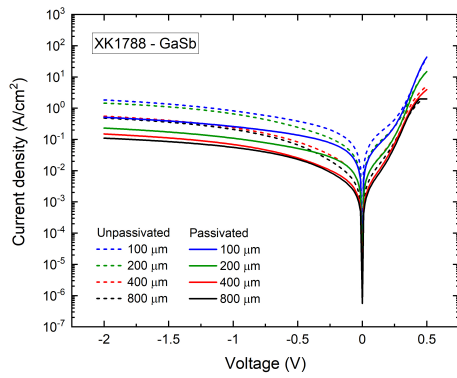
Results II

The following chapter presents the results of electrical characterisation carried out on *p-i-n* photodiodes, with a focus on leakage currents, background doping concentrations, and quantum efficiency. The detector performance is finally summarised with the calculation of specific detectivity.

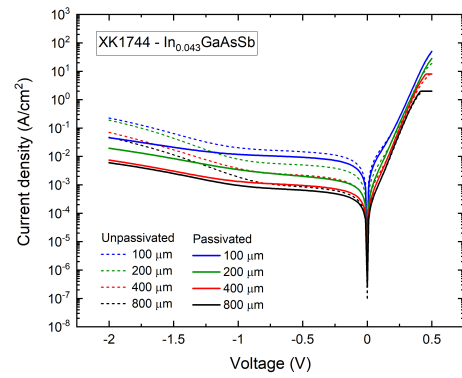
6.1 Electrical characteristics

6.1.1 Current-voltage characteristics

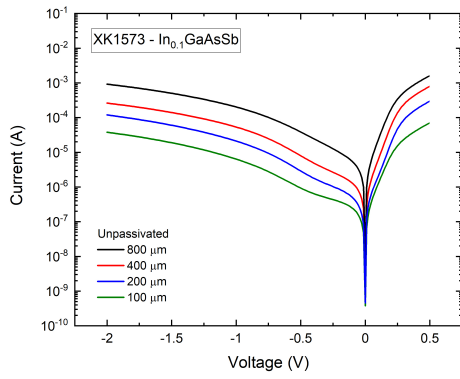
Figures 6.1a-6.1g show the room temperature voltage dependent current densities of $\text{In}_x\text{Ga}_{1-x}\text{As}_y\text{Sb}_{1-y}$ *p-i-n* photodiodes with $0 \leq x \leq 0.3$ on a log-linear scale. Measurements were performed on various device sizes with mesa diameters ranging between 100 and 800 μm . Samples with $x = 0, 0.043, 0.2,$ and 0.3 have been additionally passivated with SU-8 resist, as described in section 4.3.5. Dark current densities of both unpassivated and passivated samples are presented on the graphs. All samples exhibit the expected diode current-voltage relationship that can generally be described by an exponential increase in current with forward bias, and a much slower increase/plateauing of current with reverse bias. The passivated samples do exhibit slightly improved IV characteristics visible in both overall lower dark current density, as well as a slower increase in leakage current with reverse bias.



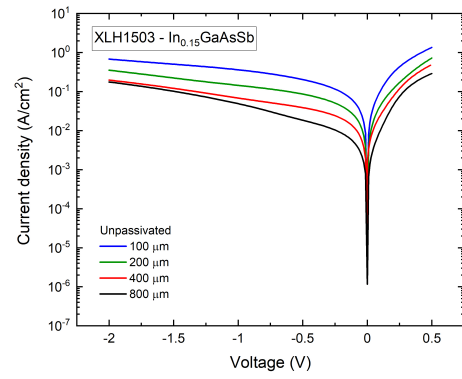
(a)



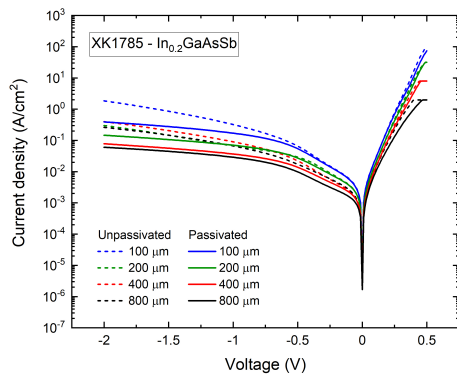
(b)



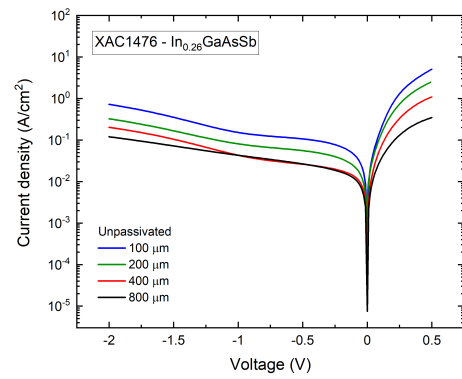
(c)



(d)



(e)



(f)

Such improvement with passivation of the mesa side walls indicates that the surface currents are an important leakage mechanism in these photodiodes.

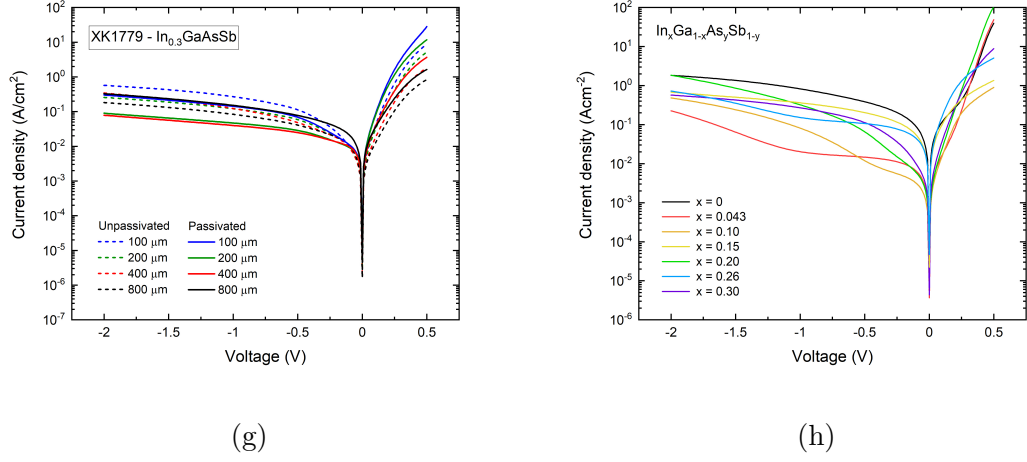


Figure 6.1: Current density against voltage for In_xGaAsSb samples with (a) $x = 0$, (b) $x = 0.043$, (c) $x = 0.1$, (d) $x = 0.15$, (e) $x = 0.20$, (f) $x = 0.26$, and (g) $x = 0.30$. (h) Current density against voltage of all unpassivated samples taken from 800 μm device mesas.

Figure 6.1h shows the room temperature voltage dependent current densities for all unpassivated samples, measured on 800 μm devices. Evidently, the dark current of all samples increases with reverse bias instead of plateauing at the reverse saturation current. This is due to either the generation of carriers within the depletion region, surface effects, or a combination of the two. Further analysis is needed to confirm the dominant leakage mechanism. Furthermore, the diode current of all samples is affected by both shunt and series resistance to a varying degree, the effects of which can be seen in forward bias at very low current levels where the shunt resistance dominates, and highest current levels where the Ohmic losses lead to a voltage drop and a slower, no longer exponential increase in current. This dependence of current on voltage in forward bias is described by the equation 2.14, where the total diode current is represented by the sum of the independent current contributions. The above expression was fit to the experimental forward IV data of 800 μm devices in order to extract the values of the reverse saturation current, ideality factor, series resistance, and shunt resistance. This was achieved by varying the above parameters

until a good fit to experimental data was reached. The tunneling current was assumed to have a negligible contribution for this voltage range and doping levels. Figure 6.2a shows an example of the forward IV fit on the sample with $x=0.15$, with the relevant regions highlighted. Note that all of the values presented henceforth were not averaged over multiple devices, but are rather extracted from the best devices measured on each sample in order to accurately present the potential of this material system.

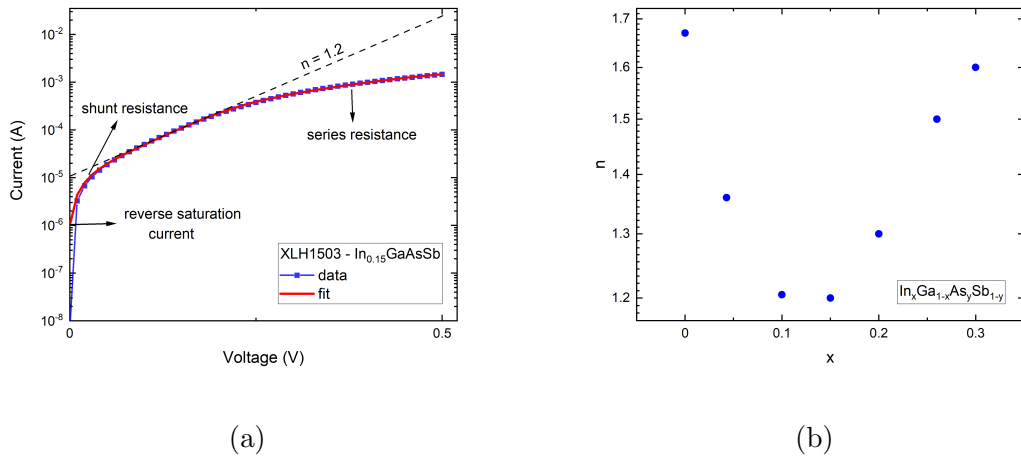


Figure 6.2: (a) An example of the IV fit in forward bias for the $\text{In}_{0.15}\text{GaAsSb}$ sample. Y-intercept corresponds to the reverse saturation current. The ideality factor is extracted from the slope of the exponential region. (b) The variation of ideality factor with indium fraction in the alloy.

Figure 6.2b shows the variation of the ideality factor with In fraction in the alloy. The GaSb photodiode fits with the highest ideality factor of 1.67, which indicates that unfavourable generation-recombination currents are dominant in the 0-0.5 V region. The ideality factor initially improves with the addition of In and As to the alloy, with the lowest value of $n \sim 1.2$ reached in samples with $x = 0.10$, and 0.15, before increasing towards even higher In fractions in the alloy. This suggests that the favourable diffusion current dominates in In_xGaAsSb photodiodes with $0 < x \leq 0.20$. The generation-recombination currents become significant once again

in photodiodes with the highest In fractions of $x = 0.26$, and 0.30 , which measure an ideality factor of 1.5 and 1.6 , respectively.

Typically, in a wider bandgap material direct band-to-band generation-recombination of carriers within the depletion region is negligible, and instead SRH generation-recombination dominates. This is believed to be the main cause of such a high ideality factor in GaSb which is known to suffer from a high native defect concentration caused by the creation of Ga_{Sb} antisites during growth[74], [80]. While low In fraction quaternaries have a similar bandgap, they measure a lower ideality factor, suggesting there are fewer defect induced trap states within the bandgap compared to GaSb. The increase in the ideality factor with higher In fractions in the alloy could be a direct result of the bandgap narrowing which would increase SRH generation-recombination, and potentially enable direct band-to-band generation-recombination. However, it might also point to an increase in defect density, particularly in the alloy with the highest In fraction of 30% which exhibited clear signs of phase separation.

Figure 6.3 shows the variation in shunt resistance with In fraction in the alloy extrapolated from the forward IV fit. Shunt resistance initially increased significantly from $2.2 \text{ k}\Omega$ in GaSb to $40 \text{ k}\Omega$ in $\text{In}_{0.043}\text{GaAsSb}$, before gradually reducing down to $2.5 \text{ k}\Omega$ in $\text{In}_{0.30}\text{GaAsSb}$. Prineas et al.[69] similarly measured $45 \text{ k}\Omega$ in an $\text{In}_{0.20}\text{GaAsSb}$ p - n diode.

The higher the surface leakage the lower the shunt resistance, as more current is allowed to flow via the additional conduction paths while bypassing the bulk junction. Unsurprisingly, GaSb measured one of the lowest shunt resistances due to the high density of surface states. It has been shown that the GaSb surface is extremely reactive such that exposure to air results in the spontaneous creation of metallic Sb which contaminates the mesa sidewalls and leads to ohmic leakage by creating additional conduction paths parallel to the surface according to equations 3.1 and 3.2[69], [89], [90]. This process is believed to be taking place in other Sb-based detectors including InGaAsSb. If that is the case, one would expect a

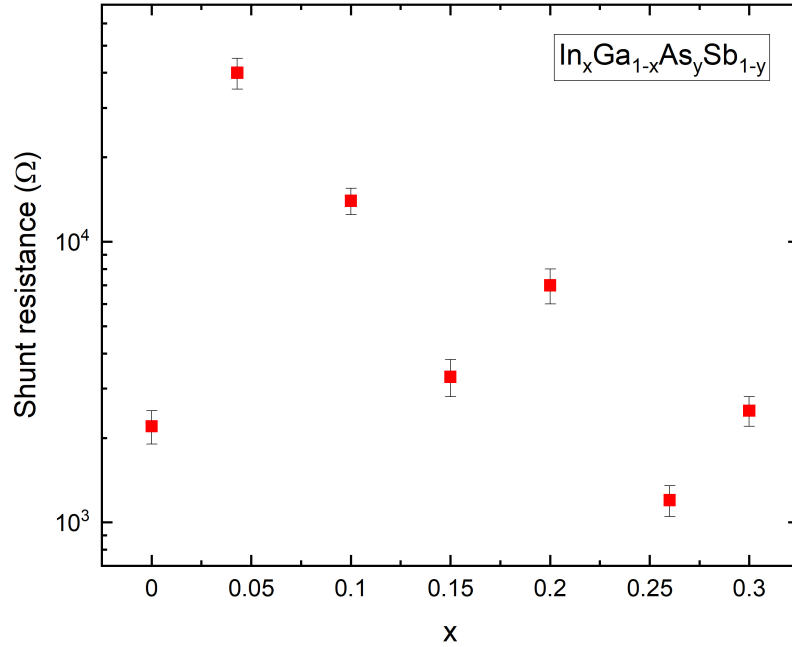


Figure 6.3: Shunt resistance variation with In fraction.

decrease in surface leakage and a commensurate increase in shunt resistance with increasing In fractions in the alloy as we move away from the GaSb-like surface (higher In and As fractions require less Ga and Sb, this would translate to less GaSb on the surface as well). Interestingly, the lowest surface leakage was noted in the sample with the lowest In fraction of 4.3%, while increasing In fractions resulted in a continuous increase in surface leakage. This would indicate that other surface leakage mechanisms are present in the InGaAsSb alloy. Indeed, others have noted that the dominant leakage mechanism is in fact generation-recombination at the surface[31] rather than ohmic leakage caused by a build-up of oxides. However, it was noted by Prineas et al.[69] that while the freshly etched InGaAsSb photodiodes were limited by surface generation-recombination currents, over time ohmic leakage becomes dominant due to a build-up of oxides at the mesa sidewalls. Note that the samples presented in this work were grown, fabricated, and characterised over

several different campaigns of varying durations. This might have influenced the observed trend since the time between each of the phases also varied across different campaigns.

On the other hand, not all samples could be fit with series resistance in forward bias, indicating that either this resistance is non-ohmic, or some other processes are taking place. A more advanced current model needs to be employed to identify dominant mechanisms under forward bias. All samples employ top p -GaSb and bottom n -GaSb contact layers. Although n -GaSb is known to be a poor contact, the back surface of the sample is used as a common contact to maximise its area and mitigate this potential issue. GaSb and $\text{In}_{0.043}$ measured a very low ohmic series resistance of 7 and 5 Ω , respectively, while $\text{In}_{0.15}\text{GaAsSb}$ measured a much higher ohmic series resistance of 190 Ω . Evidently, it is possible to create good ohmic contacts with the InGaAsSb alloy system, however, repeatability was not achieved with the current processing flow.

Figure 6.4 shows the compositional variation of the measured current density at -100 mV, and the reverse saturation current density extracted from the forward IV fit. The latter gives an indication of the bulk-limited leakage excluding surface effects. The measured current density initially reduced significantly, from 7.03 mA/cm² measured in GaSb, to the lowest value of 0.36 mA/cm² measured in In_xGaAsSb with the lowest In fraction of 0.043. This initial reduction was followed by a gradual increase towards higher In fractions, up to ~ 11 mA/cm² measured in samples with $x = 0.26$, and 0.3. While the reverse saturation current density extrapolated from the forward IV fit follows a similar trend, it is 10-30 times lower than the measured current density, which agrees with the suggestion that surface effects have an important role in overall leakage.

In addition to high surface leakage, the aforementioned high native defect concentration noted in GaSb also leads to its high bulk leakage. While the improvement in the overall dark current density of InGaAsSb compared to GaSb could be attributed to its lower surface leakage, it is possible that introducing In and As to the

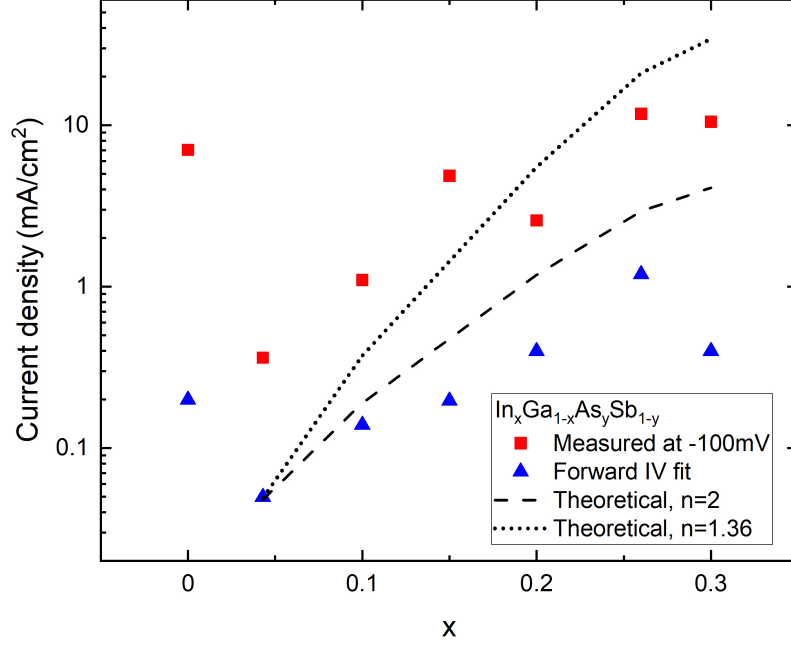


Figure 6.4: The variation of measured and fitted current density with In fraction in the alloy. The dashed and dotted lines indicate the theoretical bandgap dependence of current density, relative to the 4.3% indium sample assuming $n = 2$ and 1.36, respectively.

alloy has a positive effect on the native defect concentration, i.e. it is reduced, which would explain the initially much lower measured current density, and the noted improvement in the ideality factor. While the current density does increase with increasing In fractions in the alloy, the commensurate bandgap reduction will naturally lead to a higher bulk leakage current. The expected increase in current density as a result of the bandgap reduction alone in the SRH-limited case can be estimated through the equation[181], [182]:

$$J_0 = A \exp(-E_g/nkT) \quad (6.1)$$

where A is a constant obtained from fitting the above equation to experimental data.

This dependence of reverse saturation current density on the bandgap is indicated by the dashed and dotted lines relative to the 4.3% In sample, assuming $n = 2$ and 1.36, respectively. Evidently, the noted increase in dark current density is indeed primarily a result of the bandgap narrowing. Typical current density values for bulk InGaAsSb photodetectors reported in the literature range approximately from 0.3 to 250 mA/cm². The values reported in this work are amongst the lowest. However, given the significance of surface effects, we can't have full confidence they represent the bulk limit for this alloy.

As mentioned previously, dark current flowing through a reverse biased photodiode can be described by equation 2.15 as a sum of bulk and surface leakage currents, where the total leakage current density is expected to increase with increasing P/A ratio if the device is limited by surface currents. In order to identify the dominant leakage current component in our photodiodes it is necessary to investigate the change in the dark current density with increasing or decreasing device dimensions. Figure 6.5a shows the variation in current density measured at -100 mV with P/A ratio for all unpassivated samples.

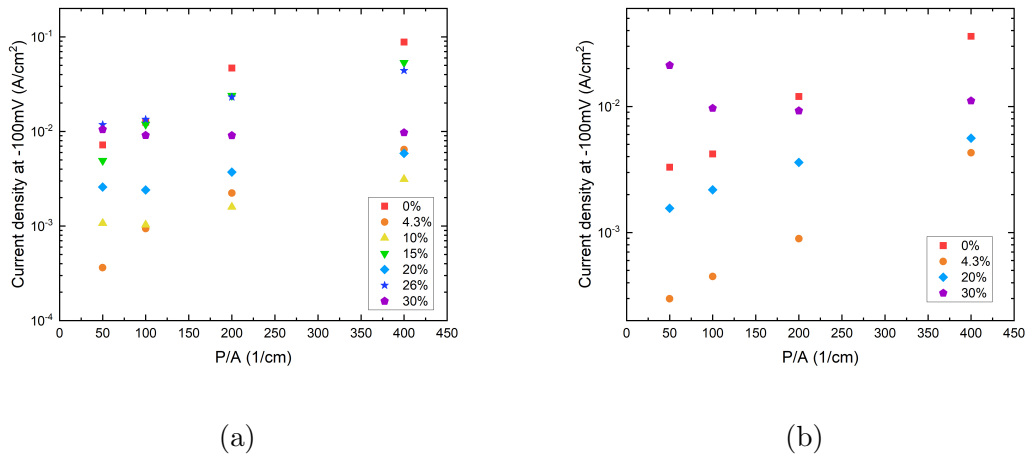


Figure 6.5: Measured current density at -100 mV against P/A ratio for (a) unpassivated, and (b) SU-8 passivated samples.

Current density was found to increase with decreasing device dimensions in all but

one sample, which confirms that surface currents are indeed the dominant source of leakage in our InGaAsSb photodiodes. This is in agreement with previous reports on leakage mechanisms in InGaAsSb photodiodes. Bhagwat et al.[31] similarly observed an increase in leakage current density with P/A ratio in In_{0.13}GaAsSb photodiodes, while Prineas et al.[69] attributed this surface leakage to generation-recombination at the exposed mesa sidewalls.

The leakage current density increases with P/A ratio even in the passivated samples, though to a lesser degree as can be seen from the graph in figure 6.5b, suggesting that surface currents are still the dominant leakage mechanism and further development of passivation/encapsulation is needed to minimise their influence. While the sample with the highest In fraction of 30% does not show a clear trend in current density with P/A ratio, this is believed to be due to the aforementioned poor material homogeneity caused by the phase separation noted in this sample. In this case, bulk currents caused by the material defects are comparable to surface currents.

Similarly, the inverse dynamic resistance-area product ($1/R_dA$) is expected to increase with decreasing device dimensions in samples dominated by surface currents[31], [69] according to equation 2.16. Figure 6.6a shows the variation of the dynamic resistance area product with In fraction at 0 and -100 mV for 800 μm devices.

A familiar trend can be seen, in which GaSb measures a very low dynamic resistance area product at both 0 and -100 mV, of 13 and 14 Ωcm^2 , respectively. A significant improvement is seen in InGaAsSb samples with low In fractions, with the highest R_dA of 194 and 416 Ωcm^2 measured in the 4.3% In sample at 0 and -100 mV, respectively. The R_dA product gradually decreases with increasing In fractions, down to $\sim 10 \Omega\text{cm}^2$ measured in samples with 26 and 30% In. This is the expected trend since the dynamic resistance is defined by leakage and as such mirrors the trend seen in dark current density. Typical R_0A values reported in literature for InGaAsSb-based photodetectors are between 1 and 150 Ωcm^2 [61], [69], [88],

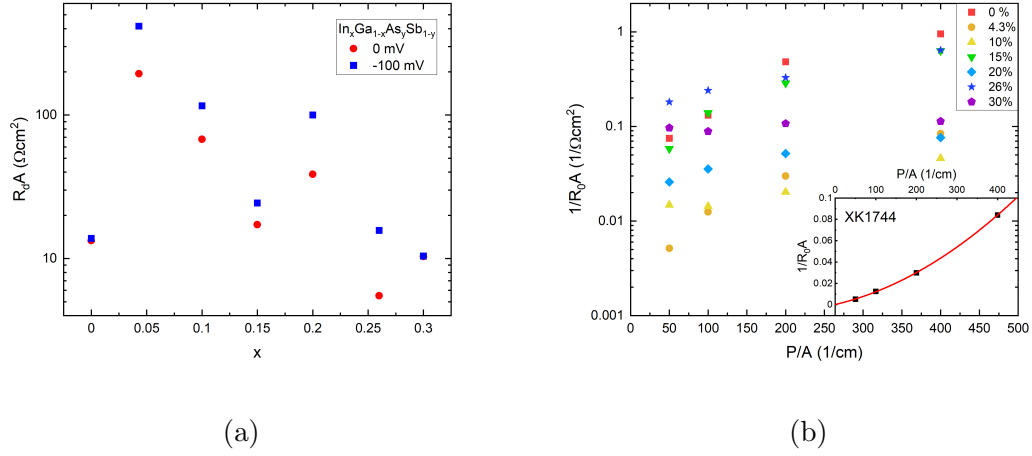


Figure 6.6: (a) Variation in the dynamic resistance area product with In fraction. (b) $1/R_d A$ product against P/A ratio for In_xGaAsSb samples with $0 \leq x \leq 0.30$.

[130], [134], [139], [140], with one of the highest values of $260 \Omega\text{cm}^2$ measured in a passivated $\text{In}_{0.18}\text{GaAsSb}$ p - i - n photodiode[135].

More importantly, the $1/R_d A$ product increases with increasing P/A ratio in all but the 30% In sample, as evident from the graph in figure 6.6b, further supporting the fact that surface currents are indeed the dominant source of leakage in the InGaAsSb photodiodes. The quadratic dependence of $1/R_d A$ on P/A ratio predicted by equations 2.16 and 2.17 for a surface dominated device can be seen in the sample with the lowest In fraction of 4.3%, as evident from the inset in figure 6.6b. The upper limit of the dynamic resistance at 0 V extrapolated from the x-axis intercept at $P/A = 0$ is 6098Ω . However, the majority of samples cannot be satisfactorily fit with a quadratic dependence. This is most likely due to the variation in surface leakage between different devices of the same size making it difficult to ascertain a particular trend. The 4.3% In sample exhibits the most consistent performance across different devices allowing us to extrapolate from the quadratic dependence.

Figure 6.7 shows the voltage dependent leakage current densities measured in our GaSb and InGaAsSb photodiodes with In fractions of 4.3, 10, and 20%, compared to a commercially available extended InGaAs photodetector with a cutoff wavelength

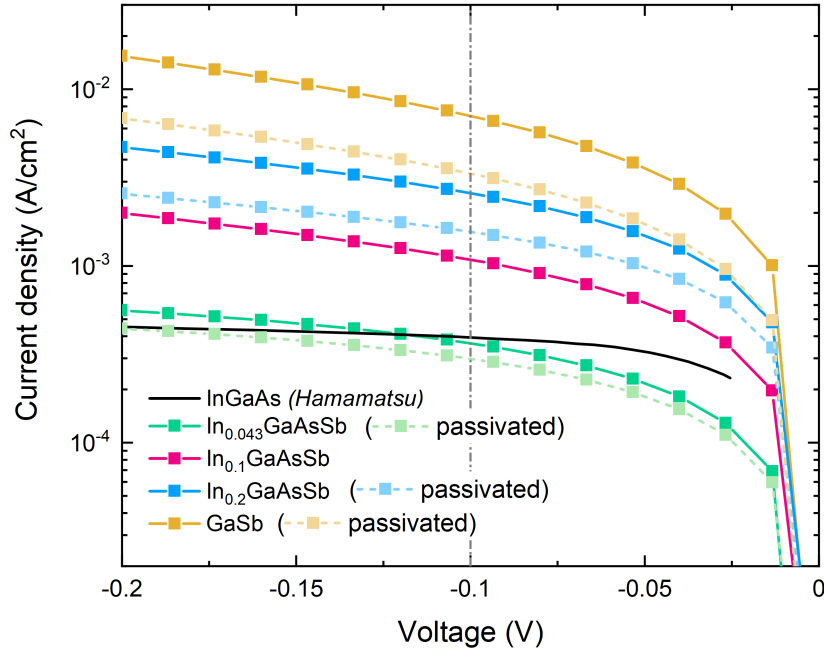


Figure 6.7: Reverse current density against voltage measured in $\text{In}_x\text{Ga}_{1-x}\text{As}_y\text{Sb}_{1-y}$ photodiodes with $x = 0, 0.043, 0.1,$ and 0.2 , compared to an extended InGaAs detector from Hamamatsu[183].

similar to our 20% device of $2.6 \mu\text{m}$ [183]. The unpassivated InGaAsSb photodiode with the lowest In fraction of 4.3% measures a current density of 0.36 mA/cm^2 at -100 mV , comparable to the extended InGaAs detector which measures a current density of 0.4 mA/cm^2 . Although the photodiodes with higher In fractions in the alloy measure higher leakage current densities, they are far from the optimisation level reached in the InGaAs detector. Moreover, Dashiell et al.[23] reported an order of magnitude lower dark current density of 0.052 mA/cm^2 in an InGaAsSb TPV with a cutoff wavelength of $2.5 \mu\text{m}$, highlighting the potential of InGaAsSb-based photodiodes to outperform extended-InGaAs detectors in the e-SWIR range.

In conclusion, our findings agree with the pre-existing reports on leakage mechanisms in InGaAsSb photodiodes, which identify surface currents as the leading

source of leakage in such devices. We have found this to be the case across all $p-i-n$ samples with In fractions between 0 and 30%. Hence the prevalence of surface currents appear to be independent of the In fraction in the alloy. Therefore, development of passivation technologies is key in optimising device performance and approaching the true bulk-limited case.

6.1.2 Unintentional intrinsic doping

Although the intrinsic InGaAsSb region is nominally undoped, the presence of unintentional dopants was confirmed through CV measurements. The background doping levels are caused by either impurities unintentionally introduced during growth, or native defects that stem from growth dynamics. In either case, the doping concentration will define how quickly the junction depletes with reverse bias. Higher doping levels in the intrinsic region require higher reverse voltages to deplete the junction of charges. Thus by measuring the capacitance in the diodes under reverse bias one can obtain information about the doping levels in the absorbing region.

The exact unintentional doping concentration of the intrinsic region was extracted by fitting the experimental CV data to a depletion model described in section 4.4.5. The doping levels of the p , i , and n regions were varied until a good fit to experimental data was achieved. Figure 6.8 shows the variation of the unintentional intrinsic doping concentration with In fraction in the alloy, extracted from the fit. The inset in the figure shows an example of the CV fit for the sample with 30% In.

GaSb measured the highest background doping concentration of $2.7 \times 10^{15} \text{ cm}^{-3}$, which is significantly lower than typical unintentional doping levels reported in GaSb, usually between $10^{16} - 10^{17} \text{ cm}^{-3}$. It is well-established that such a high (always p -type) background doping concentration found in GaSb stems from Ga_{Sb} antisites, which are native defects introduced during growth[20], [46], [76]. This is most likely caused by the poor surface mobility of Sb atoms which tend to aggregate

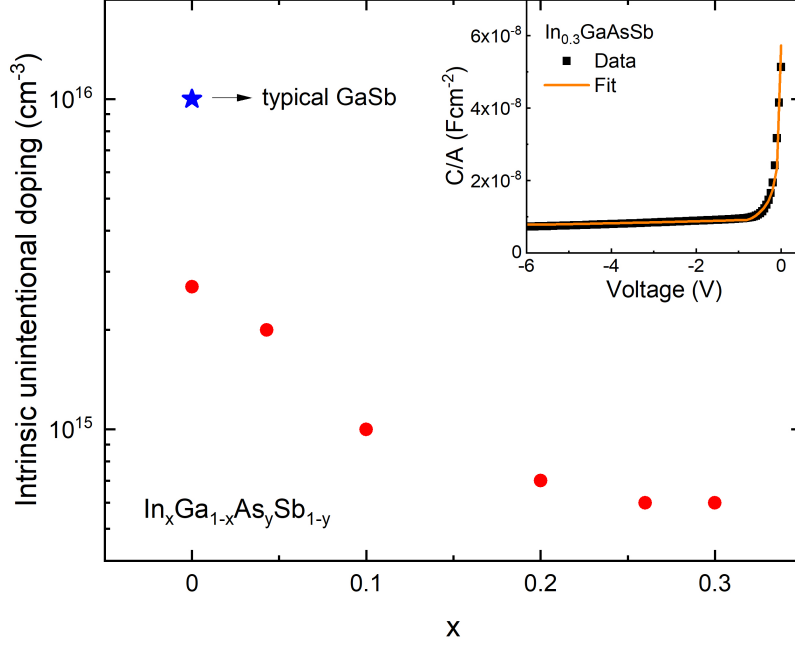


Figure 6.8: The intrinsic unintentional doping concentration as a function of In fraction in the alloy for $\text{In}_x\text{Ga}_{1-x}\text{As}_y\text{Sb}_{1-y}$ layers with $0 \leq x \leq 0.30$. Note that the sample with $x = 0.15$ could not be satisfactory fit and is not presented on the graph. The inset shows an example of the CV fit for the sample with $x = 0.30$.

together during growth leading to Sb vacancies, which are then easily occupied by Ga atoms[81]. We believe that the much lower residual doping concentration measured in this work is a direct result of a careful moderation of excess Sb flux, which has been reported to play an important role in GaSb growth dynamics[75]. Despite some conflicting reports on the influence of the V/III ratio on the native defect density in GaSb (refer to section 3.1), recent investigation carried out by our research group did in fact conclude that a reduced V/III growth rate ratio gives the best material quality, i.e the lowest native defect concentration[184].

Interestingly, the addition of In and As to the alloy significantly reduced the background doping concentration. It initially dropped to $1 \times 10^{15} \text{ cm}^{-3}$ measured in

$\text{In}_{0.1}\text{GaAsSb}$, followed by a more gradual reduction to $6 \times 10^{14} \text{ cm}^{-3}$ measured in both $\text{In}_{0.26}\text{GaAsSb}$ and $\text{In}_{0.30}\text{GaAsSb}$ where the doping plateaued. There is insufficient evidence to conclude that the native defect responsible for p -type conductivity in GaSb is the same defect that causes a p -type background in InGaAsSb, and that the introduction of In and As to the alloy has reduced or eliminated this defect. However, if the main culprit for the creation of the dominant Ga_{Sb} antisite defects in GaSb is indeed the clustering of Sb atoms at the growing surface, it is likely that this remains an issue in InGaAsSb as well, particularly in the dilute alloys which are predominantly GaSb-like. Furthermore, InGaAsSb requires lower growth temperatures than GaSb which might reduce the tendency of Sb atoms to cluster together at the surface. Likewise, growing InGaAsSb layers with increasing As fractions requires a reduction of the Sb flux in order to maintain the same overall V/III ratio, which might also lead to a reduction in background doping. Additionally, the introduction of In and As to the alloy most likely changed the adatom surface dynamics leading to the formation of other complex defects which could give rise to a compensatory unintentional n -type doping. Given the improvement in current-voltage characteristics with the addition of In/As to the alloy seen in both the reduction of leakage currents and an improvement in the ideality factor, we conclude that the most likely explanation is a reduction of the native defect. This decrease in background doping of InGaAsSb with increasing In fractions was also noted by Lazzari et al.[46] in MBE-grown In_xGaAsSb layers with $x = 0, 0.15, \text{ and } 0.20$. The authors similarly attributed this reduction to the disappearance of the native defect found in GaSb.

Although the dopant type could not be inferred through CV measurements alone, numerous reports[43], [44], [46], [61], [88], [99], [128], [133]–[135], [137] on the background doping in InGaAsSb suggest it is p -type for alloy compositions with In fractions between 15 and 30%. However, Rakovics et al.[118] observed a change in the dopant type from n to p in In_xGaAsSb layers with $x > 0.10$. Likewise, typical doping concentrations measured in nominally undoped InGaAsSb layers are

between $1 \times 10^{15} - 5 \times 10^{16} \text{ cm}^{-3}$ [43], [44], [46], [61], [88], [99], [128], [133]–[135], [137] - much higher than those reported in this work. Evidently, the lower background doping concentration achieved in our epitaxial GaSb layers was carried through into InGaAsSb due to a careful moderation of V/III growth rate ratios.

6.1.3 Quantum efficiency

Figure 6.9a shows the room temperature voltage dependent external quantum efficiency of GaSb and InGaAsSb photodiodes at $1.55 \mu\text{m}$, calculated through equation 2.26 from the measured current-voltage data. Figure 6.9b shows an IV example under dark and light conditions for an InGaAsSb diode with 4.3% In.

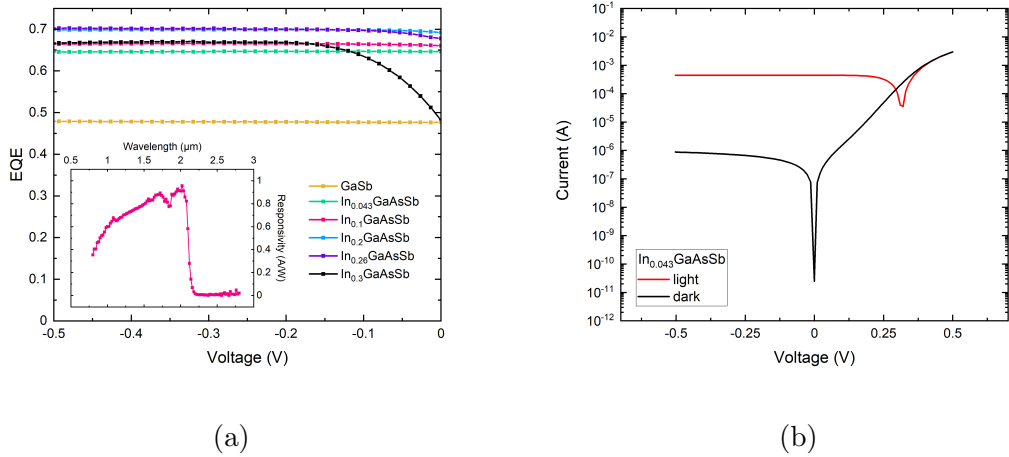


Figure 6.9: (a) Current flowing through a biased In_{0.043}GaAsSb photodiode under dark and light conditions. (b) External quantum efficiency against voltage for In_xGa_{1-x}As_ySb_{1-y} photodiodes with $0 \leq x \leq 0.30$. The inset shows an example of the responsivity spectrum at zero bias for the sample with 4.3% In.

As expected, GaSb measured the lowest quantum efficiency of 48%, while the InGaAsSb photodiode with the lowest In fraction of 4.3% measured a significantly higher quantum efficiency of 65%. The quantum efficiency continued to increase with increasing In fractions in the alloy, up to a maximum value of $\sim 70\%$ measured in samples with 20 and 26% In, which is consistent with the measured increase in

absorption coefficient in alloys with higher In fractions. Assuming 30% reflection losses at the surface, these photodiodes have reached the theoretical limit for internal quantum efficiency. The sample with the highest In fraction of 30% measured a lower quantum efficiency of 67% which was only reached at a voltage of ~ -200 mV. At zero bias, this sample measured an EQE similar to the GaSb photodiode of only 48%. The lower quantum efficiency is consistent with the lower absorption coefficient measured in this sample. The quantum efficiency values reported in this work are within the range of values typically reported for MBE-grown InGaAsSb photodetectors with $0.10 \leq x \leq 0.30$, between 60 and 70% [44], [131], [132], [139].

The responsivity of InGaAsSb devices was calculated from the measured quantum efficiency through equation 2.27, and was found to be between 0.81 A/W and 0.87 A/W at $1.55 \mu\text{m}$ and zero bias in samples with an In fraction of less than 30%. Since responsivity is higher at wavelengths closer to the absorption edge, as can be seen from the inset in figure 6.9a which shows the wavelength-dependent responsivity of the $\text{In}_{0.043}\text{GaAsSb}$ photodiode, one can expect an increase in responsivity to ~ 1 A/W at $\sim 2\mu\text{m}$.

Moreover, the quantum efficiency is independent of reverse bias in all but the samples with the highest In fractions of 26 and 30%. This suggests that the minority carrier diffusion length is greater than the active layer thickness ($L_p > 1 \mu\text{m}$). This is in agreement with previous reports on the minority carrier diffusion length in InGaAsSb-based photodetectors which was found to be between 10 and $12 \mu\text{m}$ [22], [69], [125], [131]. Despite the mesa diameters exceeding the minority carrier diffusion length, this is unlikely to prevent the collection of photogenerated carriers by the external contacts. Collection of carriers is limited by the voltage drop required to move charges from the centre of the big mesas to the contact within the p -type cladding. This can become an issue if the light source is too focused or bright, but steps were taken to ensure this limit is never reached.

The bias dependence seen in $\text{In}_{0.30}\text{GaAsSb}$ is consistent with lower minority carrier diffusion lengths most likely caused by a higher density of defects present in this

alloy due to the aforementioned phase separation. Although the sample with 26% In also exhibited a bias dependence, the quantum efficiency increased by only 2% from zero bias to ~ -80 mV.

6.1.4 Specific detectivity

As the ultimate figure of merit that defines photodetector signal-to-noise performance, room temperature specific detectivity was calculated through equation 2.28 from the dark current, R_0A , and responsivity data at $1.55 \mu\text{m}$. Figure 6.10a shows the voltage dependence of specific detectivity for $\text{In}_x\text{Ga}_{1-x}\text{As}_y\text{Sb}_{1-y}$ photodiodes with $0 \leq x \leq 0.30$.

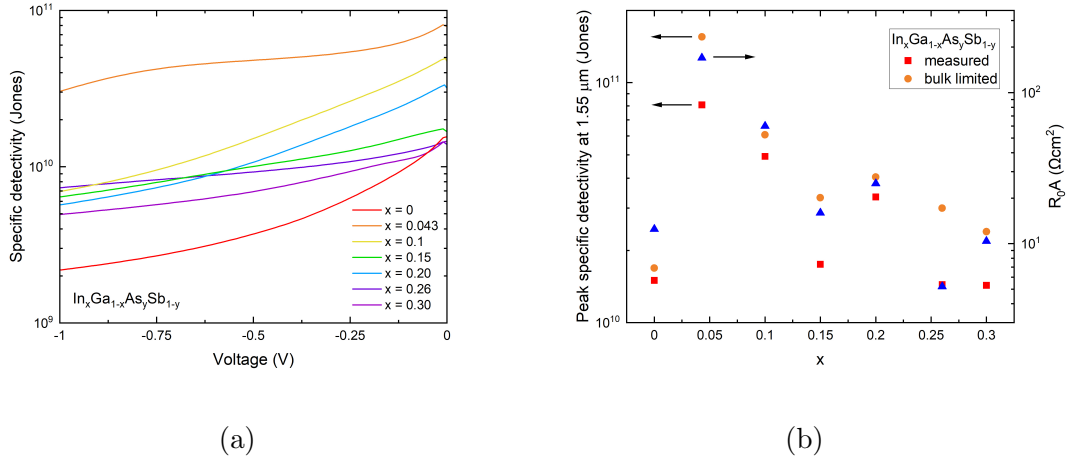


Figure 6.10: (a) Specific detectivity against voltage at $1.55 \mu\text{m}$ for GaSb and InGaAsSb photodiodes. (b) Measured and bulk limited peak specific detectivities and R_0A product as a function of In fraction in the alloy.

The peak specific detectivity extracted from this data is presented in figure 6.10b against In fraction in the alloy. To demonstrate the potential of the InGaAsSb alloy system, the specific detectivity was also calculated with the reverse saturation current density extrapolated from forward bias as the upper limit of what could be achieved in devices that are bulk rather than surface limited. The zero-bias dynamic resistance-area product is also presented on the graph. GaSb measured one of the

lowest peak specific detectivities of 1.53×10^{10} Jones at -10 mV. The highest peak specific detectivity of 8.08×10^{10} Jones was measured in the sample with the lowest In fraction of 4.3% at -10 mV, which is five times higher than the detectivity measured in GaSb. The peak specific detectivity then gradually reduced with increasing In fractions in the alloy, down to the lowest value of 1.43×10^{10} Jones measured in $\text{In}_{0.30}\text{GaAsSb}$ at -10mV. Since responsivity increases with wavelength according to equation 2.27, a commensurate improvement in specific detectivity is expected at longer wavelengths closer to the photodiodes' cut-offs. Such improvement can be seen from the graph in figure 6.11, where the specific detectivity increased from 3.7×10^{10} Jones at $1.55 \mu\text{m}$ to 4.3×10^{10} Jones at $2.02 \mu\text{m}$ in our $\text{In}_{0.10}\text{GaAsSb}$ *p-i-n* photodiode.

The specific detectivity of all samples peaks at around zero bias before gradually decreasing with higher voltages, indicating that it is dominated by leakage currents which increase with increasing bias. Therefore, despite the improvement in both the absorption coefficient and responsivity of the photodiodes with increasing In fraction in the alloy, the specific detectivity decreases due to the worsening of the leakage current. The specific detectivity calculated from the extrapolated reverse saturation current density is up to two times higher than the measured one, with the highest value of 1.55×10^{11} Jones projected for the sample with the lowest In fraction of 4.3%, confirming there is still room for improvement through the minimisation of surface leakage.

Typical specific detectivity values reported for InGaAsSb-based photodetectors are between 3×10^9 and 9×10^{10} Jones[22], [44], [61], [69], [88], [131], [132], [135], [139], with one of the highest values of 9.4×10^{10} Jones measured in an $\text{In}_{0.14}\text{GaAsSb}$ pBn photodetector[140]. Furthermore, the non-optimised photodiodes reported in this work measure a specific detectivity comparable to commercially available extended InGaAs photodetectors with a $2.6 \mu\text{m}$ cutoff ($\sim 6 \times 10^{10}$ Jones)[185].

Figure 6.11 shows the measured wavelength dependent specific detectivity of our $\text{In}_{0.10}\text{GaAsSb}$ *p-i-n* photodiode calculated from its zero-bias spectral responsivity,

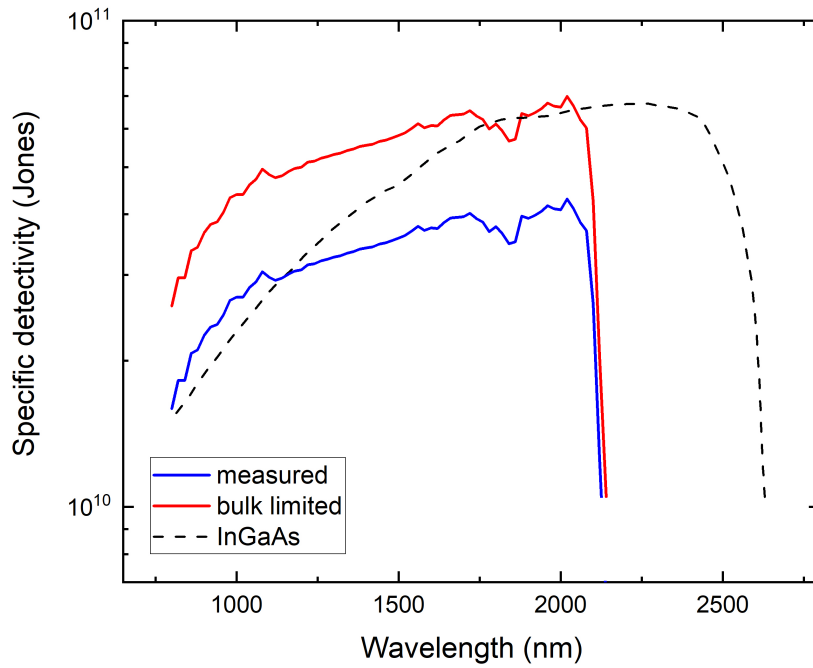


Figure 6.11: Measured and bulk limited wavelength dependant specific detectivities of our $\text{In}_{0.1}\text{GaAsSb}$ $p-i-n$ photodiode compared to a commercially available InGaAs photodetector with a $2.6 \mu\text{m}$ cutoff[185].

and the extrapolated specific detectivity assuming a bulk limited device. The specific detectivity of Teledyne's extended InGaAs photodetector[185] is also shown on the graph for comparison.

Chapter 7

Conclusions and Future Work

7.1 Conclusions

The aim of this work was to investigate the quaternary InGaAsSb alloy as a promising material system for applications in the SWIR spectral region across a wide In fraction range from 4.3% to 30% in a single study. The main focus of this work is the compositional variation of various material and InGaAsSb-based device properties, with particular attention given to dilute alloys which are seldom investigated in literature.

MBE growth of $\text{In}_x\text{Ga}_{1-x}\text{As}_y\text{Sb}_{1-y}$ photodiodes with $0 \leq x \leq 0.30$ lattice matched to GaSb substrates was discussed in chapter 5. A detailed analysis of the XRD spectra revealed epitaxial layers of good crystalline quality in samples with $x < 0.15$. The samples exhibited well-lattice matched and narrow epilayer peaks indicating good material uniformity. Growth of samples with $x > 0.15$ proved more challenging. XRD spectra showed a general broadening of epilayer peaks and, in some cases, even a decomposition into multiple peaks which is indicative of phase separation, i.e. the alloy forming with GaAs- and InSb-rich quaternary regions. Optimising growth conditions for InGaAsSb layers with high In fractions, i.e. employing lower growth temperatures, would likely result in suppressed phase separation and successful growth of such alloys. Various optical

properties of the InGaAsSb alloy were also investigated in this chapter. The absorption coefficient of InGaAsSb layers was extracted from the FTIR transmission data. All samples measured a relatively high absorption coefficient comparable to other III-V semiconductor alloys with bandgaps in the e-SWIR spectral region. Moreover, the absorption coefficient increased with increasing In fractions in the alloy, up to 8500 cm^{-1} measured in the sample with 26% In at $2.2 \mu\text{m}$. The sample with the highest In fraction of 30% measured a slightly lower absorption coefficient which might either mark a beginning of a downward trend with even higher In fractions in the alloy, or it might be a direct result of the phase separation noted in this alloy. Moreover, Urbach energies between 5 and 12 meV were extracted from the absorption data for GaSb and InGaAsSb layers, where one can note an increase in Urbach energy with increasing In fractions in the alloy, consistent with the broadening of the XRD spectra. The bandgap energies extracted from the absorption data exhibit the expected reduction from 0.722 eV measured in GaSb to 0.422 eV measured in $\text{In}_{0.30}\text{GaAsSb}$. Interestingly, the downward bowing of the bandgap fits better with the less common model proposed by Moon et al.[114], than the much more widely used model proposed by Vurgaftman et al.[100], which was found to underestimate the bowing observed in the experiment.

The compositional variation of various electrical properties of InGaAsSb-based photodiodes were presented in chapter 6. Both the dark current density and the dynamic resistance-area product initially improved significantly in dilute alloy InGaAsSb diodes compared to the GaSb one. Dark current density reduced from 7.03 mA/cm^2 in GaSb to 0.36 mA/cm^2 in $\text{In}_{0.043}\text{GaAsSb}$ at -100 mV, while the R_0A product increased from $13 \Omega\text{cm}^2$ in GaSb to $194 \Omega\text{cm}^2$ in $\text{In}_{0.043}\text{GaAsSb}$. Furthermore, the unintentional doping concentration, analysed from the capacitance-voltage data, decreased significantly with the introduction of In and As to the alloy, from $2.7 \times 10^{15} \text{ cm}^{-3}$ measured in GaSb to $6 \times 10^{14} \text{ cm}^{-3}$ measured in InGaAsSb alloys with 26 and 30% In. This is believed to be the lowest value ever reported for the background carrier concentration in InGaAsSb layers which is typically between

$1 \times 10^{15} - 5 \times 10^{16} \text{ cm}^{-3}$. The above trends point to a reduction in the native defect concentration known to be an issue in epitaxial GaSb. Fewer defect states in the lattice lead to lower SRH generation-recombination rates which results in lower bulk leakage currents, higher ideality factor, and lower background doping levels in InGaAsSb diodes compared to the GaSb ones. Although the initial improvement in leakage currents and R_0A product was followed by their worsening with even higher In fractions in the alloy, this was shown to be a direct consequence of the bandgap narrowing in these alloys which naturally leads to an increase in SRH leakage. Moreover, the investigation of the current density and $1/R_0A$ product with changing device dimensions revealed that all photodiodes are limited by surface leakage. While the photodiodes passivated with SU-8 photoresist did exhibit lower dark current densities, they were still dominated by surface leakage which highlights the need for the development of alternate passivation techniques. All InGaAsSb photodiodes exhibited an excellent external quantum efficiency between 65 and 70%, as measured with a $1.55 \mu\text{m}$ laser and with no anti-reflection coating applied. A nearly perfect EQE is expected with an AR coating, particularly at longer wavelengths closer to the photodiodes' cutoffs. The EQE also increased slightly with increasing In fractions in the alloy. GaSb on the other hand measured a much lower quantum efficiency of 48%. Moreover, the EQE was found to be largely independent of applied bias suggesting that the minority carrier diffusion length is greater than the active region thickness ($> 1\mu\text{m}$). The EQE values correspond to responsivities between 0.81 and 0.87 A/W at $1.55 \mu\text{m}$ and zero bias, although a higher responsivity of $\sim 1 \text{ A/W}$ can be expected at longer wavelengths closer to the absorption edge.

Finally, the detectors' signal-to-noise performance was summarised with the calculation of specific detectivity. Like the dark current density and the dynamic resistance-area product, the specific detectivity improved significantly with the introduction of In/As to the alloy, with a peak value of 8.08×10^{10} Jones measured in the photodiode with 4.3% In at -10 mV, while the GaSb photodiode measured a peak specific detectivity of 1.53×10^{10} Jones at -10 mV. Even though the absorption

coefficient and quantum efficiency continually increased with increasing In fractions in the alloy, the worsening of the R_0A product and leakage currents dominates the overall detector performance, leading to a gradual reduction of the specific detectivity in alloys with higher In fractions. The potential increase in specific detectivity with the reduction of surface leakage was demonstrated through the calculation of specific detectivity in the bulk-limited case as the upper limit for what could be achieved with the material. Specific detectivity as high as 1.55×10^{11} Jones was shown possible in the alloy with 4.3% In.

7.2 Future Work

Future work should include temperature dependent measurements of current density to shed light on the different current mechanisms, particularly Shockley-Read-Hall generation and surface recombination which are believed to be important contributions to leakage at room temperature in the devices characterised in this work. The activation energy extracted from the appropriate Arrhenius plot (current density against $1000/T$) close to room temperature should correspond to roughly half the bandgap in devices that are SRH limited. Surface limited devices on the other hand are typically weakly temperature dependent[22]. Furthermore, additional measurements need to be carried out to confirm the dopant type of the unintentionally doped intrinsic regions, and investigate whether or not the dopant type changes with In fraction in the alloy, which was suggested to be the case in a different study[118]. One potential avenue of obtaining the dopant type is through Hall measurements. However, this might not produce reliable results due to such low doping levels reported in these samples, and a different measurement technique might be preferable.

Although phase separation was observed through the broadening and decomposition of XRD peaks, additional PL measurements could be performed to obtain more information about the material quality. Sharp and bright PL emission peaks

have been associated with good quality, uniform epitaxial growth, while spectral broadening and lower PL intensities have been associated with alloy disorder and phase separation. Therefore, the evolution of the PL spectra with increasing In fractions in the alloy should closely follow the trend seen in XRD measurements. Moreover, a direct measurement of the observed phase separation could be made through transmission electron microscopy (TEM) in order to confirm the presence as well as the extent of the phase separation. Additionally, time resolved PL measurements could be performed to obtain the lifetime of minority carriers which is related to the density of traps in the material; the PL emission intensity will reduce quicker if more defects are present in the material as a result of the trapping of photogenerated carriers.

While passivation has been attempted in this work on select samples, they showed only marginal improvement. Therefore, a different passivation technique should be employed or developed to combat the high surface leakage that limits the performance of InGaAsSb devices. For example, surface treatment with an aqueous solution containing sulfur has been shown very effective in limiting surface recombination in InGaAsSb-based devices[156], [157]. Sulfur treatment should be followed by encapsulation in a dielectric such as SiO₂ to stabilize the surface and limit ageing-induced degradation. This layer can also serve as an anti-reflection coating which should improve the optical performance of the devices.

InGaAsSb photodetectors with dark current densities and specific detectivities comparable to commercially available extended InGaAs photodetectors have already been demonstrated[23], [140]. Even the non-optimised photodiodes reported in this work exhibit impressive and comparable detector performances. The main hurdle in fabricating low-leakage and high responsivity InGaAsSb photodiodes is their relatively high surface recombination current which has been noted in many other Sb-based semiconductor devices. As such, the development of suitable passivation and encapsulation techniques should be the focus of future work. Furthermore, very dilute alloy InGaAsSb photodiodes have demonstrated an impressively superior

performance compared to their GaSb counterparts. Therefore, if trying to achieve cutoff wavelengths similar to that of GaSb, it might be beneficial to use a dilute alloy InGaAsSb device instead.

One could potentially create a multi-stack structure where each layer has a different composition with the aim of extending the spectral response, however, this comes with several challenges. Firstly, the allowed In fractions before reaching the miscibility gap only cover a narrow 1.7 - 3 μm window. Secondly, stacking layers with different InGaAsSb compositions would introduce band misalignment, which might result in a device that requires a higher voltage or graded interfaces to lessen the potential barrier. Furthermore, the leakage of such a structure would still be limited by the alloy with the narrowest bandgap. As a result, it is believed that the challenges of creating such a structure outweigh the potential benefits.

In light of the results of this study and the comprehensive literature review conducted, we recommend a pBn architecture with a wide bandgap AlGa(As)Sb barrier as the most optimal photodetector structure employing the InGaAsSb material system. The built-in electric field ensures zero-bias operation at room temperature, while the AlGa(As)Sb barrier suppresses unwanted leakage currents. This detector design already achieved the highest specific detectivity of 9.7×10^{10} Jones to ever be recorded in an InGaAsSb photodetector at room temperature and zero bias[140].

References

- [1] M. Ahmetoglu (Afrailov), B. Kucur, I. Andreev, E. Kunitsyna, M. Mikhailova, and Y. Yakovlev, “Electrical and optical properties of the GaInAsSb-based heterojunctions for infrared photodiode and thermophotovoltaic cell application,” *Infrared Physics Technology*, vol. 53, no. 5, pp. 399–403, 2010. DOI: <https://doi.org/10.1016/j.infrared.2010.07.007>.
- [2] H. Hao, G. Wang, X. Han, *et al.*, “Extended-wavelength InGaAsSb infrared unipolar barrier detectors,” *AIP Advances*, vol. 8, no. 9, p. 095 106, Sep. 2018. DOI: <https://doi.org/10.1063/1.5026839>.
- [3] F. Cao, L. Liu, and L. Li, “Short-wave infrared photodetector,” *Materials Today*, vol. 62, pp. 327–349, Feb. 2023. DOI: <https://doi.org/10.1016/j.mattod.2022.11.003>.
- [4] Y. Uliel, D. Cohen-Elias, N. Sicon, *et al.*, “InGaAs/GaAsSb Type-II superlattice based photodiodes for short wave infrared detection,” *Infrared Physics Technology*, vol. 84, pp. 63–71, 2017. DOI: <https://doi.org/10.1016/j.infrared.2017.02.003>.
- [5] G. R. Savich, D. E. Sidor, X. Du, *et al.*, “III-V semiconductor extended short-wave infrared detectors,” *Journal of Vacuum Science Technology B*, vol. 35, no. 2, 02B105, Feb. 2017. DOI: [10.1116/1.4975340](https://doi.org/10.1116/1.4975340).
- [6] R. Sidhu, N. Duan, J. Campbell, and A. Holmes, “A long-wavelength photodiode on InP using lattice-matched GaInAs-GaAsSb type-II quantum

- wells,” *IEEE Photonics Technology Letters*, vol. 17, no. 12, pp. 2715–2717, 2005. DOI: 10.1109/LPT.2005.859163.
- [7] B. Chen and A. L. Holmes, “InP-based short-wave infrared and midwave infrared photodiodes using a novel type-II strain-compensated quantum well absorption region,” *Optics Letters*, vol. 38, no. 15, pp. 2750–2753, Aug. 2013. DOI: 10.1364/OL.38.002750.
- [8] J. Huang, W. Ma, Y. Wei, *et al.*, “How to Use Type II InAs/GaSb Superlattice Structure to Reach Detection Wavelength of 2–3 μm ,” *IEEE Journal of Quantum Electronics*, vol. 48, no. 10, pp. 1322–1326, 2012. DOI: 10.1109/JQE.2012.2210390.
- [9] A. Haddadi, R. Chevallier, A. Dehzangi, and M. Razeghi, “Extended short-wavelength infrared nBn photodetectors based on type-II InAs/AlSb/GaSb superlattices with an AlAsSb/GaSb superlattice barrier,” *Applied Physics Letters*, vol. 110, no. 10, p. 101 104, Mar. 2017. DOI: 10.1063/1.4978378.
- [10] D. Cohen-Elias, N. Snapi, O. Klin, *et al.*, “Minority carrier diffusion length for electrons in an extended SWIR InAs/AlSb type-II superlattice photodiode,” *Applied Physics Letters*, vol. 111, no. 20, p. 201 106, Nov. 2017. DOI: 10.1063/1.5005097.
- [11] D. Cohen-Elias, Y. Uliel, O. Klin, *et al.*, “Short wavelength infrared InAs/InSb/AlSb type-II superlattice photodetector,” *Infrared Physics & Technology*, vol. 84, pp. 82–86, 2017. DOI: <https://doi.org/10.1016/j.infrared.2017.01.005>.
- [12] A. Haddadi, X. V. Suo, S. Adhikary, *et al.*, “High-performance short-wavelength infrared photodetectors based on type-II InAs/InAs_{1-x}Sb_x/AlAs_{1-x}Sb_x superlattices,” *Applied Physics Letters*, vol. 107, no. 14, p. 141 104, Oct. 2015. DOI: 10.1063/1.4932518.

-
- [13] D. Cohen-Elias, Y. Uliel, N. Cohen, I. Shafir, O. Westreich, and M. Katz, “Short wavelength infrared pBn GaSb/AlAsSb/InPSb photodetector,” *Infrared Physics & Technology*, vol. 85, pp. 81–85, 2017, ISSN: 1350-4495. DOI: <https://doi.org/10.1016/j.infrared.2017.05.021>.
- [14] C. Li, Y. Zhang, K. Wang, Y. Gu, H. Li, and Y. Li, “Distinction investigation of InGaAs photodetectors cutoff at 2.9 μm ,” *Infrared Physics Technology*, vol. 53, no. 3, pp. 173–176, 2010. DOI: <https://doi.org/10.1016/j.infrared.2009.11.002>.
- [15] A. Rogalski and R. Ciupa, “Performance Limitation of Short Wavelength Infrared InGaAs and HgCdTe Photodiodes,” *Journal of Electronic Materials*, vol. 28, no. 6, pp. 630–636, 1999. DOI: <https://doi.org/10.1007/s11664-999-0046-6>.
- [16] B. Liang, D. Chen, B. Wang, T. A. Kwasniewski, and Z. Wang, “Analysis, Optimization, and Design of 2–2.8 μm Stacked Multiple-Junction PIN GaInAsSb/GaSb Photodetectors for Future O/E Interconnections,” *IEEE Transactions on Electron Devices*, vol. 57, no. 2, pp. 361–367, 2010. DOI: [10.1109/TED.2009.2036303](https://doi.org/10.1109/TED.2009.2036303).
- [17] M. Mitsuhashi, Y. Ohiso, and H. Matsuzaki, “Strain-compensated InGaAsSb/InGaAsSb multiquantum-well structure grown on InP (001) substrate as optical absorber for wavelengths beyond 2 μm ,” *Journal of Crystal Growth*, vol. 535, p. 125551, 2020. DOI: <https://doi.org/10.1016/j.jcrysgro.2020.125551>.
- [18] A. Yildirim and J. P. Prineas, “Suppressed phase separation in thick GaInAsSb layers across the compositional range grown by molecular beam epitaxy for 1.7–4.9 μm infrared materials,” *Journal of Vacuum Science and Technology B*, vol. 30, no. 2, 02B104, Mar. 2012. DOI: <https://doi.org/10.1116/1.3668088>.

- [19] F. M. Mohammedy and M. J. Deen, "Growth and fabrication issues of GaSb-based detectors," *Journal of Materials Science: Materials in Electronics*, vol. 20, pp. 1039–1058, May 2009. DOI: <https://doi.org/10.1007/s10854-009-9927-y>.
- [20] P. S. Dutta, H. L. Bhat, and V. Kumar, "The physics and technology of gallium antimonide: An emerging optoelectronic material," *Journal of Applied Physics*, vol. 81, no. 9, pp. 5821–5870, May 1997. DOI: <https://doi.org/10.1063/1.3653566>.
- [21] A. Bainbridge, K. Mamic, L. A. Hanks, F. Al-Saymari, A. P. Craig, and A. R. J. Marshall, "Resonant Cavity Enhanced Photodiodes in the Short-Wave Infrared for Spectroscopic Detection," *IEEE Photonics Technology Letters*, vol. 32, no. 21, pp. 1369–1372, Nov. 2020. DOI: [10.1109/LPT.2020.3025977](https://doi.org/10.1109/LPT.2020.3025977).
- [22] A. P. Craig, M. Jain, G. Wicks, *et al.*, "Short-wave infrared barrier detectors using InGaAsSb absorption material lattice matched to GaSb," *Applied Physics Letters*, vol. 106, no. 20, p. 201103, May 2015. DOI: <https://doi.org/10.1063/1.4921468>.
- [23] M. W. Dashiell, J. F. Beausang, H. Ehsani, *et al.*, "Quaternary InGaAsSb Thermophotovoltaic Diodes," *IEEE Transactions on Electron Devices*, vol. 53, no. 12, pp. 2879–2891, Dec. 2006. DOI: [10.1109/TED.2006.885087](https://doi.org/10.1109/TED.2006.885087).
- [24] K. Qiu, A. C. S. Hayden, M. G. Mauk, and O. V. Sulima, "Generation of electricity using InGaAsSb and GaSb TPV cells in combustion-driven radiant sources," *Solar Energy Materials and Solar Cells*, vol. 90, no. 1, pp. 68–81, Jan. 2005. DOI: <https://doi.org/10.1016/j.solmat.2005.02.002>.
- [25] S. Suchalkin, S. Jung, G. Kipshidze, *et al.*, "GaSb based light emitting diodes with strained InGaAsSb type I quantum well active regions," *Applied Physics Letters*, vol. 93, no. 8, Aug. 2008. DOI: <https://doi.org/10.1063/1.2974795>.

-
- [26] T. D. Nguyen, J. O. Kim, and S. J. Lee, “Growth of InGaAsSb/GaSb compound for infrared optoelectronic devices,” *Condensed Matter and Interphases*, vol. 24, no. 2, pp. 250–255, May 2022. DOI: <https://doi.org/10.17308/kcmf.2022.24/9265>.
- [27] D. Donetsky, G. Kipshidze, L. Shterengas, T. Hosoda, and G. Belenky, “2.3 μm type-I quantum well GaInAsSb/AlGaAsSb/GaSb laser diodes with quasi-CW output power of 1.4 W,” *Electronics Letters*, vol. 43, no. 15, Jul. 2007.
- [28] J. B. Rodriguez, L. Cerutti, and E. Tournié, “GaSb-based, 2.2 μm type-I laser fabricated on GaAs substrate operating continuous wave at room temperature,” *Applied Physics Letters*, vol. 94, no. 2, Jan. 2009. DOI: <https://doi.org/10.1063/1.3072596>.
- [29] E. Tournié, J.-L. Lazzari, F. Pitard, C. Alibert, A. Joullié, and B. Lambert, “2.5 μm GaInAsSb lattice-matched to GaSb by liquid phase epitaxy,” *Journal of Applied Physics*, vol. 68, no. 11, pp. 5936–5938, Dec. 1990. DOI: <https://doi.org/10.1063/1.346925>.
- [30] M. Piskorski, A. Piotrowska, T. T. Piotrowski, *et al.*, “LPE growth and characterisation of GaInAsSb and GaAlAsSb quaternary layers on (100) GaSb substrates,” *Thin Solid Films*, vol. 459, no. 1, pp. 2–6, Jul. 2004. DOI: <https://doi.org/10.1016/j.tsf.2003.12.072>.
- [31] V. Bhagwat, Y. Xiao, I. Bhat, *et al.*, “Analysis of leakage currents in MOCVD grown GaInAsSb based photodetectors operating at 2 μm ,” *Journal of Electronic Materials*, vol. 35, pp. 1613–1617, Aug. 2006. DOI: <https://doi.org/10.1007/s11664-006-0206-x>.
- [32] B. Zhang, T. Zhou, H. Jiang, Y. Ning, and Y. Jin, “GaInAsSb/GaSb infrared photodetectors prepared by MOCVD,” *Electronics Letters*, vol. 31, no. 10, pp. 830–832, May 1995.

- [33] C. A. Wang, D. R. Calawa, and C. J. Vineis, "Evolution of surface structure and phase separation in GaInAsSb," *Journal of Crystal Growth*, vol. 225, no. 2-4, pp. 377–383, May 2001. DOI: [https://doi.org/10.1016/S0022-0248\(01\)00884-3](https://doi.org/10.1016/S0022-0248(01)00884-3).
- [34] C. A. Wang, "Step structure of GaInAsSb grown by organometallic vapor phase epitaxy," *Journal of Electronic Materials*, vol. 29, no. 1, pp. 112–117, Jan. 2000. DOI: <https://doi.org/10.1007/s11664-000-0105-5>.
- [35] A. N. Semenov, Y. V. Terent'ev, B. Y. Meltser, *et al.*, "Molecular Beam Epitaxy of Thermodynamically Metastable GaInAsSb Alloys for Medium IR-Range Photodetectors," *Semiconductors*, vol. 44, no. 5, pp. 672–677, May 2010. DOI: <https://doi.org/10.1134/S1063782610050222>.
- [36] G. B. Stringfellow, "IMMISCIBILITY AND SPINODAL DECOMPOSITION IN III/V ALLOYS," *Journal of Crystal Growth*, vol. 65, no. 1-3, pp. 454–462, Dec. 1983. DOI: [https://doi.org/10.1016/0022-0248\(83\)90086-6](https://doi.org/10.1016/0022-0248(83)90086-6).
- [37] G. B. Stringfellow, "ORDERED STRUCTURES AND METASTABLE ALLOYS GROWN BY OMVPE," *Journal of Crystal Growth*, vol. 98, no. 1-2, pp. 108–117, Nov. 1989. DOI: [https://doi.org/10.1016/0022-0248\(89\)90191-7](https://doi.org/10.1016/0022-0248(89)90191-7).
- [38] R. Kaspi and G. P. Donati, "Digital alloy growth in mixed as/sb heterostructures," *Journal of Crystal Growth*, vol. 251, no. 1, pp. 515–520, 2003. DOI: [https://doi.org/10.1016/S0022-0248\(02\)02185-1](https://doi.org/10.1016/S0022-0248(02)02185-1).
- [39] R. Wang, D. Chen, J. A. McArthur, *et al.*, "Al_{0.3}In_{0.7}AsSb digital alloy nbn photodetectors," *Journal of Lightwave Technology*, vol. 40, no. 1, pp. 113–120, Jan. 2022.
- [40] S. J. Maddox, S. D. March, and S. R. Bank, "Broadly Tunable AlInAsSb Digital Alloys Grown on GaSb," *Crystal Growth & Design*, vol. 16, no. 7, pp. 3582–3586, 2016. DOI: [10.1021/acs.cgd.5b01515](https://doi.org/10.1021/acs.cgd.5b01515).

-
- [41] B. Wen'gang and L. Azihen, "Band Gap Energy and Its Temperature Dependence of GaInAsSb Quaternary Alloy Grown by Molecular Beam Epitaxy," *Chinese Physics Letters*, vol. 9, no. 1, p. 53, Jan. 1992. DOI: 10.1088/0256-307X/9/1/015.
- [42] M. Muñoz, K. Wei, F. H. Pollak, J. L. Freeouf, C. A. Wang, and G. W. Charache, "Optical constants of $\text{Ga}_{1-x}\text{In}_x\text{As}_y\text{Sb}_{1-y}$ lattice matched to GaSb (001): Experiment and modeling," *Journal of Applied Physics*, vol. 87, no. 4, pp. 1780–1787, Feb. 2000. DOI: <https://doi.org/10.1063/1.372092>.
- [43] E. Tournie, J.-L. Lazzari, E. Villemain, *et al.*, "GaInAsSb/GaSb pn photodiodes for detection to 2.4 μm ," *Electronics Letters*, vol. 27, no. 14, pp. 1237–1239, Jul. 1991. DOI: 10.1049/e1:19910776.
- [44] A. Li, J. Zhong, Y. Zheng, *et al.*, "Molecular beam epitaxial growth, characterization and performance of high-detectivity GaInAsSb/GaSb PIN detectors operating at 2.0 to 2.6 μm ," *Journal of Crystal Growth*, vol. 150, pp. 1375–1378, May 1995. DOI: [https://doi.org/10.1016/0022-0248\(95\)80163-4](https://doi.org/10.1016/0022-0248(95)80163-4).
- [45] C. A. Wang, H. K. Choi, D. C. Oakley, and G. W. Charache, "Extending the cutoff wavelength of lattice-matched GaInAsSb/GaSb thermophotovoltaic devices," *AIP Conference Proceedings*, vol. 460, no. 1, pp. 256–265, Mar. 1999. DOI: <https://doi.org/10.1063/1.57805>.
- [46] J.-L. Lazzari, F. De Anda, J. Nieto, *et al.*, "Carrier Concentration Control of GaSb/GaInAsSb System," *AIP Conference Proceedings*, vol. 890, no. 1, pp. 115–126, Feb. 2007. DOI: 10.1063/1.2711727.
- [47] M. Fox, *Optical Properties of Solids* (Condensed Matter Physics), second. Oxford University Press, 2010, vol. 3.
- [48] J. I. Pankove, *Optical Processes in Semiconductors* (Solid state physical electronics series). Prentice-Hall, 1971.

- [49] S. T. Schaefer, S. Gao, P. T. Webster, R. R. Kosireddy, and S. R. Johnson, “Absorption edge characteristics of GaAs, GaSb, InAs, and InSb,” *Journal of Applied Physics*, vol. 127, no. 16, p. 165705, Apr. 2020. DOI: <https://doi.org/10.1063/5.0003001>.
- [50] R. K. Willardson and A. C. Beer, *Semiconductors and semimetals* (Optical Properties of III-V Compounds), second. Academic Press, 1972.
- [51] E. Rosencher and B. Vinter, *Optoelectronics*. Cambridge University Press, 2002.
- [52] J. I. Pankove, “Absorption Edge of Impure Gallium Arsenide,” *Physical Review*, vol. 140, A2059–A2065, 6A Dec. 1965. DOI: <https://doi.org/10.1103/PhysRev.140.A2059>.
- [53] B. Bansal, V. K. Dixit, V. Venkataraman, and H. L. Bhat, “Alloying induced degradation of the absorption edge of $\text{InAs}_x\text{Sb}_{1-x}$,” *Applied Physics Letters*, vol. 90, no. 10, p. 101905, Mar. 2007. DOI: <https://doi.org/10.1063/1.2711388>.
- [54] C. W. Greeff and H. R. Glyde, “Anomalous Urbach tail in GaAs,” *Physical Review B*, vol. 51, pp. 1778–1783, 3 Jan. 1995. DOI: <https://doi.org/10.1103/PhysRevB.51.1778>.
- [55] S. R. Johnson and T. Tiedje, “Temperature dependence of the Urbach edge in GaAs,” *Journal of Applied Physics*, vol. 78, no. 9, pp. 5609–5613, Nov. 1995. DOI: <https://doi.org/10.1063/1.359683>.
- [56] S. Sze and L. Ming-Kwei, *Semiconductor Devices: Physics and Technology*, third. John Wiley & Sons Singapore Pte. Limited, 2012.
- [57] G. Parker, *Introductory semiconductor device physics*. Prentice Hall International, 1994.
- [58] A. Rogers, *Essentials of Optoelectronics with applications* (Optical and Quantum Electronics Series). Chapman & Hall, 1997, vol. 4.

-
- [59] J. Wilson and J. Hawkes, *Optoelectronics: An Introduction* (Prentice Hall international series in optoelectronics), third. Prentice Hall Europe, 1998.
- [60] I. Andreev, N. Il'inskaya, E. Kunitsyna, M. Mikhailova, and Y. P. Yakovlev, "High-efficiency GaInAsSb/GaAlAsSb photodiodes for 0.9-to 2.55- μm spectral range with a large-diameter active area," *Semiconductors*, vol. 37, pp. 949–954, Aug. 2003. DOI: <https://doi.org/10.1134/1.1601665>.
- [61] H. Shao, A. Torfi, W. Li, D. Moscicka, and W. Wang, "High detectivity AlGaAsSb/InGaAsSb photodetectors grown by molecular beam epitaxy with cutoff wavelength up to 2.6 μm ," *Journal of Crystal Growth*, vol. 311, no. 7, pp. 1893–1896, Mar. 2009. DOI: <https://doi.org/10.1016/j.jcrysgro.2008.12.009>.
- [62] B. G. Streetman and S. Banerjee, *Solid state electronic devices* (Prentice Hall Series in Solid State Physical Electronics), fifth. Prentice hall International, 2000.
- [63] S. M. Sze and K. K. Ng, *Physics of Semiconductor Devices*, third. John Wiley & Sons, 2006.
- [64] M. Razeghi and A. Rogalski, "Semiconductor ultraviolet detectors," *Journal of Applied Physics*, vol. 79, no. 10, pp. 7433–7473, May 1996. DOI: <https://doi.org/10.1063/1.362677>.
- [65] A. Rogalski and M. Razeghi, "Narrow-gap semiconductor photodiodes," in *Photodetectors: Materials and Devices III*, G. J. Brown, Ed., International Society for Optics and Photonics, vol. 3287, SPIE, 1998, pp. 2–13. DOI: 10.1117/12.304467.
- [66] G. R. Savich, "Analysis and suppression of dark currents in mid-wave infrared photodetectors," Ph.D. dissertation, University of Rochester, 2015.
- [67] V. Gopal, "Variable-area diode data analysis of surface and bulk effects in HgCdTe photodetector arrays," *Semiconductor Science and Technology*, vol. 9, no. 12, p. 2267, Dec. 1994. DOI: 10.1088/0268-1242/9/12/018.

- [68] V. Gopal, “A general relation between zero-bias resistance - area product and perimeter-to-area ratio of the diodes in variable-area diode test structures,” *Semiconductor Science and Technology*, vol. 11, no. 7, p. 1070, Jul. 1996. DOI: 10.1088/0268-1242/11/7/018.
- [69] J. P. Prineas, J. Yager, S. Seyedmohamadi, and J. T. Olesberg, “Leakage mechanisms and potential performance of molecular-beam epitaxially grown GaInAsSb 2.4 μm photodiode detectors,” *Journal of Applied Physics*, vol. 103, no. 10, p. 104511, May 2008. DOI: <https://doi.org/10.1063/1.2932080>.
- [70] V. Letka, “Medium- and long-wavelength InAs/InAsSb strained-layer superlattices for applications in infrared nBn detectors,” Ph.D. dissertation, Lancaster University, 2019.
- [71] J. Venter and S. Sinha, “Thermal and flicker noise improvement in short-channel CMOS detectors,” in *Sensors, MEMS and Electro-Optical Systems*, M. du Plessis, Ed., International Society for Optics and Photonics, vol. 9257, SPIE, 2014, 92570Q. DOI: 10.1117/12.2064735.
- [72] H. M. Oloomi, M. S. Alam, and M. M. Rana, “Noise Performance Evaluation of Uncooled Infrared Detectors,” *IEEE Sensors Journal*, vol. 11, no. 4, pp. 971–987, 2011. DOI: 10.1109/JSEN.2010.2069559.
- [73] K. Achtenberg, J. Mikołajczyk, C. Ciofi, G. Scandurra, K. Michalczewski, and Z. Bielecki, “Low-frequency noise measurements of IR photodetectors with voltage cross correlation system,” *Measurement*, vol. 183, p. 109867, Oct. 2021. DOI: <https://doi.org/10.1016/j.measurement.2021.109867>.
- [74] K. Nakashima, “Electrical and Optical Studies in Gallium Antimonide,” *Japanese Journal of Applied Physics*, vol. 20, no. 6, pp. 1085–1094, Jun. 1981. DOI: 10.1143/JJAP.20.1085.

-
- [75] M. Lee, D. J. Nicholas, K. E. Singer, and B. Hamilton, “A photoluminescence and Hall-effect study of GaSb grown by molecular-beam epitaxy,” *Journal of Applied Physics*, vol. 59, no. 8, pp. 2895–2900, Apr. 1986.
- [76] E. T. R. Chidley, S. K. Haywood, A. B. Henriques, N. J. Mason, R. J. Nicholas, and P. J. Walker, “Photoluminescence of GaSb grown by metal-organic vapour phase epitaxy,” *Semiconductor Science and Technology*, vol. 6, no. 1, pp. 45–53, Jan. 1991. DOI: [10.1088/0268-1242/6/1/009](https://doi.org/10.1088/0268-1242/6/1/009).
- [77] G. W. Turner, S. J. Eglash, and A. J. Strauss, “Molecular-beam epitaxial growth of high-mobility n-GaSb,” *Journal of Vacuum Science ‘IT’ Technology B*, vol. 11, no. 3, pp. 864–867, May 1993. DOI: <https://doi.org/10.1116/1.586767>.
- [78] S. Roux, P. Barritault, O. Lartigue, *et al.*, “Mid-infrared characterization of refractive indices and propagation losses in GaSb/Al_xGa_{1-x}AsSb waveguides,” *Applied Physics Letters*, vol. 107, no. 17, p. 171 901, Oct. 2015. DOI: <https://doi.org/10.1063/1.4934702>.
- [79] W. G. Hu, Z. Wang, B. F. Su, Y. Q. Dai, S. J. Wang, and Y. W. Zhao, “Gallium antisite defect and residual acceptors in undoped GaSb,” *Physics Letters A*, vol. 332, no. 3-4, pp. 286–290, Nov. 2004. DOI: <https://doi.org/10.1016/j.physleta.2004.09.056>.
- [80] Anayama, C. and Tanahashi, T. and Kuwatsuka, H. and Nishiyama, S. and Isozumi, S. and Nakajima, K., “High-purity GaSb epitaxial layers grown from Sb-rich solutions,” *Applied Physics Letters*, vol. 56, no. 3, pp. 239–240, Jan. 1990. DOI: [10.1063/1.102842](https://doi.org/10.1063/1.102842).
- [81] K. F. Longenbach and W. I. Wang, “Molecular beam epitaxy of GaSb,” *Applied Physics Letters*, vol. 59, no. 19, pp. 2427–2429, Nov. 1991. DOI: <https://doi.org/10.1063/1.106037>.

- [82] A. Baraldi, C. Ghezzi, R. Magnanini, *et al.*, “Preparation of GaSb by molecular beam epitaxy and electrical and photoluminescence characterization,” *Materials Science and Engineering: B*, vol. 28, no. 1-3, pp. 174–178, Dec. 1994. DOI: [https://doi.org/10.1016/0921-5107\(94\)90041-8](https://doi.org/10.1016/0921-5107(94)90041-8).
- [83] M. Hakala, M. J. Puska, and R. M. Nieminen, “Native defects and self-diffusion in GaSb,” *Journal of Applied Physics*, vol. 91, no. 8, pp. 4988–4994, Apr. 2002. DOI: <https://doi.org/10.1063/1.1462844>.
- [84] V. Virkkala, V. Havu, F. Tuomisto, and M. J. Puska, “Native point defect energetics in GaSb: Enabling *p*-type conductivity of undoped GaSb,” *Physical Review B*, vol. 86, p. 144 101, 14 Oct. 2012. DOI: <https://doi.org/10.1103/PhysRevB.86.144101>.
- [85] J. Buckeridge, T. D. Veal, C. R. A. Catlow, and D. O. Scanlon, “Intrinsic point defects and the *n*- and *p*-type dopability of the narrow gap semiconductors GaSb and InSb,” *Physical Review B*, vol. 100, no. 3, p. 035 207, Jul. 2019. DOI: <https://doi.org/10.1103/PhysRevB.100.035207>.
- [86] C. C. Ling, M. K. Lui, S. K. Ma, X. D. Chen, S. Fung, and C. D. Beling, “Nature of the acceptor responsible for *p*-type conduction in liquid encapsulated Czochralski-grown undoped gallium antimonide,” *Applied Physics Letters*, vol. 85, no. 3, pp. 384–386, Jul. 2004. DOI: <https://doi.org/10.1063/1.1773934>.
- [87] J. Kujala, N. Segercrantz, F. Tuomisto, and J. Slotte, “Native point defects in GaSb,” *Journal of Applied Physics*, vol. 116, no. 14, p. 143 508, Oct. 2014. DOI: <https://doi.org/10.1063/1.4898082>.
- [88] A. Salesse, A. Joullié, P. Calas, *et al.*, “Surface passivation of GaInAsSb photodiodes with thioacetamide,” *Physica Status Solidi C*, vol. 4, no. 4, pp. 1508–1512, Mar. 2007. DOI: <https://doi.org/10.1002/pssc.200674138>.

- [89] M. Perotin, P. Coudray, L. Gousskov, *et al.*, “Passivation of GaSb by sulfur treatment,” *Journal of Electronic Materials*, vol. 23, pp. 7–12, Jan. 1994. DOI: <https://doi.org/10.1007/BF02651260>.
- [90] C. L. Lin, Y. K. Su, T. S. Se, and W. L. Li, “Variety Transformation of Compound at GaSb Surface under Sulfur Passivation,” *Japanese Journal of Applied Physics*, vol. 37, no. 12B, pp. L1543–L1545, Dec. 1998. DOI: 10.1143/JJAP.37.L1543.
- [91] P. S. Dutta, J. Langer, V. Bhagwat, and J. Juneja, “Dry etching, surface passivation and capping processes for antimonide based photodetectors,” in *Infrared Technology and Applications XXXI*, B. F. Andresen and G. F. Fulop, Eds., International Society for Optics and Photonics, vol. 5783, SPIE, 2005, pp. 98–105. DOI: 10.1117/12.605330.
- [92] M. Kodama, “Improvement of reverse leakage current characteristics of GaSb and $\text{Al}_{0.3}\text{Ga}_{0.7}\text{Sb}/\text{GaSb}$ diodes grown by MBE,” *Solid-State Electronics*, vol. 37, no. 8, pp. 1567–1569, Aug. 1994. DOI: [https://doi.org/10.1016/0038-1101\(94\)90167-8](https://doi.org/10.1016/0038-1101(94)90167-8).
- [93] E. Kunitsyna, T. L’vova, M. Dunaevskii, *et al.*, “Wet sulfur passivation of GaSb(100) surface for optoelectronic applications,” *Applied Surface Science*, vol. 256, no. 18, pp. 5644–5649, Jul. 2010. DOI: <https://doi.org/10.1016/j.apsusc.2010.03.027>.
- [94] R.-L. Chu, W.-J. Hsueh, T.-H. Chiang, *et al.*, “Surface Passivation of GaSb(100) Using Molecular Beam Epitaxy of Y_2O_3 and Atomic Layer Deposition of Al_2O_3 : A Comparative Study,” *Applied Physics Express*, vol. 6, no. 12, p. 121201, Nov. 2013. DOI: 10.7567/APEX.6.121201.
- [95] X. Fang, Z. Wei, D. Fang, *et al.*, “Surface State Passivation and Optical Properties Investigation of GaSb via Nitrogen Plasma Treatment,” *ACS Omega*, vol. 3, no. 4, pp. 4412–4417, Apr. 2018. DOI: <https://doi.org/10.1021/acsomega.7b01783>.

- [96] Y. Ji, K. M. Azizur-Rahman, T. Chang, *et al.*, “Optimization of surface passivation for suppressing leakage current in GaSb PIN devices,” *Electronics Letters*, vol. 56, no. 25, pp. 1420–1423, Dec. 2020. DOI: <https://doi.org/10.1049/e1.2020.2063>.
- [97] J. C. DeWinter, M. A. Pollack, A. K. Srivastava, and J. L. Zyskind, “Liquid phase epitaxial $\text{Ga}_{1-x}\text{In}_x\text{As}_y\text{Sb}_{1-y}$ lattice-matched to (100) GaSb over the 1.71 to 2.33 μm wavelength range,” *Journal of Electronic Materials*, vol. 14, no. 6, pp. 729–747, 1985. DOI: <https://doi.org/10.1007/BF02654308>.
- [98] T. H. Chiu, J. L. Zyskind, and W. T. Tsang, “Molecular Beam Epitaxial Growth of InGaAsSb on (100) GaSb with Emission Wavelength in the 2 to 2.5 μm Range,” *Journal of Electronic Materials*, vol. 16, no. 1, pp. 57–61, 1987. DOI: <https://doi.org/10.1007/BF02667791>.
- [99] N. Li, G. Wang, D. Jiang, *et al.*, “Trap-assisted tunneling current and quantum efficiency loss in InGaAsSb short wavelength infrared photo detectors,” *Semiconductor Science and Technology*, vol. 37, no. 11, p. 115 010, Oct. 2022. DOI: [10.1088/1361-6641/ac9699](https://doi.org/10.1088/1361-6641/ac9699).
- [100] I. Vurgaftman, J. R. Meyer, and L. R. Ram-Mohan, “Band parameters for III–V compound semiconductors and their alloys,” *Journal of Applied Physics*, vol. 89, no. 11, pp. 5815–5875, Jun. 2001. DOI: [10.1063/1.1368156](https://doi.org/10.1063/1.1368156).
- [101] G. B. Stringfellow, “MISCIBILITY GAPS IN QUATERNARY III/V ALLOYS,” *Journal of Crystal Growth*, vol. 58, no. 1, pp. 194–202, Jun. 1982. DOI: [https://doi.org/10.1016/0022-0248\(82\)90226-3](https://doi.org/10.1016/0022-0248(82)90226-3).
- [102] K. Nakajima, K. Osamura, K. Yasuda, and Y. Murakami, “The pseudoquaternary phase diagram of the Ga-In-As-Sb system,” *Journal of Crystal Growth*, vol. 41, no. 1, pp. 87–92, Nov. 1977. DOI: [https://doi.org/10.1016/0022-0248\(77\)90100-2](https://doi.org/10.1016/0022-0248(77)90100-2).

-
- [103] M.-C. Wu, C.-C. Chen, and C.-T. Lee, "Growth and characterization of high-quality GaInAsSb layers on GaSb substrates by liquid-phase epitaxy," *Solid-State Electronics*, vol. 35, no. 4, pp. 523–528, Apr. 1992. DOI: [https://doi.org/10.1016/0038-1101\(92\)90115-S](https://doi.org/10.1016/0038-1101(92)90115-S).
- [104] M. Astles, H. Hill, A. Williams, P. Wright, and M. Young, "Studies of the $\text{Ga}_{1-x}\text{In}_x\text{As}_y\text{Sb}_{1-y}$ quaternary alloy system I. liquid-phase epitaxial growth and assessment," *Journal of Electronic Materials*, vol. 15, pp. 41–49, Jan. 1986. DOI: <https://doi.org/10.1007/BF02649949>.
- [105] C. A. Wang, D. R. Calawa, and C. J. Vineis, "OMVPE growth of GaInAsSb in the 2–2.4 μm range," *Journal of Crystal Growth*, vol. 191, no. 4, pp. 631–640, Aug. 1998. DOI: [https://doi.org/10.1016/S0022-0248\(98\)00367-4](https://doi.org/10.1016/S0022-0248(98)00367-4).
- [106] C. A. Wang, H. K. Choi, S. L. Ransom, G. W. Charache, L. R. Danielson, and D. M. DePoy, "High-quantum-efficiency 0.5 eV GaInAsSb/GaSb thermophotovoltaic devices," *Applied Physics Letters*, vol. 75, no. 9, pp. 1305–1307, Aug. 1999. DOI: <https://doi.org/10.1063/1.124676>.
- [107] C. A. Wang, "Correlation between surface step structure and phase separation in epitaxial GaInAsSb," *Applied Physics Letters*, vol. 76, no. 15, pp. 2077–2079, Apr. 2000. DOI: [10.1063/1.126260](https://doi.org/10.1063/1.126260).
- [108] C. A. Wang, H. K. Choi, and G. W. Charache, "Epitaxial growth of GaInAsSb for thermophotovoltaic devices," *IEEE Transactions on Electron Devices*, vol. 47, no. 3, pp. 193–198, Jun. 2000. DOI: [10.1049/ip-opt:20000480](https://doi.org/10.1049/ip-opt:20000480).
- [109] C. Wang, "Progress and continuing challenges in GaSb-based III–V alloys and heterostructures grown by organometallic vapor-phase epitaxy," *Journal of Crystal Growth*, vol. 272, no. 1, pp. 664–681, Dec. 2004. DOI: <https://doi.org/10.1016/j.jcrysgro.2004.09.019>.
- [110] A. Yildirim and J. P. Prineas, "Strain- and kinetically induced suppression of phase separation in MBE-grown metastable and unstable GaInAsSb quaternary alloys for mid-infrared optoelectronics," *Journal of Vacuum Science and Technology*, vol. 32, no. 3, pp. 1000–1005, Jun. 2014. DOI: <https://doi.org/10.1116/1.2368000>.

- Science 'T&' Technology B*, vol. 31, no. 3, p. 03C125, Apr. 2013. DOI: <https://doi.org/10.1116/1.4799352>.
- [111] T. Glisson, J. Hauser, M. Littlejohn, and C. Williams, “Energy bandgap and lattice constant contours of III-V quaternary alloys,” *Journal of Electronic Materials*, vol. 7, pp. 1–16, Jan. 1978. DOI: <https://doi.org/10.1007/BF02656016>.
- [112] S. Adachi, “III-V Ternary and Quaternary Compounds,” in *Springer Handbook of Electronic and Photonic Materials*, S. Kasap and P. Capper, Eds. Cham: Springer International Publishing, Oct. 2017, pp. 725–741. DOI: 10.1007/978-3-319-48933-9_30.
- [113] A. G. Thompson and J. C. Woolley, “ENERGY-GAP VARIATION IN MIXED III–V ALLOYS,” *Canadian Journal of Physics*, vol. 45, no. 2, pp. 255–261, Feb. 1967. DOI: <https://doi.org/10.1139/p67-026>.
- [114] R. Moon, G. Antypas, and L. James, “Bandgap and lattice constant of GaInAsP as a function of alloy composition,” *Journal of Electronic Materials*, vol. 3, pp. 635–644, Aug. 1974. DOI: <https://doi.org/10.1007/BF02655291>.
- [115] S. Adachi, “Band gaps and refractive indices of AlGaAsSb, GaInAsSb, and InPAsSb: Key properties for a variety of the 2–4- μm optoelectronic device applications,” *Journal of Applied Physics*, vol. 61, no. 10, pp. 4869–4876, May 1987. DOI: <https://doi.org/10.1063/1.338352>.
- [116] M. Cherng, G. Stringfellow, D. Kisker, A. Srivastava, and J. Zyskind, “GaInAsSb metastable alloys grown by organometallic vapor phase epitaxy,” *Applied Physics Letters*, vol. 48, no. 6, pp. 419–421, Feb. 1986. DOI: <https://doi.org/10.1063/1.96517>.
- [117] M. Cherng, H. Jen, C. Larsen, G. Stringfellow, H. Lundt, and P. Taylor, “MOVPE growth of GaInAsSb,” *Journal of Crystal Growth*, vol. 77, no. 1,

- pp. 408–417, Sep. 1986. DOI: [https://doi.org/10.1016/0022-0248\(86\)90331-3](https://doi.org/10.1016/0022-0248(86)90331-3).
- [118] V. Rakovics, A. Tóth, B. Podör, C. Frigeri, J. Balázs, and Z. Horváth, “Liquid phase epitaxy growth and characterization of $\text{Ga}_{1-x}\text{In}_x\text{As}_y\text{Sb}_{1-y}$ quaternary alloys,” *Materials Science and Engineering: B*, vol. 91-92, pp. 83–86, Apr. 2002. DOI: [https://doi.org/10.1016/S0921-5107\(01\)00978-3](https://doi.org/10.1016/S0921-5107(01)00978-3).
- [119] J. A. Gonzalez-Cuevas, T. F. Refaat, M. N. Abedin, and H. E. Elsayed-Ali, “Calculations of the temperature and alloy composition effects on the optical properties of $\text{Al}_x\text{Ga}_{1-x}\text{As}_y\text{Sb}_{1-y}$ and $\text{Ga}_x\text{In}_{1-x}\text{As}_y\text{Sb}_{1-y}$ in the spectral range 0.5–6 eV,” *Journal of Applied Physics*, vol. 102, no. 1, p. 014504, Jul. 2007. DOI: <https://doi.org/10.1063/1.2751406>.
- [120] X. Peng, X. Guo, B. Zhang, *et al.*, “Numerical analysis of the short-circuit current density in GaInAsSb thermophotovoltaic diodes,” *Infrared Physics ‘I&E’ Technology*, vol. 52, no. 4, pp. 152–157, Jul. 2009. DOI: <https://doi.org/10.1016/j.infrared.2009.06.003>.
- [121] X. Peng, B. Zhang, G. Li, *et al.*, “Simulation of temperature-dependent material parameters and device performances for GaInAsSb thermophotovoltaic cell,” *Infrared Physics ‘I&E’ Technology*, vol. 54, no. 6, pp. 454–459, 2011. DOI: <https://doi.org/10.1016/j.infrared.2011.08.005>.
- [122] X.-L. Zhang, A.-B. Huang, Y.-Y. Lou, X. Li, M. Cui, and Y. Wang, “Thermophotovoltaic Energy Conversion With GaSb Lattice-Matched $\text{Ga}_x\text{In}_{1-x}\text{As}_y\text{Sb}_{1-y}$ Diodes,” *IEEE Transactions on Electron Devices*, vol. 66, no. 2, pp. 901–907, Jan. 2019. DOI: [10.1109/TED.2018.2888827](https://doi.org/10.1109/TED.2018.2888827).
- [123] B. Wen’gang, L. Azihen, and T. Songsheng, “Optical Properties of MBE-grown GaInAsSb,” *MRS Online Proceedings Library*, vol. 216, pp. 213–218, Dec. 1990. DOI: <https://doi.org/10.1557/PROC-216-213>.

- [124] S. Anikeev, D. Donetsky, G. Belenky, *et al.*, “Measurement of the Auger recombination rate in p-type 0.54 eV GaInAsSb by time-resolved photoluminescence,” *Applied Physics Letters*, vol. 83, no. 16, pp. 3317–3319, Oct. 2003. DOI: <https://doi.org/10.1063/1.1621455>.
- [125] G. W. Charache, P. F. Baldasaro, L. R. Danielson, *et al.*, “InGaAsSb thermophotovoltaic diode: Physics evaluation,” *Journal of Applied Physics*, vol. 85, no. 4, pp. 2247–2252, Feb. 1999. DOI: 10.1063/1.369533.
- [126] H. K. Choi, C. A. Wang, G. W. Turner, *et al.*, “High-performance GaInAsSb thermophotovoltaic devices with an AlGaAsSb window,” *Applied Physics Letters*, vol. 71, no. 26, pp. 3758–3760, Dec. 1997. DOI: 10.1063/1.120497.
- [127] J. Cederberg, M. Hafich, R. Biefeld, and M. Palmisiano, “The preparation of InGa(As)Sb and Al(Ga)AsSb films and diodes on GaSb for thermophotovoltaic applications using metal-organic chemical vapor deposition,” *Journal of Crystal Growth*, vol. 248, pp. 289–295, 2003. DOI: [https://doi.org/10.1016/S0022-0248\(02\)01927-9](https://doi.org/10.1016/S0022-0248(02)01927-9).
- [128] Z. A. Shellenbarger, M. G. Mauk, J. A. Cox, *et al.*, “GaInAsSb and InAsSbP photodetectors for mid-infrared wavelengths,” in *Infrared Detectors and Focal Plane Arrays V*, E. L. Dereniak and R. E. Sampson, Eds., International Society for Optics and Photonics, vol. 3379, SPIE, Jul. 1998, pp. 354–360. DOI: <https://doi.org/10.1117/12.317602>.
- [129] M. N. Abedin, T. F. Refaat, R. P. Joshi, O. V. Sulima, M. G. Mauk, and U. N. Singh, “Characterization and analysis of InGaAsSb detectors,” in *Infrared Technology and Applications XXIX*, B. F. Andresen and G. F. Fulop, Eds., International Society for Optics and Photonics, vol. 5074, SPIE, Oct. 2003, pp. 332–342. DOI: <https://doi.org/10.1117/12.486345>.
- [130] D. Hurtado-Castañeda, J. Herrera-Pérez, J. Arias-Cerón, C. Reyes-Betanzo, P. Rodriguez-Fragoso, and J. Mendoza-Álvarez, “Indium gallium arsenide antimonide photodetector grown by liquid phase epitaxy: Electrical char-

-
- acterization and optical response,” *Materials Science in Semiconductor Processing*, vol. 31, pp. 52–55, Mar. 2015. DOI: <https://doi.org/10.1016/j.mssp.2014.11.023>.
- [131] I. Shafir, N. Snapi, D. Cohen-Elias, *et al.*, “High responsivity InGaAsSb p–n photodetector for extended SWIR detection,” *Applied Physics Letters*, vol. 118, no. 6, p. 063503, Feb. 2021. DOI: <https://doi.org/10.1063/5.0037192>.
- [132] B. L. Carter, E. Shaw, J. T. Olesberg, W. K. Chan, T. C. Hasenberg, and M. E. Flatté, “High detectivity InGaAsSb pin infrared photodetector for blood glucose sensing,” *Electronics Letters*, vol. 36, no. 15, pp. 1301–1303, Jul. 2000. DOI: [10.1049/e1:20000956](https://doi.org/10.1049/e1:20000956).
- [133] C. Lin, Y. Zheng, and A. Li, “Mid-infrared GaInAsSb photodetector grown by solid source molecular beam epitaxy,” *Journal of Crystal Growth*, vol. 227–228, pp. 605–608, Jul. 2001. DOI: [https://doi.org/10.1016/S0022-0248\(01\)00781-3](https://doi.org/10.1016/S0022-0248(01)00781-3).
- [134] M. H. M. Reddy, J. T. Olesberg, C. Cao, and J. P. Prineas, “MBE-grown high-efficiency GaInAsSb mid-infrared detectors operating under back illumination,” *Semiconductor Science and Technology*, vol. 21, pp. 267–272, Jan. 2006. DOI: [10.1088/0268-1242/21/3/009](https://doi.org/10.1088/0268-1242/21/3/009).
- [135] K. C. Nunna, S. L. Tan, C. J. Reyner, *et al.*, “Short-Wave Infrared GaInAsSb Photodiodes Grown on GaAs Substrate by Interfacial Misfit Array Technique,” *IEEE Photonics Technology Letters*, vol. 24, no. 3, pp. 218–220, Feb. 2012. DOI: [10.1109/LPT.2011.2177253](https://doi.org/10.1109/LPT.2011.2177253).
- [136] E. Tournie, J. L. Lazzari, H. Mani, F. Pitard, C. L. Alibert, and A. F. Joullie, “Growth by liquid phase epitaxy and characterization of GaInAsSb and InAsSbP alloys for mid-infrared applications (2–3 μm),” in *Physical Concepts of Materials for Novel Optoelectronic Device Applications I: Materials Growth*

- and Characterization*, M. Razeghi, Ed., International Society for Optics and Photonics, vol. 1361, SPIE, 1991, pp. 641–656. DOI: 10.1117/12.24427.
- [137] A. Srivastava, J. DeWinter, C. Caneau, M. Pollack, and J. Zyskind, “High performance GaInAsSb/GaSb p-n photodiodes for the 1.8-2.3 μm wavelength range,” *Applied Physics Letters*, vol. 48, no. 14, pp. 903–904, Apr. 1986. DOI: <https://doi.org/10.1063/1.96653>.
- [138] A. Wörl, R. Müller, V. Daumer, J. Niemasz, F. Rutz, and R. Rehm, “Investigation of InGaAsSb-based heterojunction photodiodes for extended SWIR imaging,” in *Electro-Optical and Infrared Systems: Technology and Applications XX*, D. L. Hickman, H. Bürsing, G. W. Kamerman, and O. Steinvall, Eds., International Society for Optics and Photonics, vol. 12737, SPIE, 2023. DOI: <https://doi.org/10.1117/12.2680004>.
- [139] N. Li, J. Sun, Q. Jia, *et al.*, “High performance nBn detectors based on InGaAsSb bulk materials for short wavelength infrared detection,” *AIP Advances*, vol. 9, no. 10, p. 105 106, Oct. 2019. DOI: 10.1063/1.5124093.
- [140] L. A. Hanks, K. Mamic, K. Klos, *et al.*, “Quasi-planar InGaAsSb p-B-n photodiodes for spectroscopic sensing,” *Optics Express*, vol. 31, no. 9, pp. 14 358–14 366, Apr. 2023. DOI: <https://doi.org/10.1364/OE.485631>.
- [141] N. Li, W. Chen, D. Zheng, *et al.*, “The investigations to eliminate the bias dependency of quantum efficiency of InGaAsSb nBn photodetectors for extended short wavelength infrared detection,” *Infrared Physics Technology*, vol. 111, p. 103 461, 2020. DOI: <https://doi.org/10.1016/j.infrared.2020.103461>.
- [142] J. O. Kim, T. D. Nguyen, Z. Ku, A. Urbas, S.-W. Kang, and S. J. Lee, “Short wavelength infrared photodetector and light emitting diode based on InGaAsSb,” in *Infrared Technology and Applications XLIII*, B. F. Andresen, G. F. Fulop, C. M. Hanson, J. L. Miller, and P. R. Norton, Eds., International

-
- Society for Optics and Photonics, vol. 10177, SPIE, 2017, p. 101772M. DOI: 10.1117/12.2264969.
- [143] Z. A. Shellenbarger, M. G. Mauk, J. A. Cox, *et al.*, “Recent progress in GaInAsSb and InAsSbP photodetectors for mid-infrared wavelengths,” in *Photodetectors: Materials and Devices III*, G. J. Brown, Ed., International Society for Optics and Photonics, vol. 3287, SPIE, Apr. 1998, pp. 138–145. DOI: <https://doi.org/10.1117/12.304474>.
- [144] M. Henini, Ed., *Molecular Beam Epitaxy: From Research to Mass Production*, first. Elsevier Science Technology, 2012.
- [145] R. F. C. Farrow, Ed., *Molecular Beam Epitaxy: Applications to Key Materials* (Electronic Materials and Process Technology). Elsevier Science Technology, 2014.
- [146] S. Izumi, N. Hayafuji, T. Sonoda, S. Takamiya, and S. Mitsui, “Less than 10 defects/cm² · μm in molecular beam epitaxy grown GaAs by arsenic cracking,” *Journal of Crystal Growth*, vol. 150, pp. 7–12, 1995. DOI: [https://doi.org/10.1016/0022-0248\(95\)80171-8](https://doi.org/10.1016/0022-0248(95)80171-8).
- [147] P. D. Brewer, D. H. Chow, and R. H. Miles, “Atomic antimony for molecular beam epitaxy of high quality III–V semiconductor alloys,” *Journal of Vacuum Science Technology B: Microelectronics and Nanometer Structures Processing, Measurement, and Phenomena*, vol. 14, no. 3, pp. 2335–2338, May 1996. DOI: <https://doi.org/10.1116/1.588854>.
- [148] J. Matthews and A. Blakeslee, “Defects in epitaxial multilayers: I. Misfit dislocations,” *Journal of Crystal Growth*, vol. 27, pp. 118–125, Dec. 1974. DOI: [https://doi.org/10.1016/S0022-0248\(74\)80055-2](https://doi.org/10.1016/S0022-0248(74)80055-2).
- [149] Bruker, *D8 ADVANCED DISCOVER User Manual Vol. 1*, https://nanoqam.ca/wiki/lib/exe/fetch.php?media=d8_advance_discover_user_manual_vol._1_doc-m88-exx153_v6.pdf.

- [150] MicroChem, *LOR Lift-Off Resists*, https://amolf.nl/wp-content/uploads/2016/09/datasheets_LOR_datasheet.pdf.
- [151] Shipley, *Microposit S1800 series photo resist*, https://amolf.nl/wp-content/uploads/2016/09/datasheets_S1800.pdf.
- [152] S. MicroTec, *SUSS MJB4*, https://res.cloudinary.com/demhlsnej/image/upload/v1605285633/mask_aligner_mjb4_b8f389c105.pdf.
- [153] Shipley, *Microposit MF CD-26 Developer*, https://kayakuam.com/wp-content/uploads/2019/10/MF_CD_26_Data_Sheet.pdf.
- [154] A. Greene, S. Madisetti, P. Nagaiyah, *et al.*, “(invited) ingasb mosfet channel on metamorphic buffer: Materials, interfaces and process options,” *ECS Transactions*, vol. 53, no. 1, pp. 149–160, May 2013. DOI: 10.1149/05301.0149ecst.
- [155] DuPont, *DuPont Kapton Summary of Properties*, https://www.dupont.com/content/dam/dupont/amer/us/en/ei-transformation/public/documents/en/EI-10142_Kapton-Summary-of-Properties.pdf.
- [156] X. Zhang, A. Z. Li, C. Lin, *et al.*, “The effects of $(\text{NH}_4)_2\text{S}$ passivation treatments on the dark current–voltage characteristics of InGaAsSb PIN detectors,” *Journal of Crystal Growth*, vol. 251, pp. 782–786, 2003. DOI: [https://doi.org/10.1016/S0022-0248\(02\)02369-2](https://doi.org/10.1016/S0022-0248(02)02369-2).
- [157] Y. G. Xiao, V. Bhagwat, I. Bhat, and P. Dutta, “Dark current reduction of GaInAsSb based photodetectors by surface treatment with octadecylthiol,” in *Infrared Systems and Photoelectronic Technology II*, E. L. Dereniak, J. P. Hartke, R. E. Longshore, and A. K. Sood, Eds., International Society for Optics and Photonics, vol. 6660, SPIE, 2007, p. 66600V. DOI: <https://doi.org/10.1117/12.732706>.
- [158] B. Wu, G. Xia, Z. Li, and J. Zhou, “Sulphur passivation of the InGaAsSb/GaSb photodiodes,” *Applied Physics Letters*, vol. 80, no. 7, pp. 1303–1305, Feb. 2002. DOI: 10.1063/1.1448383.

-
- [159] Z. Li, G. Xia, B. Wu, W. Huang, and Z. Cheng, “Sulfur-passivation mechanism analysis of GaInAsSb photodetectors,” *Journal of Applied Physics*, vol. 94, no. 3, pp. 1295–1297, 2003.
- [160] E. Papis, A. Piotrowska, E. Kamińska, *et al.*, “Sulphur passivation of GaSb, InGaAsSb and AlGaAsSb surfaces,” *Physica Status Solidi C*, vol. 4, no. 4, pp. 1448–1453, 2007. DOI: <https://doi.org/10.1002/pssc.200674147>.
- [161] M. V. Lebedev, V. V. Sherstnev, E. V. Kunitsyna, I. A. Andreev, and Y. P. Yakovlev, “Passivation of Infrared Photodiodes with Alcoholic Sulfide Solution,” *Semiconductors*, vol. 45, no. 4, pp. 526–529, 2011. DOI: <https://doi.org/10.1134/S1063782611040142>.
- [162] J. V. Li, S. L. Chuang, O. V. Sulima, and J. A. Cox, “Passivation of AlGaAsSb/InGaAsSb/GaSb photodiodes using aqueous $(\text{NH}_4)_2\text{S}$ solution and polyimide encapsulation,” *Journal of Applied Physics*, vol. 97, May 2005. DOI: <https://doi.org/10.1063/1.1898447>.
- [163] K. A. Materials, *SU-8 2000 Permanent Negative Epoxy Photoresist*, <https://kayakuam.com/wp-content/uploads/2020/08/KAM-SU-8-2000-2000.5-2015-Datasheet-8.13.20-final.pdf>.
- [164] Bruker, *VERTEX 70v FT-IR Spectrometer*, https://www.bruker.com/en/products-and-solutions/infrared-and-raman/ft-ir-research-spectrometers/vertex-research-ft-ir-spectrometer/vertex-70v-ft-ir-spectrometer.html?page_1=2.
- [165] Bruker, *VERTEX 70v User Manual*, https://www.gfmoorelab.com/uploads/4/2/3/1/42315775/vertex_70_i26021_en_6th_rev._edition-2.pdf.
- [166] Bentham, *PVE300 Photovoltaic EQE (IPCE) and IQE solution*, <https://www.bentham.co.uk/products/systems/pve300-photovoltaic-eqe-ipce-and-iqe-solution-16/>.

- [167] Bentham, *TMc300 Single Monochromator*, <https://www.bentham.co.uk/products/components/tmc300-single-monochromator-38/>.
- [168] A. P. Craig, “Lattice Mismatched Infrared Photodetectors,” Ph.D. dissertation, Lancaster University, 2015.
- [169] W. T. Ltd, *Gallium Antimonide: Epitaxy Ready Polished Wafers*, <http://www.wafertech.co.uk/pdfs/gasb.pdf>.
- [170] Veeco, *Growth Control Scheduling Software for MBE Systems*, <https://www.veeco.com/products/growth-control-scheduling-software-for-mbe-systems/>.
- [171] W. T. Ltd, *Gallium Arsenide: Epitaxy Ready Polished Wafers*, <http://www.wafertech.co.uk/pdfs/gaas.pdf>.
- [172] R. Ferrini, M. Patrini, and S. Franchi, “Optical functions from 0.02 to 6 eV of $\text{Al}_x\text{Ga}_{1-x}\text{Sb}/\text{GaSb}$ epitaxial layers,” *Journal of Applied Physics*, vol. 84, no. 8, pp. 4517–4524, Oct. 1998. DOI: <https://doi.org/10.1063/1.368677>.
- [173] T. Skauli, P. S. Kuo, K. L. Vodopyanov, *et al.*, “Improved dispersion relations for GaAs and applications to nonlinear optics,” *Journal of Applied Physics*, vol. 94, no. 10, pp. 6447–6455, Nov. 2003. DOI: <https://doi.org/10.1063/1.368677>.
- [174] M. Wasiak, M. Motyka, T. Smolka, J. Ratajczak, and A. Jasik, “Absorption and dispersion in undoped epitaxial GaSb layer,” *Materials Research Express*, vol. 5, 2018. DOI: [10.1088/2053-1591/aaae86](https://doi.org/10.1088/2053-1591/aaae86).
- [175] C. Ghezzi, R. Magnanini, A. Parisini, *et al.*, “Optical absorption near the fundamental absorption edge in Gasb,” *Physical Review B*, vol. 52, no. 3, pp. 1463–1466, Jul. 1995. DOI: <https://doi.org/10.1103/PhysRevB.52.1463>.
- [176] G. W. Gobeli and H. Y. Fan, “Infrared Absorption and Valence Band in Indium Antimonide,” *Physical Review*, vol. 119, no. 2, pp. 613–620, Jul. 1960. DOI: <https://doi.org/10.1103/PhysRev.119.613>.

-
- [177] J. R. Dixon and J. M. Ellis, “Optical Properties of n-Type Indium Arsenide in the Fundamental Absorption Edge Region,” *Physical Review*, vol. 123, no. 5, pp. 1560–1566, Sep. 1961. DOI: <https://doi.org/10.1103/PhysRev.123.1560>.
- [178] D. A. Humphreys, R. J. King, D. Jenkins, and A. J. Moseley, “Measurement of Absorption Coefficients of $\text{Ga}_{0.47}\text{In}_{0.53}\text{As}$ Over the Wavelength Range 1.0–1.7 μm ,” *Electronics Letters*, vol. 21, no. 25/26, pp. 1187–1189, Dec. 1985. DOI: [10.1049/e1:19850839](https://doi.org/10.1049/e1:19850839).
- [179] S. D. Pandey, S. K. Dubey, R. L. Dubey, *et al.*, “Investigations on the effect of argon ion bombardment on the structural and optical properties of crystalline gallium antimonide,” *Radiation Effects & Defects in Solids*, vol. 161, no. 7, pp. 433–442, Jul. 2006. DOI: <https://doi.org/10.1080/10420150600764405>.
- [180] M. Muñoz, K. Wei, F. H. Pollack, J. L. Freeouf, and G. W. Charache, “Spectral ellipsometry of GaSb: Experiment and modeling,” *Physical Review B*, vol. 60, no. 11, pp. 8105–8110, Sep. 1999. DOI: <https://doi.org/10.1103/PhysRevB.60.8105>.
- [181] N. M. Ravindra and B. Prasad, “Saturation current in solar cells: an analysis,” *Solar Cells*, vol. 2, no. 2, pp. 109–113, Oct. 1980. DOI: [https://doi.org/10.1016/0379-6787\(80\)90004-6](https://doi.org/10.1016/0379-6787(80)90004-6).
- [182] M. Mintairov, V. Evstropov, S. Mintairov, M. Shvarts, and N. Kalyuzhnyy, “Relation between energy gap and saturation currents in GaInAs homo p-n junctions,” *Journal of Physics: Conference Series*, vol. 1410, no. 1, p. 012097, Dec. 2019. DOI: [10.1088/1742-6596/1410/1/012097](https://doi.org/10.1088/1742-6596/1410/1/012097).
- [183] Hamamatsu, *InGaAs PIN photodiode G12183-003K*, <https://www.hamamatsu.com/jp/en/product/optical-sensors/infrared-detector/ingaas-photodiode/G12183-003K.html>.

References

- [184] L. A. Hanks, “Experimental and Theoretical Determination of the Transport Properties of n-Al_xGa_{1-x}Sb/GaSb,” Ph.D. dissertation, Lancaster University, 2019.
- [185] T. J. Technologies, *J22 and J23 SERIES InGaAs PHOTODIODES Operating Instructions*, <http://www.teledynejudson.com/prods/Documents/PB4206.pdf>.